Generation of Treatment Plans for Magnetic Resonance guided High Intensity Focused Ultrasound (MRgHIFU) in the Liver

Inaugural dissertation

to
be awarded the degree of Dr. sc. med.

presented at
the Faculty of Medicine
of the University of Basel

by
Nadia Möri
from Bern, Switzerland

Basel, 2018

Originaldokument gespeichert auf dem Dokumentenserver der Universität Basel **edoc.unibas.ch**

Dieses Werk ist lizenziert unter einer Creative Commons Namensnennung-Nicht kommerziell 4.0 International Lizenz.

Approved by the Faculty of Medicine
on application of

Prof. Dr. Philippe C. Cattin, University of Basel, *First examiner*
Prof. Dr. Oliver Bieri, *Second examiner*
Dr. Christoph Jud, *Third examiner*
Prof. Dr. Niels Kuster, *External expert*

Basel, 12th April 2018

Prof. Dr. med. Thomas Gasser
Dean

To all those
who left their life
for this work.
Especially the turkeys.

Contents

Acknowledgments

First of all, I want to thank Prof. Dr. Philippe C. Cattin for giving me the opportunity to work on such an interesting PhD project. It is a pleasure how Philippe supports his students by leaving them enough freedom to explore their ideas, but at the same time giving all the needed advise.

I am grateful for the support of the team of Dr. Rares Salomir from the Radiology Department at the University of Geneva. Without their help and support this work would not be what it is. I especially want to thank Dr. Rares Salomir for reviewing all of my papers and giving new insights into the field of focused ultrasound. Thanks also to Dr. Laura Gui, for her great work resulting in very interesting experiments. Last but not least, I also want to thank Orane Lorton and Pauline Guillemin.

I am thankful to all current and former team members of the *Center for medical Image Analysis and Naviation* (CIAN), of the University of Basel, Switzerland: Simon Andermatt, Dr. Natalia Chicherova, Corinne Eymann-Baier, Dr. Beat Fasel, Alina Giger, Antal Horváth, Lorenzo Iafolla, Dr. Christoph Jud, Samaneh Manavi, Dr. Uri Nahum, Peter von Niederhäusern, Dr. Simon Pezold, Tiziano Ronchetti, Robin Sandkühler, Dr. Adrian Schneider, Carlo Seppi, Jörg Wagner, Dr. Lilian Witthauer, Dr. Stephan Wyder, and Marek Zelechowski. Among these, I especially want to thank Dr. Christoph Jud for the interesting discussions beyond the main scope of my research and all the help he provided me throughout my study time.

Finally, I want to give thanks to my family and friends for their support during my study time.

Summary

Primary liver tumor incidence is about 780 new cases per year in Switzerland with a poor prognosis, where the 5-year survival rate is only 10%. High intensity focused ultrasound (HIFU) is a non-invasive thermal ablation modality for tumor treatment which has been widely accepted for about a decade. For image guidance during HIFU sonication, ultrasound as well as magnetic resonance (MR) imaging can be used. MR not only provides images of the tumor and its motion, but is also used for temperature mapping from which the thermal dose is calculated to determine the tissue damage. MR-guided HIFU has been successfully applied for tumor ablation in immobile organs, such as uterus, prostate, breast and brain. However, HIFU treatment of abdominal organs, such as kidney and liver, remains challenging due to respiratory organ motion.

Today, there are two established principles to address the problems of liver motion in HIFU sonication: the gating and tracking strategy. In this thesis, the self-scanning method is proposed to handle organ motion. It takes advantage of the perpetual respiratory motion to passively scan the tumor. In other words, we are placing the static focal point of the HIFU into the tumor. The motion caused by breathing shifts the tumor through this focal point. We anticipate at which time point tumor tissue is located under the focal spot and modulate the HIFU intensity based on this information. Once the tumor has been ablated along the self-scanned trajectory, the focal spot is relocated to a different but static position within the body. With this method, we combine the advantages of the gating and the tracking method: a HIFU device with a fixed focus can be used and a high duty cycle is achieved. Moreover, since with the self-scanning approach no lateral steering of the focal spot is required, fewer secondary lobes are generated and position-dependent decay of the focal spot intensity during lateral steering is avoided. However, this comes at the cost of an increased complexity at the planning stage.

Three evolutionary steps towards a treatment planning method that can handle non-periodic respiratory motion are presented. In a first step, a simplified linear model is assumed to show the feasibility of the self-scanning method. This model is expanded to a more realistic non-linear model, while repetitive respiratory motion is assumed. In the third step, the method is modified such that it can handle non-periodic respiratory motion. In addition, the method provides shorter computational times compared to the previous approach. Moreover, the temperature model is adapted such that tissue inhomogeneities are included. The method and temperature model are confirmed in ex-vivo experiments, showing that a uniform temperature rise can be induced in the presence of motion and tissue inhomogeneities. These results are a first proof of principle of the self-scanning approach, confirming that the temperature rise inside the tumor can be controlled and thus tumor ablation with the self-scanning method inside the liver is in principle possible in not too slow treatment times.

1 Introduction

1.1 Motivation

Primary liver tumor incidence is about 780 new cases per year in Switzerland with a poor prognosis, where the 5-year survival rate is only 10% [2]. A non-invasive modality to treat tumors within the liver is high-intensity focused ultrasound (HIFU) [15, 17, 34, 36]. HIFU treatments can be guided by magnetic resonance (MR) imaging, which is used to track the tumor position and measure the induced temperature rise [27]. HIFU has been successfully used in the treatment of immobile tumors, such as uterus, prostate, breast and brain [34, 63]. However, HIFU treatment in abdominal organs, such as liver and kidney, remains challenging due to the respiratory motion [43]. Up to date, there are two methods to deal with the organ motion: gating and tracking [34]. The gating method leverages an almost stationary part of the breathing cycle, during which the tumor is treated. The disadvantage of the gating method is the long treatment time. The idea of the tracking method on the other hand is to continuously move the focal point position according to the respiratory motion. This approach results in shorter treatment times, however, lateral steering of the focal spot leads to an intensity decay.

In this thesis, a new method called self-scanning is proposed, which takes advantage of the perpetual respiratory motion. The focal point of the HIFU device is placed inside the tumor. The motion caused by breathing moves the tissue through this focal point. Using a motion model, the position of the tumor is anticipated and the HIFU intensity is modulated based on this information. Once the tumor has been ablated along the self-scanned trajectory, the focal spot is relocated to a different but static position within the body. With the proposed self-scanning method, we combine the advantages of the gating and the tracking method: a static HIFU device can be used and a high duty cycle is achieved. Moreover, the complexity of the beam forming problem is reduced. However, this comes at the cost of an increased complexity during the planning stage.

The aim of this thesis is to provide a method that is able to calculate feasible treatment plans for the self-scanning approach. The treatment plan must ablate the whole tumor, while minimizing treatment time and healthy tissue treatment. Moreover, the method should be able to handle non-periodic respiratory motion during treatment.

1.2 Contribution

To verify the concept of the self-scanning approach, we first propose a treatment planning method based on a simplified model, assuming linear dose delivery. In particular,

it is assumed that no heat diffusion over time occurs. Shorter treatment times compared to the tracking approach are found, indicating the feasibility of the method. As a second step, the linear model is extended to include diffusion over time and the non-linear thermal dose model. This method's results show that it is possible to find a feasible treatment plan under the assumption of a repetitive respiratory motion pattern. In a third step, the planning method is finally extended to non-periodic respiratory motion. In addition, the number of optimization parameters is reduced, leading to shorter computational times. An adaptive temperature model that is able to incorporate tissue inhomogeneities is proposed. The method is verified in ex-vivo experiments on moving turkey muscle, showing that a uniform temperature rise can be induced in the presence of motion and tissue inhomogeneities. Overall, this method is a step towards real-time treatment planning.

1.3 Outline

In Chapter 2, the medical background of this thesis and the physical, physiological and technical principles of HIFU are explained. Chapter 3 gives an overview of the mathematical models describing HIFU, namely how the temperature and the thermal dose are calculated. Chapter 4 summarizes the mathematical optimization tools utilized in the proposed treatment planning algorithms. Chapters 5–7 comprise the publications that resulted from our work to date. Chapter 5 shows a feasibility study for the self-scanning approach which is based on a simplified model. Chapter 6 expands the treatment planning method to a more realistic model including the non-linear thermal dose, while still assuming periodic motion patterns. The method shown in Chapter 7 is applicable to non-periodic respiratory motion patterns and proposes a temperature model that can adapt to tissue inhomogeneities. We show in ex-vivo experiments that the method is able to induce a near uniform temperature rise in presence of motion and tissue inhomogeneities. The thesis is completed with a discussion and conclusion in Chapter 8.

2 Background

2.1 Medical Background

Liver. The liver is located at the upper right portion of the abdomen, just beneath the diaphragm. It is a large dark-red gland which weighs about 1.5 kg in an adult [32]. The liver is important in the metabolism of the body. Among its functions is the secretion of bile, storage and filtration of blood, conversion of sugar into glycogen, the detoxification of drugs and alcohol, and many other activities [32].

Organ Motion. Breathing is caused by the motion of the diaphragm and the intercostal muscles, inducing a volume change in the lungs. During inhalation, the abdominal organs move downwards in craniocaudal direction and they move in superior direction again during exhalation [54]. The motion in the liver is mainly along the craniocaudal direction, with a motion amplitude of about 5–25 mm during relaxed breathing [54]. The motion along the latero-lateral direction is less with about 1–3 mm, while the component in the antero-posterior axis is 1–12 mm [60]. The three different components of the liver motion can be viewed in Fig. 2.1, where the mean motion over the whole liver is shown. The liver exhibits nonrigid deformations of up to 20 mm caused by sliding along the abdominal wall, resulting in variable organ and tumor shapes [54].

The motion pattern, i.e. the amplitude and the period, is different from subject to subject, but also varies over time and might even change within a few minutes [54, 43]. The period of the respiratory motion is in the range of 3–5 s, where shallow and deep breathing has an influence and might result in shorter or longer period times [22]. Other reasons for the intrasubject motion variation are different muscle tension, emotional changes, sighing and coughing [54]. Besides respiratory induced motion, the heart beat has an influence on the motion on the left side of the liver [60, 43].

Liver Tumors. Tumors that occur in the liver are called hepatic tumors, where hepatic comes from the Greek word for liver, hepar. The growth of the tumor can be either benign (non-invasive tumor) or malignant (cancerous, tending to metastases) [32]. Most cases of malignant cancer within the liver are metastases from other tumors, where the primary tumor is mostly lying in the breast, lung and the colon [5]. The most frequent malignant primary liver cancer is hepatocellular carcinoma (HCC), which is the third leading cause of cancer mortality worldwide [2]. In Switzerland, approximately 2% of all cancer incidences are caused by HCC, which corresponds to

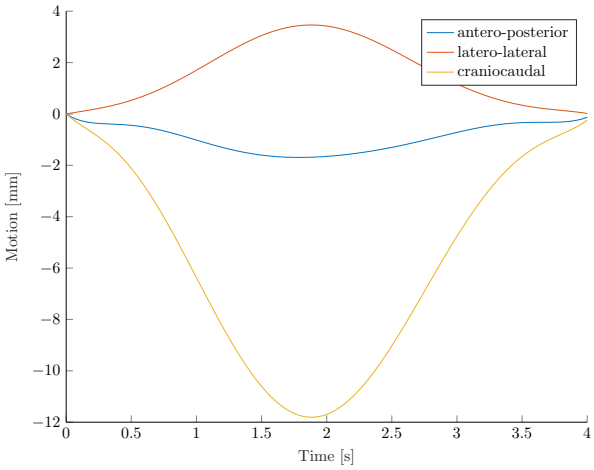

Figure 2.1: Liver motion in craniocaudally, latero-lateral, and antero-posterior direction. The mean motion of the whole liver is shown during a representative breathing cycle of one specific patient, were the data is from [33].

about 780 new cases every year[1]. Although relatively rare in Switzerland, the prognosis is poor, as HCC is often diagnosed in an advanced disease stage. The 5-year survival rate is low with approximately 10% [2].

The most important risk factor for HCC is cirrhosis, a long-term effect of many chronic liver diseases [7]. Mostly, cirrhosis is a consequence of viral Hepatitis and alcohol abuse [32]. In Europe, 40–50% of all HCC cases are caused by alcohol abuse [7].

If HCC is detected in a patient, the tumor stage, liver function and physical status of the patient should be considered to decide which treatment modality is chosen. If the tumor is already in a progressed stage, there is no effective treatment that improves survival, and thus the treatment is mainly palliative [7]. Depending on the tumor size, location and liver function, resection of the tumor can be done. Another treatment used in early stages is liver transplantation. However, the problem is the shortage of available organs and a long waiting time. Examples for nonsurgical approaches are transarterial chemoembolization (TACE), radiofrequency ablation (RFA), microwave ablation (MWA) and high intensity focused ultrasound (HIFU). There is also a systemic therapy with the drug sorafenib [10]. A staging system for HCC can be found in [10].

RFA and MWA are minimally invasive methods, where a needle is inserted into the tumor [12, 23]. In RFA, the needle emits high frequency electric current, while the MWA needle emits electromagnetic waves. In both cases the temperature inside the tissue is increased, leading to tumor ablation. A risk of methods that rely on needle

[1] www.krebsliga.ch/ueber-krebs/krebsarten/leberkrebs-hepatozellulaeres-karzinom (last accessed on December 21, 2017)

insertion, like RFA and MWA, is tumor seeding along the needle path [34]. In TACE, embolic particles and chemotherapeutic drugs are injected through a catheter into the hepatic artery feeding the tumor [59]. The goal is to cause a local loss of blood supply (ischemia). HIFU is a non-invasive treatment modality that is based on heating the tissue by mechanical waves. The advantages of HIFU as compared to other treatment modalities is the lower morbidity and fewer complications [5]. However, the treatment of liver tumors is difficult due to respiratory motion. The treatment of abdominal tumors with HIFU will be explained in more detail in Section 2.2.4.

2.2 High Intensity Focused Ultrasound (HIFU)

2.2.1 Physical and Technical Principles

Ultrasound is a sound wave with frequencies above human hearing, i.e. frequencies greater than 20 kHz [34, 17]. Sound waves are mechanical waves that propagate through vibrations of particles. They are classified into transversal (also called shear waves) and longitudinal waves, depending on the particle movement, which is either transverse or parallel to the direction of propagation [65]. Longitudinal waves occur in every medium, whereas transversal waves are only present in solids. Concerning ultrasound, soft tissue is modeled as liquid and hence shear waves are neglected [18]. The reason for this assumption is that shear waves are not efficiently generated by ultrasound devices. Moreover, if a shear wave propagates through tissue, it is strongly absorbed and will not travel far. Note however, that the bone is solid and thus shear waves occur.

Physical Parameters of Ultrasound Waves. The physical parameters that describe an ultrasound wave are the frequency, pressure, wavelength, velocity, power and intensity [65]. The frequency is the number of complete oscillations that each particle undergoes per second. For diagnostic ultrasound, which is used for imaging (e.g. fetal development), frequencies in the range of 1–20 MHz are used [18]. In focused ultrasound, where the waves are focused to a point, frequencies in the range of 0.8–3.5 MHz are used [34].

The wavelength and the frequency are inversely related. In ultrasound imaging, decreasing the wavelength (and hence increasing the frequency) results in a higher spatial resolution, as two separate structures can be more accurately distinguished. However, high-frequency waves are more attenuated than lower frequency waves, which means that they can not penetrate deep into the body [13].

The velocity of a wave is defined as the speed of propagation inside the tissue. Ultrasound travels in tissue at about 1540 m/s, depending on the tissue type [65].

The power and the intensity are measures of the strength of a wave. Power is the total energy that passes through a surface per unit time. Intensity is the energy per unit area per unit time [65]. In high intensity focused ultrasound the intensity is the highest at the focal spot, where the beam width is the narrowest, with values greater than 5 W/cm^2 [17].

Attenuation and Absorption. It takes energy for a wave to travel through tissue, and as a result the amplitude decreases continuously. This process is called attenuation. The causes of attenuation are divergence, scattering and absorption [65]. Divergence of the beam causes an intensity decay due to a larger beam area. Scattering refers to the reflection of sound from surfaces of heterogeneities in a medium. The greatest cause of attenuation, however, is absorption. The acoustic energy is absorbed by tissue and converted into heat. The amount of absorption increases linearly with the wave frequency. Bone has a higher absorption coefficient compared to soft tissue, which leads to a shielding effect of bones [27].

Reflection and Acoustic Impedance. At the boundary of two different materials, some part of the ultrasound waves is reflected while the other part transmits through the boundary. Acoustic impedance is a measure of the resistance that a material offers to the passage of ultrasound waves [65]. The greater the difference in the impedance values at the boundary of two materials, the more energy will be reflected. Because the difference in the impedance of air and tissue is that large, almost all ultrasound waves are reflected at their boundary. Hence for transmitting ultrasound waves into the body, the transducer emitting ultrasound waves should be coupled to the skin by an acoustic coupling agent (for example gel), which ensures that the waves are transmitted into the tissue [65].

Transducers. Ultrasound is generated by transducers, which are made of piezoelectric materials [17]. If a harmonically varying electric field is applied, the piezoelectric material is vibrating and thus creating a sound wave. Ultrasound transducers are constructed from multiple piezoelectric pieces that can be lined up in different structures, resulting in various transducer types [14].

Annular Transducers. Annular transducers consist of concentric ring shaped piezoelectric crystals. The beam focus can be steered to different depths along the beam axis by independent control of each of the crystals.

Phased-Array Transducers. The piezoelectric pieces in phased-array transducers are lined up in an array and each element is controlled independently. By adjusting the controlling times and delays of each crystal, the beam can be steered in all directions, not only along the beam axis [31].

2.2.2 Physiological Mechanisms

The damage caused by HIFU in tissue is mainly due to heating and cavitation [36, 34, 17]. There are three types of lesions [24]:

1. Thermally induced lesions with low intensities and long exposure times.
2. Cavitation induced lesions with high intensities and short exposure times.
3. Intermediate exposures (both intensities and exposure times). It seems that in these lesions cavitation plays an important role, although they have characteristics of thermal damage.

After the treatment by focused ultrasound, necrotic tissue remains and a gradual shrinkage of the treated volume occurs over time, indicating the replacement of the necrotic region with fibrous scar tissue [34]. The lesion is well circumscribed with an intermediate zone between intact and destroyed cells of several cell layers thickness [17].

Thermal Effect. The thermal effect arises due to the conversion of mechanical energy into heat. The tissue damage depends on the temperature rise and the exposure time. A temperature of 56°C during 1 s induces cell death [17, 34, 36, 63]. The steep temperature gradient that is possible with focused ultrasound causes a sharp boundary between treated and untreated tissue in histological examination [63].

The temperature rise inside the body induces protein denaturation, which means that the proteins lose their structure, causing them to lose some or all of their characteristics [55]. This results in disruption of the cell activity and may then lead to coagulative necrosis, which is a type of accidental cell death [53].

The lesion size depends on the used frequency, tissue acoustic properties, ultrasound intensity, exposure time and transducer geometry [56]. There is a huge variation in the needed acoustic powers due to variances in the tissue acoustic properties [27].

Cavitation. During the rarefaction (i.e. low pressure) phase of the ultrasound wave, gas can be drawn from the tissue and forms bubbles, this phenomenon is called cavitation [34]. These gas bubbles oscillate due to the pressure changes induced by ultrasound. There are two types of cavitation: non-inertial (stable) and inertial (collapse) [24]. In the non-inertial case, the bubbles' size increases during rarefaction and decreases during compression. These bubbles then scatter ultrasound, which leads to prefocal and increased heating [6]. In the inertial case, the bubble will collapse and induce a local release of energy. As a result, the temperature increases and the energy release causes fragmentation of the cells [6, 34].

While thermal effects caused by ultrasound are linear with the applied power and intensities, and are therefore rather easy to predict, cavitation is less predictable and may have more complications. However, it can increase the ablated tissue volume and has an influence on lesion forming [17, 6]. It is used to optimize focused ultrasound treatments by reducing the treatment time [63, 36]. Another modality to use cavitation for tumor ablation is histotripsy [30].

In thermal treatments, where the intention is to create a thermally induced lesion, the temperature rise should be below the boiling limit of tissue. If the temperature inside the tissue is lower than 100°C, boiling and the resulting gas formation can be avoided [26].

2.2.3 Focused Ultrasound Surgery

Ultrasound waves can be bundled similar to light, which is called focused ultrasound. The advantage of focused ultrasound is that while the tissue at the focal spot receives a high pressure field and thus a temperature rise is induced at these points,

the surrounding tissue is unaffected [34]. If the intensity of the focused ultrasound is high, i.e. in the order of 100–10 000 $\mathrm{W/cm^2}$ [17], it is called high intensity focused ultrasound, short HIFU. Due to the described focusing property, HIFU is the only non-invasive modality to treat tumors within the body [63].

HIFU tumor treatment. A HIFU treatment consists of a planning stage, the treatment itself and post-therapy imaging [52]. During the planning stage, the tumor is localized within the body and the sonication points and intensities are determined. Furthermore, problems like for example organs at risk are identified, and the beam steering through or beside strongly absorbing bones and organ motion have to be integrated into the planning [6]. During the treatment, the temperature increase is monitored, either by ultrasound or magnetic resonance (MR) imaging [17]. From the temperature, the thermal dose is calculated [51] and the treatment is terminated if a lethal dosage is achieved inside the tumor.

Frequency Choice. The frequency choice in focused ultrasound has several implications. As mentioned in Section 2.2.1, the amount of absorption increases linearly with the wave frequency. This leads to a trade-off between keeping attenuation in near field tissue low, while maximizing the energy at the focal spot [56]. When using high frequencies, the energy is more sharply focused as compared to lower frequencies [17].

Advantages. The main advantage of HIFU lies in its non-invasive nature. In contrast to other tumor treatment modalities it is not tissue specific, as every tissue type responds to heat [34]. Due to this fact, it is unlikely that a specific tumor resistance is generated [34]. Moreover, in contrast to ionizing treatments, there is no upper tolerance for repeated treatments [34]. This means that if after the treatment the tumor is not yet fully ablated, it can be repeated at a later time. Moreover, HIFU treatment has very few side effects and serious events are rare [34, 17]. As it may relieve from pain, it is also useful for palliative care [63, 17].

Limitations. As sound waves do not pass through air because of the large difference in the acoustic impedance between air and tissue, no treatment of tumors within the lung or within hollow organs is possible [34, 36]. As the attenuation in solids such as bone is large, the treatment of structures behind bones, for example organs below the ribs or brain tumors, is difficult [27]. Despite these difficulties, brain tumors have been treated through the intact skull and special focusing approaches were developed to steer through the rib cage [17]. If organs at risk, for example the heart, gall bladder or bowel, are close to the tumor, the HIFU treatment might be hindered [34].

Another limitation of HIFU is the long treatment time [34]. As the focal spot has a size of approximately $1 \times 1 \times 5\,\mathrm{mm^3}$, a tumor of larger size needs to be treated by multiple sonication points, which is time consuming [17, 34]. A method to overcome this problem is rapid heating and volumetric ablation [17].

Clinical Use and Side Effects. A detailed review of the clinical cases can be found in [34, 36, 17]. Up to now, HIFU has already been clinically used in malignant and benign tumors in the liver, kidney, renal, brain, pancreas, breast tumors and in uterine fibroids. The clinical results suggest that successful ablation of tumors is possible with only few complications. HIFU is considered as a potential alternative for surgical resection, which means that additional treatment such as chemotherapy or radiotherapy might still be used.

Most of the reported side effects of HIFU are skin burns, which result as the absorption in the skin is several times higher compared to internal soft tissue [6, 34, 17]. Reasons for skin burns are improper coupling of the transducer to the skin, scars in the pathway of the beam, improperly shaved or cleaned skin, which all lead to higher absorption values [17]. A solution for this problem might be the cooling of the skin and the transducer [6]. Another side effect of focused ultrasound is local pain [36, 34]. The pain was reported to be mild, short-lived and transient and could be prevented by moderated sedation [17]. Moreover, transient fever was reported [36, 34].

Rib fracture is a specific side effect of liver tumor treatment, although the incidence is rare [17]. More frequent side effects are skin burns and and rib heating. It was found that the temperature inside the ribs is about five times higher compared to the intercostal space [5]. Steering the focal spot through the rib cage is discussed in more detail in Section 2.2.4. Another problem in liver tumor when treated with the tracking approach are secondary hot spots [4].

Image Guidance during Surgery. For tumor, motion and temperature monitoring, ultrasound and MR imaging are used. Another application of image guidance is that the local tissue properties can be visualized [49]. This is important as the tissue properties are patient-specific and can thus not be known prior to the treatment, but play an important role in the temperature increase [49].

Ultrasound Guidance. Ultrasound can monitor cavitation bubbles, attenuation, temperature and the displacement of tissue [6]. HIFU induces physical changes of the tissue, which can be visualized by ultrasound imaging and thus the current status of the treatment is visualized [6]. If for example proteins denature, the local stiffness is irreversibly increased and can be measured using elastography [8]. Ultrasound is inexpensive and available, mobile, easy to apply and the same modality as HIFU. Moreover, it has a high temporal resolution [36, 17]. However, the image resolution is poor and the field of view is limited [36]. The real-time thermometry used for focal spot detection and correction as well as treatment monitoring is not as sophisticated compared to MR, but this is an area of active research [17]. As the requirements for focused ultrasound and imaging ultrasound are different, compromises have to be made to use the same device.

Artifacts in the presence of motion are no problem using ultrasound imaging due to the high temporal resolution of about 20–50 frames per second [5]. Temperature mapping, on the other hand is affected if it is based on the heat-related change of speed of sound [5].

MR Guidance. MR imaging is used for monitoring the tumor and the temperature.

The advantages of MR are its excellent soft tissue contrast and real-time thermometry [36, 17]. Real-time thermometry allows to adjust the position of the focal spot, online calculation of the thermal dose and adjustment of the treatment to unpredictable local tissue characteristics [17, 27]. However, MR is expensive to use, has large devices and lower spatial and temporal resolution compared to ultrasound. Moreover, an MR-compatible HIFU device is needed [17].

The most frequently used MR-thermometry measurement technique is proton resonance frequency (PRF) shift, which uses the linear dependence of water PRF on the local temperature [48, 22]. However, as the water PRF also depends on the magnetic field and local magnetic susceptibility, the PRF shift method needs a calibration step, and the temperature difference is measured instead of the absolute temperature [48, 22].

In the presence of respiratory organ motion, the tissue displacement leads to MR-signal phase changes that are independent of the temperature [21, 5]. The interscan artifacts in MR-thermometry due to motion have mainly two reasons: the spatial transformation and the perturbation in the magnetic susceptibility field [21]. The latter can be analyzed during a pretreatment step, where an atlas of the phase changes is created under the assumption of periodic motion [21]. Another possibility to correct for magnetic field changes is a reference-free approach, where the magnetic field is dynamically recalculated [22]. The spatial transformations can be corrected using a motion model [21].

2.2.4 Treatment of Abdominal Organs

The challenges that arise in the treatment of tumors in abdominal organs such as kidney and liver using HIFU are respiratory motion, high perfusion, steering through the rib cage and associated rib heating. Respiratory motion reduces the treatment efficiency, increases the treatment of healthy tissue and MR monitoring is hindered due to artifacts [43]. There are two fundamental methods to deal with the motion: suppression or tracking [43]. Suppression minimizes the motion, whereas tracking methods continuously relocate the focal point to compensate the motion.

Motion Suppression. There are different methods to suppress the motion. One of them is breath-hold, which can be either passive or active. In the passive breath-hold, mechanical ventilation is used, whereas active breath-hold is achieved by self breath-hold of the patient [43]. Often mechanical ventilation is preferred over self breath-hold as active breath-hold is hard or even impossible to achieve for some patients. Moreover, no general anesthesia can be used, which causes pain [43]. Another method to minimize the motion is single lung ventilation. High-Frequency jet ventilation is a mechanical ventilation method where near static conditions are achieved, but this technique has never been used for HIFU so far [43]. The disadvantage of breath-holding methods is the prolonged treatment time.

Gating. The gating method takes advantage of the repetitive sine-shaped respiratory motion pattern. During an almost stationary part of the respiratory motion cycle,

the tumor is sonicated [22]. The gating window defines the duty cycle. Mechanical ventilation might enlarge the gating window by an optimized breathing rate where the stationary part of the motion is enlarged [43]. However, the gating method neglects the residual motion that is still present during the gating window and long term effects like organ drift. Moreover, due to the small duty cycle, the treatment time is long [22, 43].

Tracking. Another method to overcome the respiratory motion is tracking of the tumor. Here, the focal spot of the HIFU device is actively steered to compensate the respiratory motion [43]. This approach requires tracking the movement of the tumor, which is done using a respiratory motion model. Steering of the focal spot induces an intensity loss at the focal spot, which has to be compensated [43]. As the steering range is limited, the sonication has to be stopped if the target moves outside this range [43]. Using the tracking approach, the problem of steering between the ribs is more complicated, as for each position during the breathing cycle the focal spot has to be steered through the rib cage. Steering requires a phased-array transducer with hundreds of elements, which are separately steered. Nevertheless, the duty cycle is almost 100% and therefore the treatment time can be reduced [43].

Motion Modeling. The tracking approach and the self-scanning method used in this work are both based on a motion model. A motion model takes surrogate data as input and gives a motion estimate as output [41]. The surrogate data should have a strong correlation to the organ motion of interest [41]. There are two approaches to model the respiratory motion pattern: direct and indirect motion modeling [41, 22]. Direct motion modeling is based on target localization on the surrogate data itself. The advantage of this approach is that motion changes are captured, which makes the approach applicable under free-breathing assumptions. However, real-time motion modeling is hard to achieve. The more complex the algorithm, the longer the latency. In indirect motion tracking, the surrogate analysis and motion registration are separated from the treatment. It is assumed that the breathing cycle is periodic, in particular that the motion pattern before and during treatment are the same. Before treatment, a motion model is created. For given surrogate data during treatment, the current state of the breathing cycle is extracted, from which a motion estimate is calculated using the precalculated model. The advantage of the indirect approach is that the calculation time is very short. However, changes in the motion pattern are not captured. In HIFU treatments, the surrogate data are for example MR or ultrasound images.

Steering through the Rib Cage. Steering the focal spot through the rib cage to reach abdominal organs such as the liver and kidney is challenging as the ultrasound velocity differences between the tissue types along the beam path lead to focus aberration, focus shift and reflection [22]. The result is inefficient heating and undesired tissue damage. There are different approaches to deal with this problem. Resection of the ribs was proposed to enlarge the acoustic window [5]. Rib shielding with prefocal acoustic

obstacles was suggested to avoid heating of the ribs [50]. Phased-array transducers allow to sonicate between the ribs [22, 5].

2.2.5 Treatment Planning

The focal spot size of the HIFU device is cigar shaped and measures about 1–3 mm in the transverse and 8–15 mm along the beam axis [34]. Compared to the size of tumors, this is rather small and thus ablating the whole tumor requires several treatment spots. The goal of treatment planning is to find focal spot positions with corresponding beam times and acoustic intensities such that the entire tumor is ablated. Accumulation of a lethal dose inside the tumor must be guaranteed, while surrounding healthy tissue should be treated as little as possible [46]. The lethal thermal dose inside the tissue can be described using the thermal dose formula [51]. The higher the temperature, the less time is needed to induce necrosis to the tissue. For example, a treatment of 60 min at 43°C has the same effect as heating for 15 min at 45°C. The thermal dose formula is described in Section 3.2.

The need for multiple sonication points to cover the whole tumor leads to long treatment times, which is one of the limitations of HIFU. Therefore treatment planning aims to find sonication plans that not only ablate the whole tumor, but also minimize treatment times. Causes of long treatment times are, beside the number of focal points, also healthy tissue safety, perfusion-independent heating and near field heating [3]. To maintain perfusion-independent heating, treatments with the use of small focal zones are used, which prolongs the therapy [3].

Although the temperature induced by focused ultrasound is the highest at the focal spot, the tissue between the focal spot and the device is also subjected to ultrasound waves, meaning that it is moved by mechanical vibrations and thus the temperature is increased. If the pulse duration is short and the power low, this temperature elevation can be neglected. However, if the pulse duration gets longer, the tissue in the near field region is heated to levels which can not be neglected anymore. A possible solution to near field heating is to introduce delay times to allow the healthy tissue in the near field region to cool down [26]. One could have fixed heating and cooling times [19]. However, this might lead to increased treatment times. Another possibility is to apply an approach similar to [44], where the authors optimized the heating and cooling times and shortened the treatment time significantly. When the planning is based on numerical simulation of the Pennes bioheat equation, near field heating is included and thus minimized during optimization [3].

One possibility to plan a treatment is to perform point-by-point ablation, which means that the tumor is covered by moving the focus side-by-side [63]. Here, the treatment time is dependent of the number of pulses and the delay time between the pulses to allow the healthy tissue to cool down [26]. To shorten the treatment time, it is suggested to maximize the necrosed tissue induced by one pulse, which is achieved by increasing the power and the pulse duration [26]. This reduces the number of pulses needed, but near field heating is increased. A compromise has to be found between pulse duration and the induced near field heating [26].

Heat dissipates over time and if the diffusion is exploited, the treatment time can

be shortened. A suggested method to leverage heat dissipation is volumetric ablation, where the focal spot is steered along a prescribed trajectory to increase the ablated volume [22, 35]. Using phased-array transducers, multiple foci can be simultaneously generated or fast temporal switching between different foci is achieved [25]. In [35], the authors electronically steered the focal point along multiple outwards-moving concentric circles. They could improve the treatment time and induce a homogeneous lesion. However, a problem arising in volumetric ablation is the increased near field heating.

In [16], point-by-point and volumetric heating were compared. Here, volumetric ablation was defined as the sonication of points in a predefined order and in a cyclic fashion. The heating time per location was either the same for all points (volumetric ablation) or varied between the positions (fractionated heating). The treatment time of each sonication strategy was optimized. Overall, point-by-point sonication gave the shortest and volumetric ablation the longest treatment times. The reason was that volumetric ablation can be compared to having a large focal zone, resulting in slower temperature rises. Moreover, the near field heating region was enlarged. Although it had been suggested before to reduce the number of focal spots used to shorten the treatment time in [26], the authors of [16] found that increasing the number of focal zones yields shorter treatment times. Using a larger number of focal zones, low and high dosage zones can be avoided, which reduces the needed amount of delivered energy and thus also the treatment time. However, there is a point at which increasing the number of focal zones does not improve the treatment time anymore. Overall, they found that the shortest treatment times can be achieved by axially stacked, collectively optimized point-by-point heating, with a large number of focal zones at optimal spacing and high power [16].

A treatment can be either planned using sequential or simultaneous optimization. In sequential optimization, the treatment is optimized without considering future doses beyond the current pulse's effect [16]. Simultaneous optimization, on the other hand, uses all available knowledge of heating induced by all pulses during a treatment [16]. Using simultaneous optimization, shorter treatment times are expected, as the treatment is optimized at once and all heating effects are included during optimization. However, the drawbacks of this method are the large number of variables and the fact that the tissue's acoustic properties are unknown prior to the treatment. Moreover, changing respiratory pattern during treatment is not taken into account. In [16], the authors found that sequential optimization performs almost as good as simultaneous optimization. The advantage of the simultaneous method becomes most beneficial in regions where thermal interaction is significant, which is the case between neighboring focal points. If the perfusion rate is high, the interaction decreases.

The temperature increase depends on unknown tissue parameters, such as attenuation, perfusion and absorption [25]. To achieve the desired dose, Salomir et al. suggested to use a double spiral trajectory using constant power [49]. In the first spiral, a constant velocity is used. If the tissue parameters were homogeneous over the whole heated area, already the first spiral would induce a uniform dose. Due to local inhomogeneities, this is, however, usually not the case. The second spiral is used to compensate for these inhomogeneities by adapting the velocity of the spiral to the induced temperature, measured using MR-thermometry [49]. In a follow-up work, the

inhomogeneities were compensated with a PID regulation algorithm [42]. The PID controller continuously calculated an error value, here between the measured and desired thermal dose profile, and applies a correction based on proportional (P), integral (I) and derivative (D) terms.

The treatment planning methods described so far used predetermined trajectories of the focal spot, and solely the power, spacing along the trajectory, beam and cooling times are optimized. Full optimization of all the parameters, including trajectory optimization, is difficult due to the large amount of parameters [37]. Moreover, the solution is usually not unique.

Different optimal control approaches were suggested for full optimization, where the norm of the difference between the induced and the desired thermal dose is optimized [62, 37, 3, 38]. Wan et al. used an analytical solution to the Pennes bioheat equation to reduce the computational time [62]. Here, the number of focal spots was predetermined, and it was found that the more foci were placed, the smoother the induced thermal dose profile resulted. A weighted norm difference was used, where the transition region was weighted less than the tumor. Arora et al. found the treatment plan in two steps [3]. In the first step, an optimal power deposition pattern was found to achieve the desired thermal dose. In a second step, the power deposition pattern was then approximated by optimization of the beam times and power values. The focal spot positions were chosen from predetermined positions. Malinen et al. optimized the trajectory of the focal spot without prescribing the scanning path [38]. In a first step, the phases and amplitudes of a phased-array transducer were optimized to get the desired temperature and thermal dose inside the tissue. During treatment, a feedback controller was used to correct the precalculated treatment plan according to temperature feedback from MR measurements.

The simulation of the temperature in the optimal control approaches described above is based on the Pennes bioheat equation, which is mostly solved numerically [37, 3, 38]. Depending on the simulation domain, near field heating is included into simulations and can thus be directly minimized. We will describe the Pennes bioheat equation in the next section.

3 Mathematical Models for HIFU

To plan a HIFU thermal treatment, a temperature model is needed. The HIFU transducer induces an acoustic pressure, leading to a temperature rise. The acoustic pressure as well as the temperature can be described by partial differential equations (PDE). These equations can be solved numerically, or, by using some assumptions and simplifications, they can be solved analytically. In this work, the simulations and the planning are based on an analytical solution.

3.1 Pennes Bioheat Equation (BHTE)

The temperature inside the body can be described by the Pennes bioheat equation [45]:

$$\frac{\partial T(p,t)}{\partial t} = D\nabla^2 T(p,t) - bT(p,t) + KQ(p,t), \tag{3.1}$$

where $T(p,t)$ and $Q(p,t)$ are the temperature rise and the heat source at a given point p and time t, respectively. Moreover, $D = \frac{\kappa}{\rho c}$, where κ is the thermal conductivity, ρ the density, and c is the specific heat of tissue. Furthermore, $b = \frac{wc_b}{\rho c}$, with w the perfusion and c_b the specific heat of blood, and $K = \frac{1}{\rho c}$. The first term represents the rate of change in heat content, the second conduction, the third is the perfusion heat transfer, and the last term is the heat source.

Conduction is the transfer of heat by collision of particles. It plays an important role for focused ultrasound sources with a diameter smaller than the diffusion distance [15]. On the other hand, thermal conduction can be neglected if the heat source is broad or applied slowly. In these cases the heat transfer by perfusion dominates [15]. The passage of blood through capillaries is referred to as perfusion. For rapid heating, perfusion can be neglected [15].

Tissue Properties. To calculate the temperature profile T for a given heat source Q, tissue properties like the density, ultrasonic absorption, specific heat and perfusion have to be known. There are different methods to extract these parameters from MR-thermometry measurements. These mechanisms and methods are briefly described in Chapter 7.

Closed Form Solution to BHTE. In the following, a closed form solution to the Pennes bioheat equation (3.1) is derived following [62]. For convenience, we rewrite Eq. (3.1) as

$$T_t = D(T_{rr} + T_{zz}) - bT + KQ, \tag{3.2}$$

where the point $p = (r, z)$ is written in cylindrical coordinates.

First, the closed form solution during the *power on* period is derived, i.e. $Q \neq 0$. To solve the differential equation (3.2), we first take advantage of the Fourier transform ($\mathcal{F}$) property

$$\mathcal{F}(f_x)(x) = 2\pi i x \mathcal{F}(f)(x).$$

Applying the Fourier transform to the spatial variables r and z gives

$$S_t = -4D\pi^2(R^2 + Z^2)S - bS + Kq,$$

where S and q denote the Fourier transformed temperature function T and heat source Q, respectively. The variables R and Z denote the transformed parameters r and z, respectively. The above equation is a first-order ordinal differential equation (ODE) in t. Under the assumption that at the beginning there is no temperature rise, i.e. $S(R, Z, 0) = T(r, z, 0) = 0$, the solution to the ODE is [1]

$$S(R, Z, t) = K \int_0^t \exp\left[\left(4D\pi^2(R^2 + Z^2) - b\right)(t - \tau)\right] q(R, Z, \tau)\, d\tau.$$

By applying the inverse Fourier transform, we obtain the closed form solution during the *power on* time as

$$T_{\text{on}}(r, z, t) = \frac{K}{4D\pi} \int_0^t \frac{\exp[-b(t-\tau)]}{t-\tau} \iint_{-\infty}^{\infty} \exp\left[-\frac{(r-\alpha)^2 + (z-\beta)^2}{4D(t-\beta)}\right] Q(\alpha, \beta, \tau)\, d\alpha d\beta d\tau. \quad (3.3)$$

During the *power off* period, where the heat source is turned off, i.e. $Q = 0$, the Fourier transform gives

$$S_t = -D4\pi^2(R^2 + Z^2)S - bS,$$

which is again an ODE. The initial condition at $t = 0$ is given to be $T_0(r, z)$, and hence

$$S_0 = S_0(R, Z) = S(R, Z, 0) = \mathcal{F}(T(r, z, 0)) = \mathcal{F}(T_0(r, z)).$$

The solution to the ODE is calculated as

$$S(R, Z, t) = S_0(R, Z) \exp\left[\left(4D\pi^2(R^2 + Z^2) - b\right)\right].$$

By back transformation, we obtain the closed form solution of the temperature during the *power off* time as

$$T_{\text{off}}(r, z, t) = \frac{\exp[-bt]}{4D\pi t} \iint_{-\infty}^{\infty} T_0(\alpha, \beta) \exp\left[-\frac{(r-\alpha)^2 + (z-\beta)^2}{4Dt}\right] d\alpha d\beta. \quad (3.4)$$

Explicit Formula for Gaussian Beam. The integrals given by the closed form solutions Eq. (3.3) and Eq. (3.4) can be solved analytically when assuming a Gaussian shaped temperature profile and heat source, as shown by Wan et al. [62]. A brief description of the derivation is given in Chapter 7.

Numerical Methods to solve the BHTE. The drawback of the analytical solution is that some simplifications are used, like for example the hypothesis that the beam as well as the heat source are Gaussian shaped. Using these assumptions, the near field heating is for example not modeled. Another possibility is to solve the BHTE numerically. For this, the heat source Q is not assumed to be Gaussian shaped, but calculated from the ultrasonic pressure field, given by a differential equation. The advantage of numerical calculation is that, depending on the used pressure model, nonlinear effects as well as near field heating are included into the temperature calculations. However, the drawback is that solving two differential equations numerically is time consuming and thus the treatment planning method has longer calculation times compared to using an analytical solution.

3.2 Thermal Dose

The most accepted model to determine how tissue is affected by temperature is described by the thermal dose model [51]

$$C(p,t) = \int_0^t R^{43-T(p,\tau)} d\tau, \tag{3.5}$$

where the constant R depends on the temperature T as follows:

$$R = \begin{cases} 0, & T < 39°\mathrm{C}, \\ \frac{1}{4}, & 39°\mathrm{C} \leq T < 43°\mathrm{C}, \\ \frac{1}{2}, & 43°\mathrm{C} \leq T. \end{cases}$$

The thermal dose equation estimates the cumulative equivalent minutes at a temperature of 43°C (CEM_{43}). In other words, the effect on tissue of a particular treatment with a given temperature rise is compared to a treatment at a constant temperature of 43°C. The temperature rise is given as input to the thermal dose equation (3.5), which gives then the equivalent minutes at a constant temperature of 43°C. Studies showed that the threshold thermal dosage for tissue to undergo necrosis is between 50 and 240 CEM_{43}, depending on the tissue type [20].

Another measure is given by Rosenberg et al., who found that a lethal thermal dose can be predicted if the maximal temperature is above 54°C [47]. The authors observed that 87.2% of the tissue heated above 52°C received irreversible damage. As a result, a lethal temperature threshold of 54°C was assumed for daily practice [47].

4 Mathematical Tools

The goal of this thesis is to find optimal treatment plans that minimize treatment time and the treatment of healthy tissue. For this, different optimization frameworks have been used. In this chapter, a brief overview of the different mathematical tools is given.

4.1 Sparse Optimization

In sparse optimization, one tries to recover a signal $x \in \mathbb{R}^n$ from only few measurements $b \in \mathbb{R}^m$, where often $m \ll n$. The measurements b and the signal x are related by

$$Ax = b, \tag{4.1}$$

where $A \in \mathbb{R}^{m \times n}$ is a given matrix [58, 39]. The system defined in Eq. (4.1) is underdetermined, meaning that there are fewer equations than variables ($m < n$). Usually, more than one solution exists to such equations. However, if x is sparse, i.e. if most of the entries of x are zero, the signal x can be recovered by solving

$$\arg\min_x \|x\|_0 \quad \text{such that } Ax = b, \tag{4.2}$$

where $\|x\|_0$ counts the number of nonzero entries of a vector x and is given by

$$\|x\|_0 := |\{i \,:\, x_i \neq 0\}|.$$

Despite the notation, $\|\cdot\|_0$ is not a norm. The optimization problem defined by Eq. (4.2) is a combinatorial problem and thus hard to solve [58]. Hence, instead of solving Eq. (4.2), the problem is relaxed to the ℓ_1-optimization problem

$$\arg\min_x \|x\|_1 \quad \text{such that } \|Ax - b\|_2 \leq \epsilon, \tag{4.3}$$

where the ℓ_1-norm is defined as

$$\|x\|_1 := \sum_{i=1}^{n} |x_i|.$$

The problem defined in Eq. (4.3) is denoted as basis pursuit denoise (BPDN) problem, where the parameter ϵ represents the noise level of the data [58]. Problem (4.3) can be used to recover a sparse solution x at the cost of an increasing number of measurements that have to be taken.

In the following, two methods to solve Eq. (4.3) are briefly described, the spectral projected gradient algorithm (SPGL1) and the weighted SPGL1 method.

Spectral Projected Gradient. The SPGL1 algorithm iteratively solves problems of the form [58]

$$\arg\min_x \|Ax - b\|_2 \quad \text{such that } \|x\|_1 \leq \sigma. \tag{4.4}$$

The above problem is called Lasso problem. For appropriate choices of σ and ϵ, the solutions of Eq. (4.3) and Eq. (4.4) coincide. However, typically these values are not known. Note that the Lasso problem (4.4) is easier to solve than the BPDN problem (4.3), as the absolute value $|\cdot|$ is not differentiable at zero. When solving the Lasso problem (4.4), the ℓ_1-norm is not differentiated, instead an ℓ_1-projection is used to guarantee that $\|x\|_1 \leq \sigma$.

The SPGL1 algorithm links the two problems given by Eq. (4.3) and Eq. (4.4) by the function

$$\theta(\sigma) := \|b - Ax^\sigma\|_2, \tag{4.5}$$

and x^σ is the optimal solution to the Lasso problem (4.4) with parameter σ. If the noise level ϵ is known, the root

$$\theta(\sigma) = \epsilon \tag{4.6}$$

has to be found. It can be shown that the function θ is differentiable and has a known derivative, and hence Newton's method can be applied to solve Eq. (4.6). A sequence σ_k is found with the property that $\sigma_k \to \sigma_\epsilon$, with $\theta(\sigma_\epsilon) = \epsilon$ and thus x^{σ_ϵ} is a solution to problem (4.3). More details about the SPGL1 method can be found in [58].

Weighted Spectral Projected Gradient. The WSPGL1 method is a variation of the SPGL1 algorithm [39]. The difference between the two methods is that problems of the form

$$\arg\min_x \|Ax - b\|_2 \quad \text{such that } \|x\|_{1,w} \leq \sigma \tag{4.7}$$

are solved. The difference to the Lasso problem (4.4) is that the weighted ℓ_1-norm is used, which is defined as

$$\|x\|_{1,w} = \sum_i w_i |x_i|,$$

where $w_i \in (0, 1]$ is a weight.

Similar to the SPGL1 algorithm, a sequence of weighted Lasso problems (4.7) are solved for a sequence $\{\sigma_i\}_i$. After the solution x^{σ_i} to Eq. (4.7) has been found, WSPGL1 extracts the set of the k largest entries of x^{σ_i}, denoted by Γ. The weight vector w is then chosen to be

$$w_k = \begin{cases} \omega, & k \in \Gamma, \\ 1, & \text{else}, \end{cases} \tag{4.8}$$

with $\omega \in (0, 1]$. The weight described in Eq. (4.8) is then used in the consequent weighted Lasso problem (4.7) with σ_{i+1}. A detailed description of the WSPGL1 alorithm can be found in [39].

4.2 Optimal Control

In optimal control, the goal is to find a control function u which minimizes a given cost function J. The cost function is minimized if an optimal state v^* is induced by the optimal control function u^*, where differential equations describe how a state v is induced by the control function u. In HIFU treatment planning, the control function is the treatment plan and the state the induced thermal dose, which is calculated by the Pennes bioheat equation and the thermal dose equation. The cost function consists of the treatment time and a term measuring the treatment of healthy tissue, which both should be minimized. Mathematically, this gives an optimization problem of the form

$$\min_u J(u, y) \quad \text{subject to } e(v, u) = 0,\ u \in U_{\text{ad}},\ v \in V_{\text{ad}}, \tag{4.9}$$

where U_{ad} and V_{ad} denote the feasible sets of the control u and the state v, respectively. Moreover, $e(v, u) = 0$ represents a partial differential equation (PDE) or a system of PDEs.

If for each control u a unique solution $v(u)$ exists to the PDE constraint $e(v, u) = 0$, the optimal control problem given by Eq. (4.9) can be written as the reduced problem

$$\min_u J(u, y(u)) \quad \text{subject to } u \in U_{\text{ad}},\ v(u) \in V_{\text{ad}}. \tag{4.10}$$

The reduced problem is then for example solved using the interior-point method described in Section 4.3. A comprehensive introduction to optimal control can be found in [29, 57].

4.3 Interior-Point Method

In this section, we consider optimization problems of the form

$$\min_x f(x), \quad \text{subject to } h(x) = 0,\ g(x) \leq 0, \tag{4.11}$$

where $x \in \mathbb{R}^n$ and $f : \mathbb{R}^n \to \mathbb{R}$, $h : \mathbb{R}^n \to \mathbb{R}^l$ and $g : \mathbb{R}^n \to \mathbb{R}^m$ are twice differentiable functions. The Lagrangian of the problem (4.11) is defined as [9]

$$\mathcal{L}(x, \lambda) = f(x) + \sum_{i=1}^{m} \lambda_{g,i}\, g_i(x) + \lambda_h^T h(x). \tag{4.12}$$

Barrier Method. For solving Eq. (4.11), first the inequality constraint is shifted to the objective, such that Newton's method can later be used to solve the problem. This results in the approximate problem

$$\min_x f_\mu(x) = \min_x f(x) - \mu \sum_{i=1}^{m} \log(-g_i(x)), \quad \text{subject to } h(x) = 0. \tag{4.13}$$

The solution to the approximate problem (4.13) converges to a solution of Eq. (4.11), for $\mu \to 0$. The above problem (4.13) can be solved by Newton's method, which is

used to find a root of a function, i.e. find the solution to $F(x) = 0$ for a given F. The root finding problem is defined by the first order optimality conditions of Eq. (4.13), which are given as [9]

$$\begin{aligned} \Delta\mathcal{L}(x, \lambda) &= 0, \\ -\lambda_i g_i(x) - \mu &= 0,\ i = 1, \ldots, m, \\ h(x) &= 0, \\ g_i(x) &\leq 0, \\ \lambda &\geq 0. \end{aligned} \tag{4.14}$$

The barrier method consists of solving a series of problems (4.13) defined by μ_i, where $\mu_i \to 0$. Each of the problems is solved by applying Newton's method to the first order optimality conditions given by Eq. (4.14). More details about the barrier methods, for example how to choose μ_i and stopping criteria, can be found in [9]. Note that if the constraints $u \in U_{\text{ad}}$ and $v \in V_{\text{ad}}$ of the optimal control problem described in Section 4.2 can be written as constraints of the type $h(x) = 0$ or $g(x) \leq 0$ for some functions h and g, it can be solved using the interior-point method.

Interior-Point Algorithm for Non-Convex Optimization. For non-convex optimization, the barrier method may converge to non-stationary points (i.e. points with non-zero derivative) [61]. There are different methods to adapt the barrier method to non-convex optimization. One is to combine line search and trust region steps [61], which will be very briefly described in this paragraph. It is based on the barrier method, where first the optimality conditions are solved using a Newton step, and the steplength is determined using a backtracking line search. The backtracking line search updates the steplength until a sufficient decrease is obtained. If the line search converges to a non-stationary point, the steplength converges to zero [61]. This fact is used as a criterion on where the line search might not be successful. If the steplength gets too small, the line search step is replaced by a trust region step. The advantages of the trust region step is that it is robust even when the problem is ill-conditioned [61, 11]. The trust region step is explained in the next paragraph.

SQP Iteration with Trust Regions. The problem (4.11) can be solved using a sequential quadratic programming (SQP) approach with a trust region instead of using Newton's method [11]. Given a current guess of the problem (4.11), the idea of the trust region algorithm is to use an approximate model near the current point. This approximate problem is then solved and the solution is used as next iterative point [64]. In the case of the proposed algorithm by [61, 11], the Lagrangian is approximated by a quadratic model, called SQP. The approximation by the SQP model is only trusted in a region near the current iterate, called the trust region. Depending on how well the current model fits the actual problem at the current guess, the trust region can be enlarged or is reduced. General details on trust region methods can be found in [64], and the exact formulation of the SQP step used for non-convex problems is described in [11].

4.4 Multi-Objective Optimization

The treatment planning optimization problem consists of several different objectives, namely the treatment time and the overtreatment term. This results in a multi-objective optimization problem, having the form:

$$\min_{x\in\mathcal{X}} f(x) = \min_{x\in\mathcal{X}} \begin{pmatrix} f_1(x) \\ \vdots \\ f_k(x) \end{pmatrix}, \tag{4.15}$$

where $x \in \mathbb{R}^n$, $f_i : \mathbb{R}^n \to \mathbb{R}$ are the different objectives to be minimized, and $\mathcal{X} \subseteq \mathbb{R}$ is the feasible set. The above formulation is in general not clear, as normally no solution x exist that minimizes all constraints simultaneously [40]. Hence, Pareto optimality is used to describe optimal solutions to problem (4.15). A point $x \in \mathcal{X}$ is called Pareto optimal, if there exist no $y \in \mathcal{X}$ such that $f(y) \leq f(x)$. Here, the notation $a \leq b$, for some vectors a and b, means that $a_i \leq b_i$ and $a \neq b$. The set of Pareto optimal solutions is called Pareto frontier.

A way to obtain Pareto optimal solutions is to use the weighted sum method, which transforms the vector valued function f into a scalar objective function [28, 40]

$$\min_{x\in\mathcal{X}} \sum_{i=1}^{n} w_i f_i(x). \tag{4.16}$$

If the weights w_i are positive, then minimizing Eq. (4.16) yields a Pareto optimal solution [28, 40]. However, if the Pareto frontier is not convex, not all Pareto optimal solutions can be found using the weighted sum method [40]. In particular, there are Pareto optimal solutions x for which no weight vector w exists such that problem (4.16) provides the solution x.

A possible interpretation of the weight choice is the preference between the different objectives. Higher weights indicate a higher preference. However, not only the choice of preferences might be difficult, but also the weights might not represent the supposed preferences as the magnitudes of the different objective functions can have huge differences [40]. A possible solution to this problem is to normalize each objective such that all have similar magnitudes. In this case, the weights are written as

$$w_i = \frac{p_i}{\eta_i}, \quad i = 1, \ldots, n,$$

where p_i is the preference and η_i the normalization weight for objective i. Normalization by itself can be a hard problem as often the range of the objective functions is not fully known. Different normalization strategies can be found in [28].

5 Feasibility Study of the Self-Scanning Approach

The publication in this chapter describes a first feasibility study of the self-scanning approach. We assume that the tissue undergoes necrosis if it is heated above 54°C, resulting in a linearized dose model. Moreover, we simplify the temperature calculation by assuming that no diffusion over time occurs. The respiratory motion pattern is assumed to be periodic. With these assumptions, the problem of finding an optimal treatment plan can be stated as a sparse optimization problem, which is solved using the WSPGL1 algorithm. The performance of the self-scanning method is compared to the tracking approach. We obtain shorter treatment times with the self-scanning approach, while the treatment of healthy tissue is slightly increased.

Publication. The following paper was published on the 18th May 2016 in the journal *Physics in Medicine & Biology (PMB)*.

OPEN ACCESS
IOP Publishing | Institute of Physics and Engineering in Medicine Physics in Medicine & Biology
Phys. Med. Biol. **61** (2016) 4247–4267 doi:10.1088/0031-9155/61/11/4247

Leveraging respiratory organ motion for non-invasive tumor treatment devices: a feasibility study

Nadia Möri[1], Christoph Jud[1], Rares Salomir[2] and Philippe C Cattin[1]

[1] Department of Biomedical Engineering, University of Basel, Switzerland
[2] Faculty of Medicine, Radiology, University of Geneva, Switzerland

E-mail: nadia.moeri@unibas.ch

Received 8 December 2015, revised 24 March 2016
Accepted for publication 18 April 2016
Published 18 May 2016

Abstract

In noninvasive abdominal tumor treatment, research has focused on minimizing organ motion either by gating, breath holding or tracking of the target. The paradigm shift proposed in this study takes advantage of the respiratory organ motion to passively scan the tumor. In the proposed self-scanning method, the focal point of the HIFU device is held fixed for a given time, while it passively scans the tumor due to breathing motion. The aim of this paper is to present a treatment planning method for such a system and show by simulation its feasibility. The presented planning method minimizes treatment time and ensures complete tumor ablation under free-breathing. We simulated our method on realistic motion patterns from a patient specific statistical respiratory model. With our method, we achieved a shorter treatment time than with the gold-standard motion-compensation approach.

The main advantage of the proposed method is that electrically steering of the focal spot is no longer needed. As a consequence, it is much easier to find an optimal solution for both avoiding near field heating and covering the whole tumor. However, the reduced complexity on the beam forming comes at the price of an increased complexity on the planning side as well as a reduced efficiency in the energy distribution.

Although we simulate the approach on HIFU, the idea of self-scanning passes over to other tumor treatment modalities such as proton therapy or classical radiation therapy.

Original content from this work may be used under the terms of the Creative Commons Attribution 3.0 licence. Any further distribution of this work must maintain attribution to the author(s) and the title of the work, journal citation and DOI.

0031-9155/16/114247+21$33.00 © 2016 Institute of Physics and Engineering in Medicine Printed in the UK

Keywords: self-scanning, treatment planning, HIFU in liver, simulation of treatment plans

(Some figures may appear in colour only in the online journal)

1. Introduction

High intensity focused ultrasound (HIFU) is a well-known non-invasive thermal ablation modality for tumor treatment which is widely accepted for about a decade (Schwenke *et al* 2015, ter Haar *et al* 1989, Cline *et al* 1992). For image guidance during HIFU sonication, ultrasound (Kennedy 2005) as well as magnetic resonance (MR) can be used (Hynynen 2010, Petrusca *et al* 2011, 2013). MR not only provides images of the tumor and its motion, but is also used for temperature mapping (Hynynen 2010). With MR thermometry, the focal spot position and the heating procedure are monitored. Further, the thermal dose is calculated to determine the tissue damage (Hynynen 2010, Wijlemans *et al* 2012). MR-guided HIFU has been successfully applied for tumor ablation in immobile organs, such as uterus, prostate, breast and brain (Hynynen 2010, Ellis *et al* 2013). However, HIFU treatment of abdominal organs, such as kidney and liver, remains challenging due to respiratory motion and organ drift (Von Siebenthal *et al* 2007).

Today, there are two established principles to address the problems of liver motion in HIFU sonication: the respiratory-gated and the continuous motion-compensation sonication strategies (De Senneville *et al* 2012). In the former ones, an almost stationary part of an adult breathing cycle is exploited. Within a temporal window called gating-window of 1–2 s, where the liver remains approximately still, the acoustic energy is periodically deposited (Auboiroux *et al* 2014). The disadvantages of the respiratory-gated method is the prolonged treatment time and the negligence of the remaining motion during the gating-window.

Continuous motion-compensation sonication, in contrast, is based on the idea of continuously readjusting the focal point position to the current tumor position in order to prevent both undesired tissue damage and energy spread (Ries *et al* 2010, Arnold *et al* 2011, Celicanin *et al* 2014, Holbrook *et al* 2014). The advantage of this method compared to the respiratory-gated approach is the near 100% duty cycle, which results in a shorter treatment time. However, in order to steer the focal spot of the HIFU device, a phased-array-transducer with hundreds or even thousands of elements is required, each having its own amplifier and delay time. This complicates the electrical design of the device and is expensive. Moreover, the lateral steering causes an intensity decay at the focal spot (Auboiroux *et al* 2011).

A further challenge of the motion-compensation sonication is the prediction of the liver motion to actively steer the HIFU beam. The idea of direct motion tracking is to detect the tumor in real-time and adjust the focal spot accordingly. Due to processing latency, the tumor position has to be anticipated to provide direct motion tracking (Ries *et al* 2010, Celicanin *et al* 2014, Preiswerk *et al* 2014). Preiswerk and Cattin (2015) used a non-linear Gaussian process regression method to predict organ motion based on a model-topology independent external respiratory signal.

As solid tumors are much larger than the focal spot of the HIFU device, ablating the whole tumor requires several treatment spots. The development of a sonication plan that reduces the treatment time and generates a uniform lesion has been addressed before in immobile tissue (Salomir *et al* 2000, Mougenot *et al* 2004, Hui *et al* 2009, Zhou 2013). The basic idea is to sonicate points in a regular grid, such as a spiral pattern or raster scanning.

The ultrasound waves emitted by the HIFU device cause a pressure field which induces a temperature rise at the focal spot. The temperature can be described by Pennes bio-heat equation (Cline *et al* 1992, Wissler 1998). The most accepted model to determine how tissue is

affected by the induced temperature rise is the thermal dose (Sapareto and Dewey 1984). The thermal dose equation estimates the equivalent minutes at a temperature of 43 °C. Another study (Rosenberg *et al* 2013) shows that a temperature of 54 °C can be sufficient to induce necrosis.

In this paper, we present a planning method for the proposed self-scanning approach and show its feasibility by simulation. The novel method takes advantage of the perpetual respiratory motion to passively scan the tumor. In other words, we are placing the static focal point of the HIFU into the tumor. The motion caused by breathing moves the tumor through this focal point. Based on the motion model of (Preiswerk and Cattin 2015), we anticipate at which time point tumor tissue is located under the focal spot and thus modulate the HIFU intensity based on this information. Once the tumor has been ablated along the self-scanned trajectory, the focal spot is relocated to a different but static position within the body. The main advantage of this principle is that no electronic steering of the focal spot is needed. Actively compensating for the motion can collide with both avoiding near field heating and covering the sonication volume. As a consequence, it is much easier to find an optimal solution for beam forming with the proposed self-scanning method. Moreover, the amplitude of the respiratory motion is comparable or larger than the steering range of a standard phased-array-transducer. Thus, the spatial extension of the sonicated pattern in the tumors referential is equal or larger with self-scanning techniques than with electronic steering of the beam. However, the reduced complexity on the beam forming comes at the cost of an increased complexity during the planning stage and a reduced efficiency in the energy distribution. With the proposed method, we combine the advantages of the respiratory-gated and motion-compensation method: a fixed focus can be used and a high duty cycle is achieved. Moreover, since with the proposed self-scanning approach no lateral steering of the focal spot is required, position-dependent decay of the focal spot intensity during lateral steering is avoided.

In the following, we present a method to determine optimal sonication plans for such a system ensuring complete tumor ablation. In section 2, we introduce a mathematical formulation of our model and show how to solve it. The model minimizes treatment time and handles complex non-rigid motion and non-time dependent diffusion. In section 3, we simulated our method on a patient specific statistical respiratory motion model. We compared the results to a continuous motion-compensation approach. The different approaches were evaluated in terms of efficiency and treatment time. The efficiency coefficient is a measure to determine how emitted energy can be exploited. With simulation, we showed that our method provides feasible treatment plans for the proposed self-scanning approach, which yields a faster treatment time than the continuous motion-compensation approach.

2. Method

In the following section, we show how a treatment that takes advantage of the respiratory motion can be planned. The task is to find appropriate tumor points which are sonicated by the HIFU device. The focal spot will stay fixed during a given time to achieve a precalculated temperature rise. During this phase, different liver tissue will pass through the focal spot. The points and the corresponding temperature rises have to be chosen such that the whole tumor is ablated. To avoid overtreatment, the energy has to be distributed mainly on the tumor and as few as possible energy should be spread on healthy tissue. Under these conditions, the treatment time is minimized. The treatment time consists of beam- and changing time. The beam time is the overall time where the HIFU device is focused on one point. The HIFU system used with the self-scanning method is able to electrically steer the focal spot in depth along

the acoustic axis. For the other two directions, mechanical displacement is used. Hence, the focal spot can be changed fast along the acoustic axis and slower in the other two directions. The time needed to change in the two slower directions is called changing time.

The sonication plans are calculated before treatment. As described in the next section, we assume a non-rigid, but repetitive motion and breathing pattern. We therefore calculate a lookup table that tells us at every time point which position inside the target has to be sonicated.

2.1. Assumptions

In this first proof of principle study, we assume that there is no heat diffusion over time. This means that a liver point will only change its heat value if it is inside the focal spot of the HIFU device for a certain time during treatment. In other words we assume linear dose accumulation. We will also not consider heat changes due to blood perfusion and metabolic processes. Note that volumetric ablation is less sensitive to diffusion and perfusional sink effects as the thermal build up is rather smooth compared to sharp spatial profiles generated by a fixed focus in static tissue (Köhler *et al* 2009). Further, we assume that the liver motion stays periodic over time. In other words, we assumed that no organ drift occurs and that the breathing pattern of the patient stays constant during treatment. This means that the breathing pattern repeats itself after each breathing cycle. This corresponds to the assumption of a regular breathing pattern of the patient. Note however, that our model can handle complex non-rigid breathing motion.

In order to determine which tissue has been ablated, the most accepted model is the thermal dose equation (Sapareto and Dewey 1984). However, Rosenberg *et al* (2013) showed that tissue is ablated when heated above a temperature of 54 °C, which we will use in this study.

The above assumptions are simplifications of the real problem in order to show the feasibility of the self-scanning approach. In our ongoing research, we will include diffusion over time as well as perfusion. Moreover, we plan to switch to the thermal dose model.

2.2. Mathematical model

For the mathematical formulation, we consider three sets of points in different coordinate systems. The first set consists of points that might be heated up during the treatment. These points may be inside or outside the tumor and are in the liver coordinate system. We will call this set liver points P_l. The second set includes the target points, which form a subset of the liver points, $P_\mathrm{t} \subseteq P_\mathrm{l}$. The target points include tumor points as well as some surrounding tissue points. To be sure that all of the tumor cells will be ablated, some surrounding tissue of the tumor has to be treated as well (safety margin). The goal of the HIFU treatment is to heat the target points and ablate them. The last set consists of points in the world coordinate system which can be focused by the HIFU device. We will refer to these as world points P_w. The main difference between the two sets P_l and P_w is that the liver points will move in the world coordinate system during breathing, whereas the points from the second set are still.

On the basis of speed and direction of the liver movement, we will set up a cover matrix M similar as in Trofimov *et al* (2005). This matrix indicates which liver points will be heated during free-breathing when sonicating a certain point in the world coordinate system. Each matrix column j represents the heat profile of all the liver points after a breathing cycle when a world point p_j is sonicated. These heat profiles can be thought of as cylinders. The shape of a cylinder is determined by the liver motion at the specific location (length and direction) and the focal spot size (diameter). A cylinder represents the tissue which is heated during one breathing cycle when a certain world point is sonicated. In figure 1, a schematic 2D setup is

shown. In this case, a column of the covermatrix is drawn as a rectangle that represents the treated liver points. For simplicity, the motion of the liver shown in figure 1 is linear. In fact, the motion is nonlinear and the rectangles would have a more complex form. Note however, that our model handles complex non-rigid breathing motion. The task in finding a feasible treatment plan can be formulated as choosing appropriate cylinders which cover the whole tumor. Mathematically, this corresponds in finding a vector $x \in \mathbb{R}^m$, which has positive values at the positions where the corresponding cylinders are part of the treatment plan. Note, however, that all the cylinders represent a heat profile, and thus there have to be some overlaps of the cylinders to make sure that all of the target points will be ablated. Moreover, the cylinders are banana-shaped due to the ellipsoidal breathing motion.

Suppose we have n liver points $P_\mathrm{l} = \{l_i\}_{i=1}^n$, m world points $P_\mathrm{w} = \{p_j\}_{j=1}^m$ and target points $P_\mathrm{t} \subseteq P_\mathrm{l}$. The cover matrix $M \in \mathbb{R}^{n\times m}$ is defined as

$$M_{ij} = \begin{cases} I(i,j), & \text{if } l_i \text{ is inside the focal spot when } p_j \text{ is sonicated,} \\ 0, & \text{otherwise,} \end{cases} \tag{1}$$

where $I(i,j)$ is the total temperature rise at liver point l_i during one breathing cycle when focusing world point p_j. Note that for $x \in \mathbb{R}_+^m$, the values of Mx represent how much the temperature rises at each liver point, when p_j is sonicated by the HIFU device with intensity x_j, for $j = 1, ..., m$. We assume that tissue is ablated when heated above a temperature of 54 °C (Rosenberg *et al* 2013). The goal is therefore to provide a minimal temperature rise of $\alpha = 18$ °C to each $l_i \in P_\mathrm{t}$ and simultaneously minimize the temperature rise for points outside the target. The target vector $T \in \mathbb{R}^n$ is defined as:

$$T_i = \begin{cases} \alpha, & \text{if } l_i \in P_\mathrm{t}, \\ 0, & \text{otherwise.} \end{cases}$$

To ablate the target, we want to find $x \in \mathbb{R}_+^m$ that satisfies

$$Mx \geqslant T. \tag{2}$$

We call the solution x to the above equation sonication or treatment plan.

We assume that the temperature rise induced by the HIFU device can be approximated with a Gaussian blurred ellipsoid with deviations σ_z in parallel direction, and σ_r perpendicular to the acoustic axis. The formula of $I(i,j)$ used in the definition of the covermatrix M in equation (1) is as follows:

$$I(i,j) = v_i \sum_{t=t_\mathrm{in}}^{t_\mathrm{ex}} \exp\left(-\frac{(l_i^r(t) - p_j^r)^2}{2\sigma_r^2}\right) \exp\left(-\frac{(l_i^z(t) - p_j^z)^2}{2\sigma_z^2}\right), \tag{3}$$

where $(l_i^r(t), l_i^z(t))$ denotes the cylindric liver point coordinates l_i at time t, (p_j^r, p_j^z) the cylindric coordinates of world point p_j, t_in is the time of inhalation, t_ex marks exhalation, and v_i is a normalization constant. We normalize the matrix row-wise with the constant v_i such that $\max_{1\leqslant k\leqslant n}(Me_i)_k = \alpha$, for $i = 1, ..., m$ and $\{e_i\}_i$ the standard basis of $\mathbb{R}^m$. Hence, the maximal temperature rise that can be delivered by focusing a certain point p_j with intensity $x_j = 1$ yields the lethal temperature rise of 18 °C.

2.3. Optimization

The beam time is related to the number of points that have to be sonicated to ablate the entire target volume, i.e. the non-zero entries of x. Hence, we want to minimize equation (2) over the

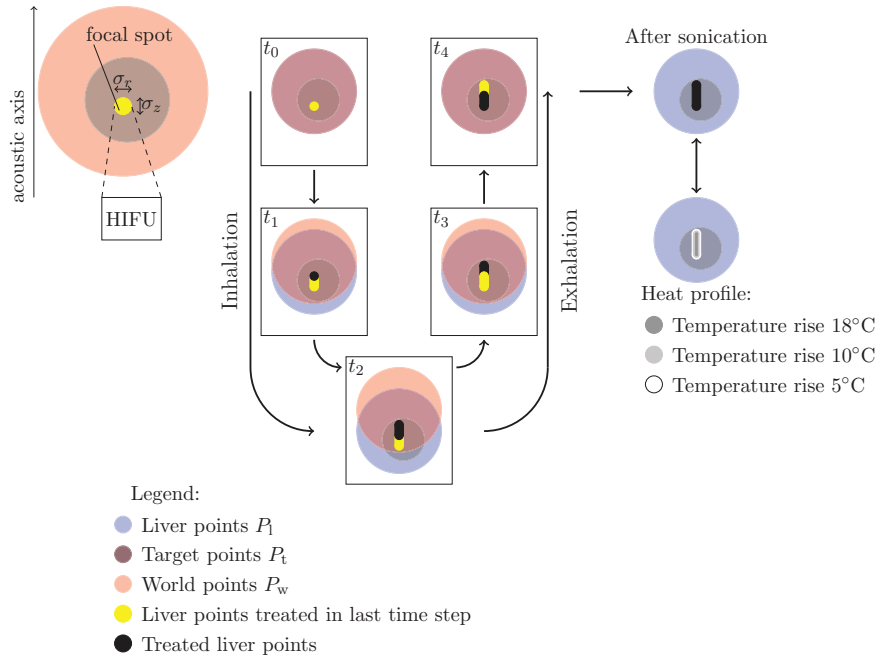

Figure 1. Scheme of the liver motion and the different point sets.

number of non-zero entries of x, which is the ℓ_0-norm. However, the minimization problem with the ℓ_0-norm is an NP-hard problem (Natarajan 1995) and we thus minimize equation (2) over the ℓ_1-norm of x, which is a good approximation.

$$\min_{x \geqslant 0} \|x\|_1 \text{ subject to } Mx \geqslant T. \tag{4}$$

Note that when minimizing $\|x\|_1$, overtreatment outside as well as inside the target is minimized. Here $x \geqslant 0$ means that $x_k \geqslant 0 \; \forall \, k$, and the ℓ_1-norm is defined as

$$\|x\|_1 = \sum_{k=1}^{m} |x_k|.$$

The above equation can be stated as a linear programming problem in the following way:

$$\min_{x \geqslant 0} f^T x \text{ subject to } Mx \geqslant T, \tag{5}$$

where $f = (1, \ldots, 1)^T$, T, and M are defined as in section 2.2. Note that $f^T x$ is another formulation for $\|x\|_1$, if $x \geqslant 0$. The advantage of this approach is that the solution will fulfill the inequality constraints exactly. The ablation of the whole target volume is thus guaranteed. However, the disadvantage of the linear programming algorithm is its computational complexity, which is $\mathcal{O}(m^{3.5})$ (Robere 2012), where m is the number of variables (in our case, $m \approx 63\,000$).

To reduce the complexity, the minimization problem in equation (4) can also be stated in an unconstrained version, which yields a convex problem:

$$\min_{x \geqslant 0} \|x\|_1 + \lambda \, \|Mx - T\|_2^2, \tag{6}$$

with $\lambda > 0$. The above formulation is a Lagrange Multiplier formulation of the compressed sensing problem, which can be minimized with the weighted spectral projected gradient algorithm (wspgl1) proposed by Mansour (2012). The wspgl1 algorithm has a complexity of $\mathcal{O}(m)$ (Birgin *et al* 2014). However, the numerical solution of the ℓ_1-formulation in equation (6) will not fulfill the equality constraint exactly. This leads to a treatment plan that does not completely ablate the target volume. To get a feasible sonication plan which ablates the whole target volume, the solution $\tilde{x}$ to equation (6) needs to be scaled, which leads to a non-optimal sonication plan.

For the scaling, we define the index sets $J_k = \{i : M_{ki} \neq 0\}$, for $k \in \{j : (M\tilde{x})_j < \alpha,\ l_j \in P_t\}$ and rescale $\tilde{x}_i$ for $i \in \cup_k J_k$ by

$$x_i = \frac{\alpha \tilde{x}_i}{\min_{\{k\,:\,i \in J_k\}} (M\tilde{x})_k}. \tag{7}$$

If $i \notin \cup_k J_k$, no scaling is needed. For $1 \leqslant i \leqslant m$ it holds that $(Mx)_i \geqslant (M\tilde{x})_i$. For the undertreated points l_k with $k \in \{j : (M\tilde{x})_j < \alpha,\ l_j \in P_t\}$, we have after scaling

$$(Mx)_k = \sum_{i \in J_k} M_{ki} x_i = \sum_{i \in J_k} \frac{\alpha M_{ki} \tilde{x}_i}{\min_{\{k\,:\,i \in J_k\}} (M\tilde{x})_k} \geqslant \frac{\alpha (M\tilde{x})_k}{\min_k (M\tilde{x})_k} \geqslant \alpha.$$

Thus, the minimal temperature rise inside the target volume is α and the scaled solution x thus ablates the whole target volume. Note that it is possible that $(M\tilde{x})_k < (Mx)_k$ for $k \notin \{j : (Mx)_j < \alpha\}$. Hence, the scaling not only ensures complete target volume ablation, but it also enhances overtreatment.

In practice, the treatment plans have to be adjusted during treatment due to unpredictable organ drift and changing breathing cycle of the patient during treatment. With these changes in the respiratory motion, the calculated treatment plans have to be adjusted to guarantee complete target volume ablation. Therefore, the shorter computation time of the compressed sensing approach in equation (6) would be preferred.

2.4. Reducing overtreatment

There are two different kinds of overtreatment that occur: treating healthy tissue outside of the tumor and heating target volume tissue above the lethal temperature rise α. Both types of overtreatment should be avoided, not only to minimize treatment time, but also to avoid unwanted tissue damage. When the induced temperature rise inside the target is too high, the tissue can start to boil, which is unwanted. To avoid treating tissue outside the target, the HIFU device is turned off when healthy tissue is exposed. To account for this, the covermatrix is slightly changed to

$$M^{\mathrm{f}}_{ij} = v_i \sum_{t \in S_j} \exp\left(-\frac{(l^r_i(t) - p^r_j)^2}{2\sigma_r^2}\right) \exp\left(-\frac{(l^z_i(t) - p^z_j)^2}{2\sigma_z^2}\right), \tag{8}$$

with the same notation as in equation (3). The set S_j denotes the time where most of the points inside the focal spot are target tissue. In the specific case, if the target volume is a sphere, S_j can be defined as $S_j = \{t_{\mathrm{in}} \leqslant t \leqslant t_{\mathrm{ex}} : \| p_j - m(t) \|_2^2 \leqslant R\}$, where $m(t)$ denotes the target center coordinates at time t, and R is the radius around the target center in which the HIFU device is allowed to treat tissue.

To reduce overtreatment inside the target, first a treatment plan x has to be calculated by equations (5) or (6). Then, the breathing cycle is split into p time steps $\{[t_{\mathrm{in}} = t_0, t_1], ..., [t_{p-1}, t_{\mathrm{ex}} = t_p]\}$.

A new covermatrix is calculated which indicates the temperature rise induced by the HIFU device during this shorter time periods. When thinking of cylinders, the time splitting means that we divide the height of each cylinder into p smaller ones. With the splitting, another minimization problem has to be solved to determine the temperature rises at the different time steps. Let $B = \{i\colon x_i > 0\}$ denote the indices of the points that are sonicated in the treatment plan x and $a = p\cdot|B|$. Let $f\colon \{1, ..., |B|\} \to B$ be an enumeration of the set B, define $q_k = \lceil \frac{k}{p} \rceil$, and $t_k = \mathrm{mod}(k+1, p)$. The covermatrix $M^s \in \mathbb{R}^{n\times a}$ is defined as

$$M^s_{ik} = v_i \sum_{t=t_k}^{t_{k+1}} \exp\left(-\frac{(l_i^r(t) - p^r_{f(q_k)})^2}{2\sigma_r^2}\right)\exp\left(-\frac{(l_i^z(t) - p^z_{f(q_k)})^2}{2\sigma_z^2}\right).$$

The minimization problem to determine the temperature rise at the different time steps can be formulated as

$$\min_{x\geqslant 0} \|M^s x\|_1 \text{ subject to } M^s x \geqslant T. \tag{9}$$

Note that if we would not calculate a solution x first, the minimization problem in equation (9) had $p \cdot n$ variables. With the knowledge of a treatment plan, this number can be reduced to $p\cdot|B|$.

2.5. Time measurement

To estimate the beam time, we assume that we need 5 breathing cycles to induce the lethal temperature rise α. In other words, a temperature rise of 3.6 °C can be achieved in one breathing cycle. Hence, for the treatment plan x, the beam time can be calculated as

$$t_{\text{beam}} = \sum_{i=1}^{m} \lceil 5 \cdot x_i \rceil. \tag{10}$$

The treatment time additionally depends on the time needed to change the HIFU device position. The time needed to change with the mechanical displacement in the two slower directions is denoted by c, the electric steering along the acoustic axis can be neglected. If the fast direction is along the x-axis, the time function for a change between two points $P_1 = (x_1, y_1, z_1)$ and $P_2 = (x_2, y_2, z_2)$ is as follows:

$$t_{\text{change}}(P_1, P_2) = \begin{cases} 0, & \text{if } y_1 = y_2 \text{ and } z_1 = z_2, \\ c, & \text{otherwise.} \end{cases} \tag{11}$$

The total changing time is $N \cdot c$, if we have to perform N mechanical displacements. Therefore, we check how many different x-coordinates occur among the focus points of the sonication plan in order to calculate the changing time.

2.6. Efficiency coefficient

In order to compare our methods, we calculate the conversion efficiency η. The efficiency coefficient measures how much energy is wasted by overtreatment. Overtreatment occurs when tissue outside the target is treated or when target tissue is heated above α. The formula for η is as follows:

$$\eta = \frac{E_{\text{out}}}{E_{\text{in}}} = \frac{\|T\|_1}{\|Mx\|_1}, \tag{12}$$

where E_{in} is the energy that is put inside the patient by the HIFU device, and E_{out} is the energy that can be used to ablate the target. Note that E_{out} is the minimal energy needed to ablate the target, which is $\|T\|_1$. The efficiency of the optimal solution is $\eta_{opt} = 1$.

2.7. Continuous motion-compensation method

To evaluate the different methods, we compare the performance of the results to a continuous motion-compensation approach. In the motion-compensation approach, a covermatrix which respects the focal spot steering is computed. As a consequence, the focal spot range is smaller and the temperature rise is higher as compared to the self-scanning approach. Moreover, we modeled the intensity decay at the focal spot during steering with a Gaussian decay in the perpendicular direction to the acoustic axis of the HIFU device (Auboiroux *et al* 2011). Along the acoustic axis, the intensity decay can be neglected. We assumed that the highest intensity can be achieved at the target center, and that the deviation σ_I of the Gaussian is 12 mm. In the following, the continuous motion-compensation approach is referred to as *ContMotion*.

3. Results

As mentioned in section 2.3, we consider two different optimization problems, a compressed sensing and a linear programming approach. With a different choice of the point sets, the compressed sensing method is split into two different methods, *OT* and *WL*, which will be explained in the next section 3.1. In sections 3.3–3.9, the results of our simulations are explained. We evaluated the treatment time and the energy distribution efficiency. Further, we looked at sagittal and axial slices through the liver and which temperature rise is induced into the target points.

We tested our methods on realistic liver breathing motion data using a patient specific statistical respiratory motion model (Preiswerk and Cattin 2015). We set the target to be a sphere inside the liver such that all the energy delivered by the HIFU device will be emitted into the liver. The target with a radius of 15 mm is located at the liver dome, where the motion is non-rigid.

If nothing else is mentioned, the results in the following are obtained by minimizing with covermatrix M as defined in equation (1) with $I(i, j)$ defined in equation (3).

3.1. Choice of point sets

We made the following choice of the three point sets: P_w consists of target points, since we do not want to sonicate healthy tissue. For the liver points we had two different approaches. The first one was to consider liver points which fulfill $P_t \subsetneq P_l$. This leads to a minimization not only inside, but also outside the target. Therefore, as few as possible energy is wasted on healthy tissue. We refer to this method as *whole liver method* (*WL*). The second approach was to consider solely target points as liver points, i.e. $P_l = P_t$. In other words, we exclusively optimize inside the target. The advantage of this approach is that the temperature profile inside the target is more homogeneous. We call this method *only target method* (*OT*). The two different methods *WL* and *OT* are solved with wspgl1. For the *linear programming method* (*LinProg*), the choice of the liver point set does not matter. Both suggested choices of liver points achieved similar results. A summary of the methods can be seen in table 1.

Table 1. Summary of the different methods.

	Method	Liver points	Algorithm
Self-scanning	*WL*	$P_t \subsetneq P_l$	wspgl1
	OT	$P_t = P_l$	wspgl1
	LinProg	$P_t \subseteq P_l$	Linear programming
Focal spot steering	*ContMotion*		Linear programming

3.2. Focal spot size

The beam time additionally depends on the focal spot size of the HIFU device, σ_z and σ_r. In figure 1, the two parameters are shown. Notice that in Figure 1, the focal spot is drawn as a circle, but in fact has an ellipsoidal shape and therefore σ_z and σ_r are not equal. The focal spot size along the acoustic axis is denoted by σ_z, σ_r denotes the size perpendicular to the acoustic axis. The smaller the focal spot, the longer it takes to ablate the target. On the other hand, for smaller focal spot size the method is more flexible: When treating a point near the target border, less healthy tissue will be treated with a narrower focal spot. We tried different values of σ_z and σ_r to see the influence on the treatment time and the efficiency. The ratio between the two deviations σ_z and σ_r is constant and given by the HIFU device (Cline *et al* 1994). Here, we assume that the ratio $\sigma_z : \sigma_r$ is equal to 5.

3.3. Treatment time

The beam-, changing- and total treatment time of the different methods are shown in figure 2. The duration in figure 2(a) is calculated from the sonication plan x as described in equation (10). It indicates how long the beam time lasts, measured in breathing cycles. It can be seen that the number of breathing cycles used decreases with increasing focal spot size. The reason is that more tissue can be treated if the focal spot size increases. Therefore, less points have to be sonicated to cover the whole target. This yields a shorter beam time.

Figure 2(b) shows how many time the HIFU device has to change its position. The number of changes was calculated by equation (11) with $c = 1$. Notice that when setting $c = 1$ in equation (11), the changing time and the number of changes are in fact the same. Recall that the continuous motion-compensation approach does not need any change in HIFU transducer position as it can freely steer the beam in all directions.

To estimate the total treatment time, we assume that it takes one breathing cycle to change the HIFU device position along the mechanical axes. The total treatment time for the continuous motion-compensation approach consist only of the beam time. The results can be seen in figure 2(c). *WL* has a shorter treatment time than *OT*. However, *LinProg* achieves the shortest treatment time. The total treatment time of *ContMotion* is in between of *OT* and *WL*.

In figure 2(d), we see the relative treatment time compared to the *ContMotion* approach. The relative duration shows how the different methods perform compared to the *ContMotion* solution for different focal spot sizes. We can observe that the relative treatment duration of *OT* is increasing over the different focal spot sizes, whereas the relative treatment time of *LinProg* and *WL* stays almost constant. *WL* has a relative treatment time around 0.8, *LinProg* achieves values of about 0.59–0.64. *OT* has a treatment time of 1.2–1.5 times the sonication time of *ContMotion*.

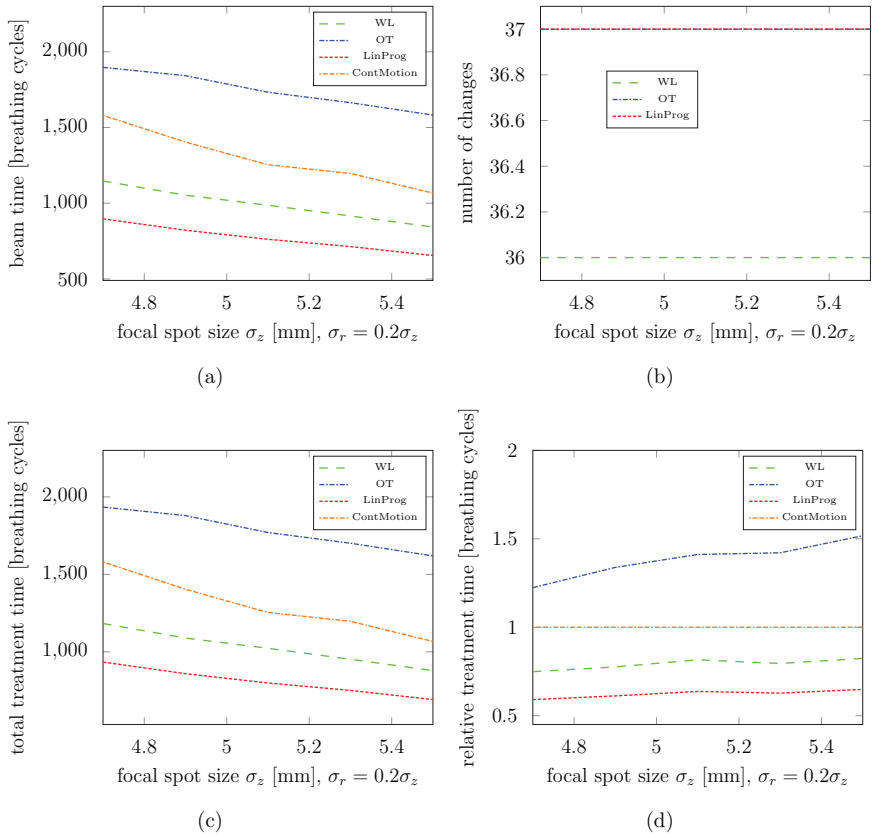

Figure 2. Effect of focal spot size on treatment time. (a) Beam time in breathing cycles calculated by equation (10), (b) number of changes calculated by equation (11) with $c = 1$, (c) total treatment time assuming that one change of the HIFU device takes one breathing cycle, (d) relative treatment time compared to the continuous motion-compensation method (*ContMotion*).

3.4. Efficiency

In figure 3, we see how the efficiency coefficient given by equation (12) evolves with increasing focal spot size. We can see that the efficiency is almost constant for the different focal spot sizes. The efficiency is the highest for the *ContMotion* approach. Since *ContMotion* follows the liver motion, overtreatment can be reduced. However, also with this approach not all overtreatment can be avoided. The reason is that when ablating the border points of the target, also some healthy tissue will be heated. *OT* performs better than *WL*, and the *LinProg* approach has the highest efficiency coefficient of our proposed methods.

3.5. Overtreatment

The distribution of the two different kinds of overtreatment is shown in figure 4. The difference between the two methods *WL* and *OT* is the distribution of the overtreatment. *WL*

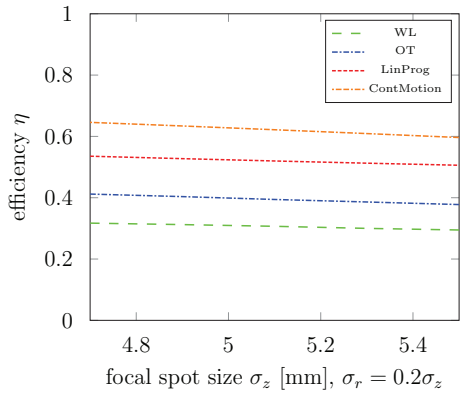

Figure 3. Efficiency coefficient for the different methods calculated by equation (12). The efficiency of the optimal solution is 1.

induces a higher temperature rise inside the target and treats healthy tissue less. The reason for this behavior are the different strategies. The prior target of *OT* is to avoid temperature rises above α inside the target. The treatment of healthy tissue is not minimized. Due to the bigger focal spot of the HIFU device with increasing σ_z and σ_r, more healthy tissue is affected when focusing a point at the target border. This results in an increasing treatment outside the target. *LinProg* combines the advantages of the two. The treatment of tissue outside the target is almost the same as with *WL*, and at the same time the overtreatment inside the target is below the level of *OT*. However, *ContMotion* achieves the least overtreatment inside and outside the target.

3.6. Temperature rise of target points

The dose volume plots for a focal spot size of $\sigma_z = 5\,\text{mm}$ and $\sigma_r = 1\,\text{mm}$ can be seen in figure 5. An ideal dose volume plot would have a maximal and minimal temperature rise of 18 °C inside the whole target. We see that *OT* and *LinProg* achieve similar dose volume plots. WL induces a temperature rise of above 60 °C, which can cause boiling. However, the *ContMotion* approach induces the smallest temperature rise inside the target while ablating the whole target. This result corresponds to figure 4(b), where the overtreatment inside the target is shown.

3.7. Sagittal and axial slices through the liver

To observe the temperature profile after the HIFU treatment, sagittal and axial slices of the different methods are shown in figures 6 and 7, respectively. In these plots, filled circles represent target points, whereas unfilled circles are healthy tissue. The focal spot deviations are $\sigma_z = 5\,\text{mm}$ and $\sigma_r = 1\,\text{mm}$. In the sagittal slices, we can see that the methods heat up points that lay above the target. This is due to the main motion direction, which is along the z-axis. Note that there is also motion in the xy-plane due to the non-rigid motion, however the main motion is along the z-axis. The *LinProg* approach induces a lower temperature rise into the points above the target as compared to *OT*. As a results, less volume will be ablated above the target with the *LinProg* approach. *WL* on the other hand induces the highest temperature rise inside the target, this can be seen in figure 8. However, less healthy tissue points are ablated as compared to *OT*,

Phys. Med. Biol. **61** (2016) 4247 N Möri *et al*

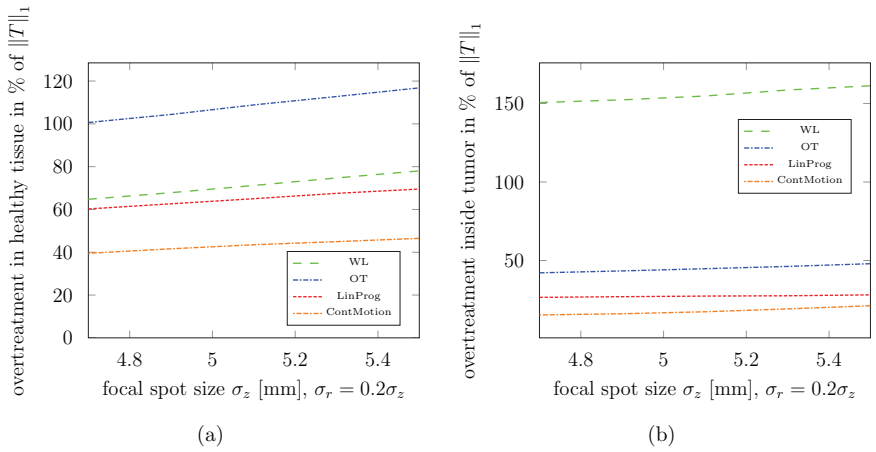

Figure 4. Distribution of the overtreatment for different focal spot sizes. (a) Accumulated temperature rises in healthy tissue relative to the optimal accumulated temperature rises inside the target, which is $\|T\|_1$, (b) overtreatment inside the target, in percent of $\|T\|_1$.

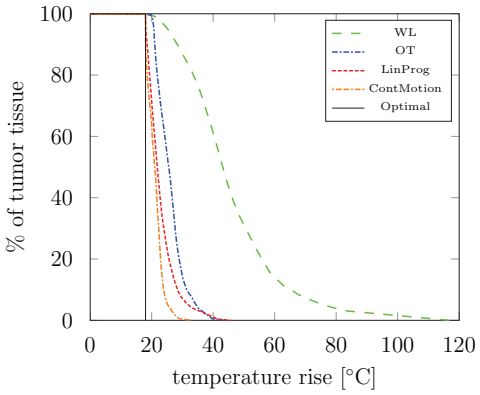

Figure 5. Dose volume plots of the different methods. The focal spot deviations are $\sigma_z = 5$ mm and $\sigma_r = 1$ mm. The abscissa indicates the induced temperature rise, where 18 °C yields tissue ablation. The ordinate represents the percentage of the target tissue. We see that all the methods induce the lethal temperature rise to 100% of the target tissue. The optimal solution induces to 100% of the target tissue the lethal temperature rise of 18 °C, and to 0% a temperature rise above 18 °C.

which can be seen in table 2. The *ContMotion* approach has the least treatment outside the target, due to the motion-compensation. However, at the right and left hand side of the target more healthy points are treated than below and above the target. This is due to the focal spot shape: more overtreatment occurs along the acoustic axis.

In the axial slices, the heat distribution inside the target can be seen. The *ContMotion* approach achieves a temperature rise of 18–25 °C inside the target, except for two hotspots, where the temperature is about 35 °C. *WL* induces the highest temperature rise inside the tumor,

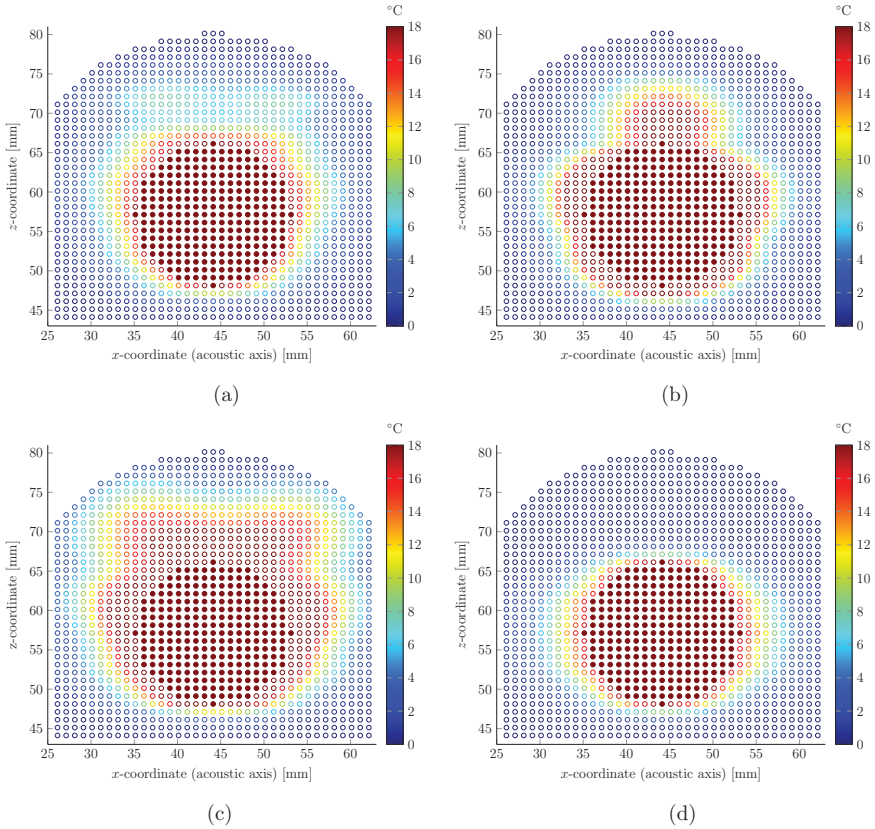

Figure 6. Sagittal slices through the liver, 12 mm away from the target center. The filled circles represent target tissue, unfilled circles represent surrounding tissue. The circle color indicates the induced temperature rise after the HIFU treatment. The focal spot deviations are $\sigma_z = 5$ mm and $\sigma_r = 1$ mm. The acoustic axis of the HIFU device is along the x-axis, and the main breathing motion is along the z-axis. (a) LinProg. (b) WL. (c) OT. (d) ContMotion.

and produces two hot spots with a temperature rise of above 60 °C, which can be seen in figure 8. This is problematic, since these temperature rises can cause boiling. *OT* and *LinProg* induce a higher temperature rise at the tumor bottom compared to the remainder of the target.

If we look at table 2, we can see how much healthy tissue is ablated in percentage of the target volume. We observe that with the *ContMotion* approach, healthy tissue of the size of 0.1% of the target volume is ablated. In our proposed methods, more healthy tissue is heated above 18 °C. However, treatment of tissue outside the target can be reduced by turning off the beam when the focal spot position is outside the target.

3.8. Minimizing with M^f

If minimizing equation (6) with covermatrix M^f as defined in equation (8), treatment of tissue outside the target with *OT* can be reduced. The results can be seen in figure 9. To find

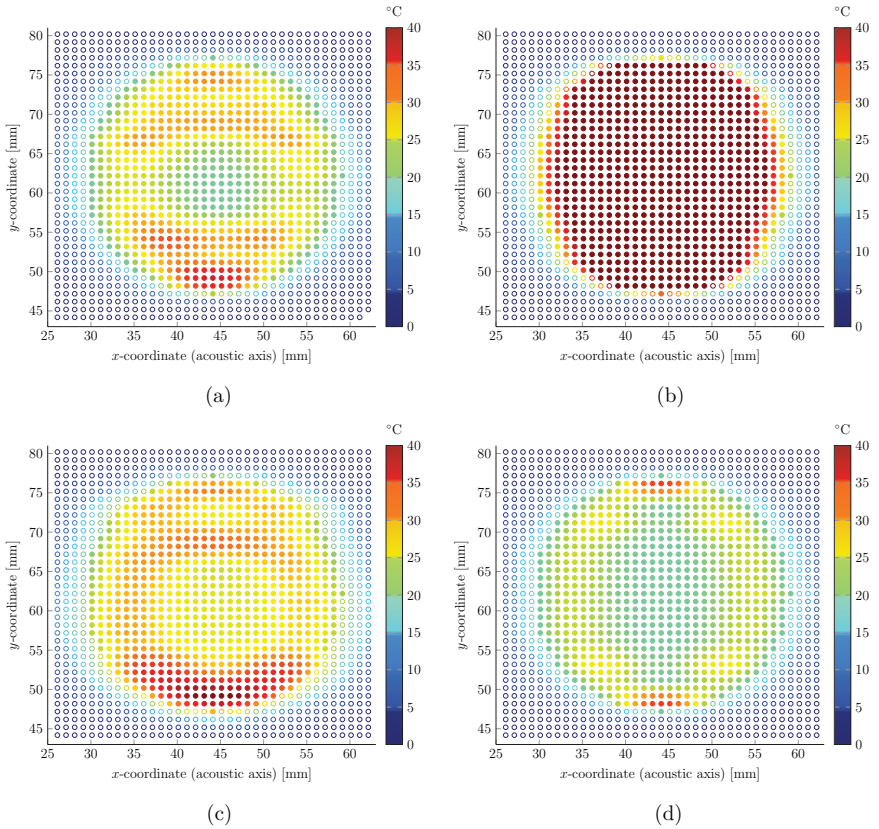

Figure 7. Axial slices through the liver at the target center. The filled circles represent target tissue, unfilled circles represent surrounding tissue. The circle color indicates the induced temperature rise after the HIFU treatment. The focal spot deviations are $\sigma_z = 5$ mm and $\sigma_r = 1$ mm. The acoustic axis of the HIFU device is along the x-axis, and the main breathing motion is along the z-axis. (a) *LinProg*. (b) *WL*. (c) *OT*, (d) *ContMotion*.

appropriate values of R in the definition of S_j, we found out that $R = 3$ mm gives the best results for the focal spot size of $\sigma_z = 5$ mm, $\sigma_r = 1$ mm. When choosing $R = 0$ mm, which means that the beam is immediately turned off when focusing healthy tissue, the method does not improve. Ablation outside and inside the tumor increases (see table 2 and figure 9(e)). The problem when choosing $R = 0$ mm is that border points of the target have to be heated from points that are inside the target. As a result, these points are heated more. In other words, the energy can not be equally distributed, which results in high temperature rises outside as well as inside the target. However, when choosing $R = 3$ mm, i.e. allowing the focal beam to heat healthy tissue with a distance of at most 3 mm from the target, better results can be achieved. The energy can be distributed more evenly, which results in lower temperature rises. Hence, ablation of tissue outside the tumor can be reduced (table 2), while the dose volume plot stays almost the same as with *OT* (figure 9(e)). However, ablation of healthy tissue is still higher compared to the other methods.

Table 2. Efficiency η and the volume of ablated healthy tissue in percentage of the target volume.

Method	$\geqslant +18$ °C (%)	η
WL	17.9	0.31
OT	25.9	0.4
LinProg	1.6	0.52
ContMotion	0.1	0.63
WL using M^{s} and $T = 10$	0.6	0.54
OT using M^{f} and $R = 0$ mm	42.4	0.25
OT using M^{f} and $R = 3$ mm	21.5	0.44

Note: The target is a sphere with a radius of 15 mm and the focal spot size is $\sigma_z = 5$ mm, $\sigma_r = 1$ mm.

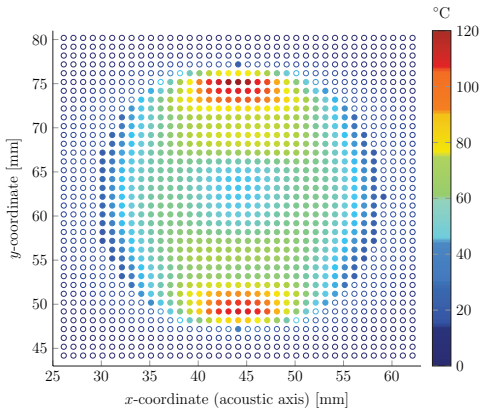

Figure 8. Axial slice through the liver at the target center of the *WL* method for better visualization of the temperature rise. The filled circles represent target tissue, unfilled circles represent surrounding tissue. The circle color indicates the induced temperature rise after the HIFU treatment. The focal spot deviations are $\sigma_z = 5$ mm and $\sigma_r = 1$ mm. The acoustic axis of the HIFU device is along the x-axis, and the main breathing motion is along the z-axis.

3.9. Minimizing with M^{s}

The dose volume plot of *WL* can be further improved by the minimization problem stated in equation (9). We divided the breathing cycle into $T = 10$ different time steps. In figure 10(c), it can be seen that the dose volume plot of *WL* can be improved, the maximal temperature rise inside the target is much less compared to *WL*. However, it is still higher than with the *OT* and *LinProg* approach. The ablated healthy tissue is much less compared to *WL*, which can be seen in table 2. However, the computational effort is larger with this method than computing *WL*. Further, the treatment time is elongated with this method: the duration is about 1.7 times longer than with *WL*. This is due to the higher intensities used in the treatment plan.

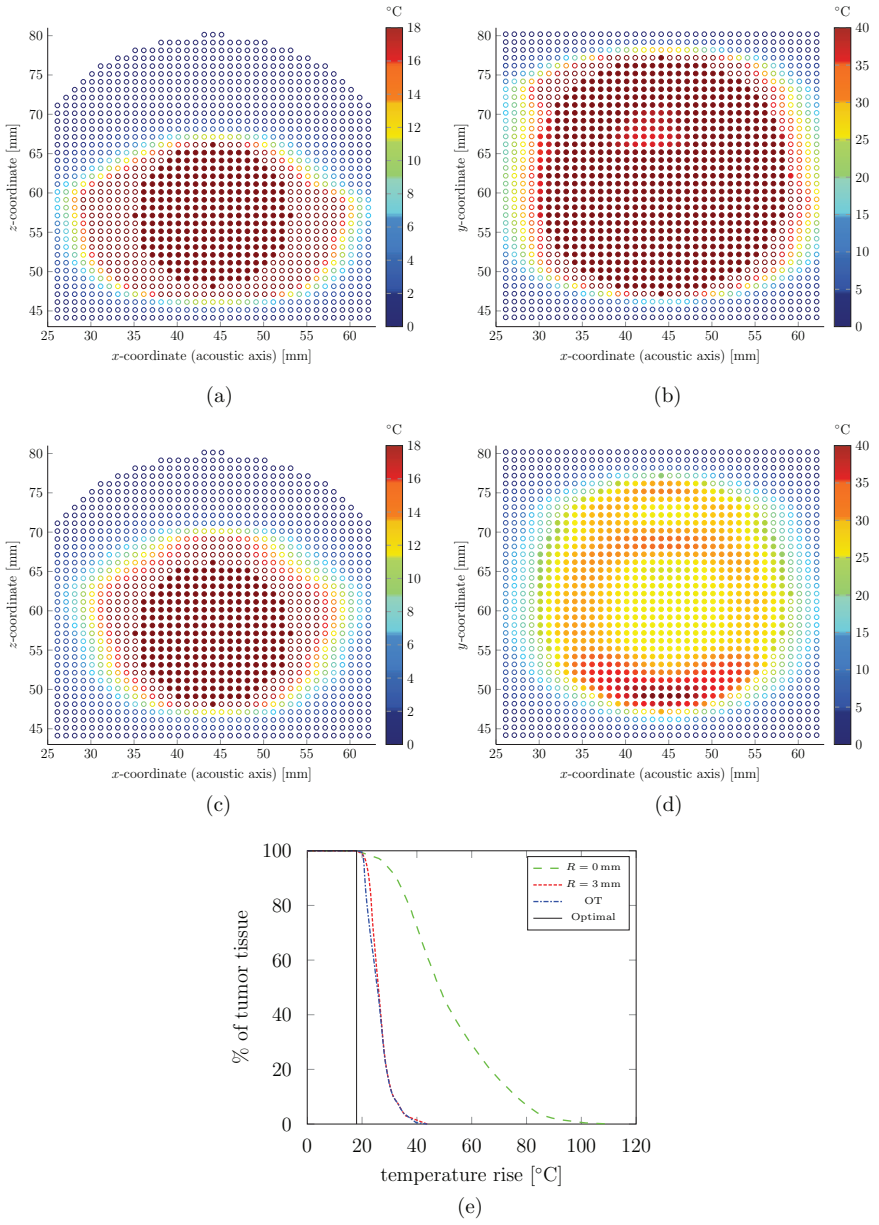

Figure 9. The sagittal and axial slices of the treatment plans from minimization problem with matrix M^{f} defined in equation (8), with $\sigma_z = 5\,\mathrm{mm}$, $\sigma_r = 1\,\mathrm{mm}$, (a) sagittal slice with $R = 0\,\mathrm{mm}$, (b) axial slice with $R = 0\,\mathrm{mm}$, (c) sagittal slice with $R = 3\,\mathrm{mm}$, (d) axial slice with $R = 3\,\mathrm{mm}$, (e) dose volume plots.

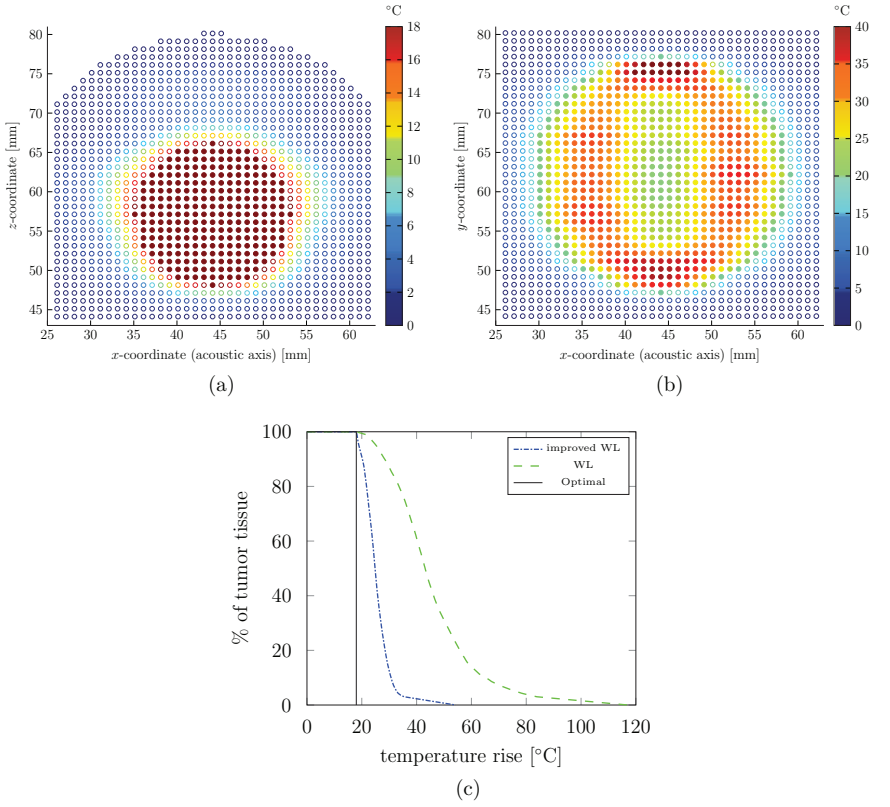

Figure 10. The sagittal (a), axial (b) slices and the dose volume plot (c) of *WL* after adjusting the intensities by minimization problem (9).

4. Discussion

We conclude that *LinProg* combines the advantages of *WL* and *OT*. It minimizes overtreatment inside the target, while avoiding damage on healthy tissue. However, in practice the sonication plan has to be adjusted during treatment. The breathing pattern of the patient can change during treatment which results in a different liver motion. To account for this, the treatment plans have to be adapted regularly. Additionally, the thermo-acoustic parameters of the tissue can not be predicted with a high accuracy (Zhang *et al* 2009). This requires a fast computation of the treatment plan. The treatment plans computed with the compressed sensing approach (*OT* & *WL*) can be calculated in linear time, whereas *LinProg* has a complexity of $\mathcal{O}(m^{3.5})$. However, currently no real-time computation is possible. The presented methods are calculated before the treatment. It will be subject of future work to improve the algorithms towards on-line computation of the treatment plans. As soon as our treatment planning method can be computed in real-time, we will be able to consider non-repetitive breathing patterns of the patient. The goal is then to use a pre-calculated sonication plan. As soon as we observe a change in the motion pattern, the sonication plan will be adapted to the new conditions. However, at the moment this is not yet possible and is subject of future work.

The disadvantage of *WL* is the high temperature rise inside the target which can cause tissue boiling. This problem can be solved by choosing the covermatrix $\boldsymbol{M}^{\mathrm{s}}$ and the minimization problem as stated in equation (9). However, the complexity of this problem is higher than the compressed sensing approach. The disadvantage of *OT* on the other hand is treatment outside the target. By changing the covermatrix $\boldsymbol{M}$ to $\boldsymbol{M}^{\mathrm{f}}$ in the compressed sensing formulation, treatment outside the target can be reduced, while preserving linear complexity. The dose volume plots on the other hand stay almost the same.

When comparing our method to *ContMotion*, we observe that the efficiency is decreased. However, we can achieve shorter treatment plans with the self-scanning approach using the *LinProg* method.

The idea of self-scanning shows potential to be adapted in other tumor treatment modalities such as proton therapy or classical radiation therapy. The difference between the models is the dose accumulation. Therefore, in our proposed model the covermatrix $\boldsymbol{M}$ has to be adjusted to the particular therapy.

In our simulation, we did not consider diffusion over time and therefore our results are an approximation of the reality. But since the motion-compensation approach was simulated with the same model, we are able to compare the methods under the same conditions. The main thing that will change when including diffusion over time is that after a certain amount of time, the already heated tissue will cool down. As a result, these points have to be heated again, which increases the treatment time. At the border of the target, this effect helps to avoid ablation of healthy tissue. Inside the target on the other side it is probable that the treatment time increases. However, when sonicating the points in an optimal order, especially when sonicating neighboring points, the increase of treatment time can be reduced. Moreover, since in the presented results both the self-scanning as well as the continuous motion-compensating approach were simulated without diffusion, we expect a comparable change in the treatment time. However, it remains to be shown that the self-scanning approach has a shorter treatment time under real conditions.

Another simplification in our model is the assumption that tissue which is heated above 54 °C undergoes necrosis. A more accurate measure on the thermal impact of tissue is the thermal dose equation. According to the thermal dose equation, it might not be enough in some cases to heat tissue above a temperature of 54 °C. However, if tissue is heated for enough time to 54 °C, by the thermal dose equation, necrosis can be induced. Including the thermal dose model in a further study may thus change our estimated treatment time and it remains to be shown that the impact on the self-scanning and the continuous motion-compensating approach is in the same range.

Moreover, there are other limitations, such as the reduced ultrasound window due to ribs and skin heating (Hynynen 2010, Wijlemans *et al* 2012, Ellis *et al* 2013). It has to be shown in further studies, how these problems can be solved in detail when using the proposed self-scanning approach. However, the self-scanning approach simplifies beam forming, as compared to the continuous motion compensating approach, we do no longer have to deal with the often contradicting goals of compensation of the motion and avoiding near field heating while at the same time covering the sonication volume.

5. Conclusion

In this paper, we proposed a novel self-scanning approach for HIFU in liver and showed its feasibility by simulation. We indicated an algorithm to calculate a treatment plan for such a setup. Our method achieved a shorter treatment time than the motion-compensation approach.

However, we simulated our method on a simplified model. It remains to be shown in further studies how the self-scanning method performs under a more realistic model. Moreover, the energy distribution efficiency is reduced. Despite the decreased efficiency, the expected shorter treatment time and the reduced complexity on the beam forming possible with the proposed self-scanning method render the idea of self-scanning attractive.

References

Arnold P, Preiswerk F, Fasel B, Salomir R, Scheffler K and Cattin P C 2011 3D organ motion prediction for MR-guided high intensity focused ultrasound *Medical Image Computing and Computer-Assisted Intervention—MICCAI 2011* (New York: Springer) pp 623–30

Auboiroux V, Dumont E, Petrusca L, Viallon M and Salomir R 2011 An mr-compliant phased-array HIFU transducer with augmented steering range, dedicated to abdominal thermotherapy *Phys. Med. Biol.* **56** 3563

Auboiroux V, Petrusca L, Viallon M, Muller A, Terraz S, Breguet R, Montet X, Becker C D and Salomir R 2014 Respiratory-gated MRGHIFU in upper abdomen using an MR-compatible in-bore digital camera *BioMed Res. Int.* **2014** 1–9

Birgin E G, Martinez J M and Raydan M 2014 Spectral projected gradient methods: review and perspectives *J. Stat. Softw.* **60** 1–21

Celicanin Z, Auboiroux V, Bieri O, Petrusca L, Santini F, Viallon M, Scheffler K and Salomir R 2014 Real-time method for motion-compensated MR thermometry and MRGHIFU treatment in abdominal organs *Magn. Reson. Med.* **72** 1087–95

Cline H E, Hynynen K, Hardy C J, Watkins R D, Schenck J F and Jolesz F A 1994 MR temperature mapping of focused ultrasound surgery *Magn. Reson. Med.* **31** 628–36

Cline H E, Schenck J F, Hynynen K, Watkins R D, Souza S P and Jolesz F A 1992 MR-guided focused ultrasound surgery *J. Comput. Assist. Tomogr.* **16** 956–65

De Senneville B D, Ries M, Bartels L W and Moonen C T 2012 MRI-guided high-intensity focused ultrasound sonication of liver and kidney *Interventional Magnetic Resonance Imaging* (New York: Springer) pp 349–66

Ellis S, Rieke V, Kohi M and Westphalen A C 2013 Clinical applications for magnetic resonance guided high intensity focused ultrasound (MRGHIFU): present and future *J. Med. Imaging Radiat. Oncol.* **57** 391–9

Holbrook A B, Ghanouni P, Santos J M, Dumoulin C, Medan Y and Pauly K B 2014 Respiration based steering for high intensity focused ultrasound liver ablation *Magn. Reson. Med.* **71** 797–806

Hui L, Guofeng S and Yazhu C 2009 Treatment planning of scanning time and path for phased high-intensity focused ultrasound surgery *IEEE 2nd Int. Conf. on Biomedical Engineering and Informatics* pp 1–4

Hynynen K 2010 MRI-guided focused ultrasound treatments *Ultrasonics* **50** 221–9

Kennedy J E 2005 High-intensity focused ultrasound in the treatment of solid tumours *Nat. Rev. Cancer* **5** 321–7

Köhler M O, Mougenot C, Quesson B, Enholm J, Le Bail B, Laurent C, Moonen C T and Ehnholm G J 2009 Volumetric HIFU ablation under 3D guidance of rapid MRI thermometry *Med. Phys.* **36** 3521–35

Mansour H 2012 Beyond ℓ1-norm minimization for sparse signal recovery *Statistical Signal Processing Workshop* pp 337–40

Mougenot C, Salomir R, Palussière J, Grenier N and Moonen C T 2004 Automatic spatial and temporal temperature control for MR-guided focused ultrasound using fast 3d mr thermometry and multispiral trajectory of the focal point *Magn. Reson. Med.* **52** 1005–15

Natarajan B K 1995 Sparse approximate solutions to linear systems *SIAM J. Comput.* **24** 227–34

Petrusca L *et al* 2013 Hybrid ultrasound/magnetic resonance simultaneous acquisition and image fusion for motion monitoring in the upper abdomen *Investigative Radiol.* **48** 333–40

Petrusca L, Viallon M, Terraz S, de Luca V, Celicanin Z, Auboiroux V, Brunke S, Cattin P and Salomir R 2011 Simultaneous ultrasound imaging and MRI acquisition *Interventional Magnetic Resonance Imaging* (Berlin: Springer) pp 457–70

Preiswerk J C F and Cattin P C 2015 Respiratory motion compensation with topology independent surrogates *ICART: Imaging and Computer Assistance in Radiation Therapy MICCAI workshop* pp 97–104

Preiswerk F, De Luca V, Arnold P, Celicanin Z, Petrusca L, Tanner C, Bieri O, Salomir R and Cattin P C 2014 Model-guided respiratory organ motion prediction of the liver from 2D ultrasound *Med. Image Anal.* **18** 740–51

Ries M, De Senneville B D, Roujol S, Berber Y, Quesson B and Moonen C 2010 Real-time 3D target tracking in MRI guided focused ultrasound ablations in moving tissues *Magn. Reson. Med.* **64** 1704–12

Robere R 2012 Interior point methods and linear programming University of Toronto

Rosenberg C, Kickhefel A, Mensel B, Pickartz T, Puls R, Roland J and Hosten N 2013 PRFS-based MR thermometry versus an alternative T1 magnitude method–comparative performance predicting thermally induced necrosis in hepatic tumor ablation *PloS One* **8** e78559

Salomir R, Palussière J, Vimeux F C, de Zwart J A, Quesson B, Gauchet M, Lelong P, Pergrale J, Grenier N and Moonen C T 2000 Local hyperthermia with MR-guided focused ultrasound: spiral trajectory of the focal point optimized for temperature uniformity in the target region *J. Magn. Reson. Imaging* **12** 571–83

Sapareto S A and Dewey W C 1984 Thermal dose determination in cancer therapy *Int. J. Radiat. Oncol. Biol. Phys.* **10** 787–800

Schwenke M *et al* 2015 An integrated model-based software for FUS in moving abdominal organs *Int. J.Hyperthermia* **31** 240–50

ter Haar G, Sinnett D and Rivens I 1989 High intensity focused ultrasound—a surgical technique for the treatment of discrete liver tumours *Phys. Med. Biol.* **34** 1743

Trofimov A, Rietzel E, Lu H M, Martin B, Jiang S, Chen G T Y and Bortfeld T 2005 Temporo-spatial IMRT optimization: concepts, implementation and initial results *Phys. Med. Biol.* **50** 2779–98

Von Siebenthal M, Székely G, Gamper U, Boesiger P, Lomax A and Cattin P 2007 4D MR imaging of respiratory organ motion and its variability *Phys. Med. Biol.* **52** 1547

Wijlemans J, Bartels L, Deckers R, Ries M, Mali W T M, Moonen C and van den Bosch M 2012 Magnetic resonance-guided high-intensity focused ultrasound (MR-HIFU) ablation of liver tumours *Cancer Imaging* **12** 387

Wissler E H 1998 Pennes 1948 paper revisited *J. Appl. Physiol.* **85** 35–41

Zhang S, Wan M, Zhong H, Xu C, Liao Z, Liu H and Wang S 2009 Dynamic changes of integrated backscatter, attenuation coefficient and bubble activities during high-intensity focused ultrasound (HIFU) treatment *Ultrasound Med. Biol.* **35** 1828–44

Zhou Y 2013 Generation of uniform lesions in high intensity focused ultrasound ablation *Ultrasonics* **53** 495–505

6 An Optimal Control Approach

The method of this chapter's publication is based on a more realistic setup. The temperature model used is based on an analytical solution of the Pennes bioheat equation assuming a Gaussian shaped heat source and temperature rise, from which the thermal dose is calculated. The optimization problem to obtain treatment plans is based on an optimal control approach, which is solved using an interior-point algorithm. The treatment plan is found for the whole treatment at once. The treatment time and overtreatment obtained with the self-scanning approach is compared to the tracking approach. We show that the treatment time as well as the amount of overtreatment of both methods are in the same range. The temperature model is verified with ex-vivo experiments, showing a good agreement to the measured MR-thermometry data.

An appendix concludes this chapter, giving more details about the method by showing some additional theoretical results of the proposed method.

Publication. The following paper was presented as Poster in Quebec, September 2017, at the *20th International Conference on Medical Image Computing and Computer Assisted Intervention (MICCAI)* and was published as part of the conference proceedings.

An Optimal Control Approach for High Intensity Focused Ultrasound Self-Scanning Treatment Planning

Nadia Möri[1( )], Laura Gui[2], Christoph Jud[1], Orane Lorton[2], Rares Salomir[1], and Philippe C. Cattin[1]

[1] Department of Biomedical Engineering, University of Basel, Basel, Switzerland
nadia.moeri@unibas.ch
[2] Faculty of Medicine, Radiology, University of Geneva, Geneva, Switzerland

Abstract. In noninvasive abdominal tumor treatment, research has focused on canceling organ motion either by gating, breath holding or tracking of the target. This paper is based on the novel self-scanning method which combines the advantages of the gated and the tracking method. This approach leverages the respiratory organ motion by holding the focal spot of the high intensity focused ultrasound (HIFU) device static for a given time, while it passively scans the tumor due to respiratory motion. This enables to use a lower-cost HIFU device. We present a planning method for such a system that is based on optimal control theory which optimizes the scanning path and the sonication intensities simultaneously. The method minimizes treatment time and ensures complete tumor ablation according to the thermal dose under free-breathing. To verify our method, we simulated a tumor in two dimensions. The achieved treatment time performs on par to the gold-standard tracking method. Moreover, we measured the temperature profile of the HIFU device in a tissue-mimicking phantom to verify our temperature model.

Keywords: Self-scanning · Treatment planning · HIFU

1 Introduction

High intensity focused ultrasound (HIFU) is a well-known non-invasive thermal ablation modality for tumor treatment which is widely accepted for decades [3,4]. For image guidance during HIFU sonication, magnetic resonance imaging (MRI) is often used, which not only provides images of the tumor, but is also used for temperature mapping [5,11]. The challenge arising in HIFU treatment of abdominal organs, such as kidney and liver, is respiratory motion and organ drift [13]. So far, research has focused on minimizing organ motion either by gating, breath holding or tracking of the target. However, the disadvantage of gating is the prolonged treatment time, and for tracking, the beam of the HIFU device has to be steered, which causes an intensity decay at the focal spot [2].

© Springer International Publishing AG 2017
M. Descoteaux et al. (Eds.): MICCAI 2017, Part II, LNCS 10434, pp. 532–539, 2017.
DOI: 10.1007/978-3-319-66185-8_60

In this paper, we use a novel method which takes advantage of the perpetual respiratory motion to passively scan the tumor. In other words, we are placing the static focal point of the HIFU into the tumor [8]. The motion caused by breathing shifts the tumor through this focal point. For tracking of the tumor, a respiratory motion model can be used, for example the one described in [6]. With the motion model we anticipate at which time point tumor tissue is located under the focal spot and thus modulate the HIFU intensity based on this information. Once the tumor has been ablated along the self-scanned trajectory, the focal spot is relocated to a different but static position within the body. With the proposed method, we combine the advantages of the gated and the tracking method: a lower-priced HIFU device can be used and a high duty cycle is achieved. Moreover, the complexity of the beam forming is reduced by not steering the focal spot. However, this comes at the cost of an increased complexity of the planning stage.

We present an optimal control approach to determine optimal sonication plans for such a system ensuring complete tumor ablation. Optimal control approaches have been used before to find treatment plans using HIFU in static tissue [1,7,14]. However, in these approaches the target is still and not moving as in our case. The novelty of our method compared to the self-scanning approach in [8] is that we modeled a realistic temperature elevation and included the thermal dose, whereas they used a simplified temperature and dose model. Our approach optimizes the scanning path and the sonication intensities simultaneously. In a first step an optimal scanning path is found. In a second step, we optimize the thermal dose by adjusting the intensities. We simulated a 2D tumor and showed the feasibility of our method. Moreover, we experimentally evaluated our temperature model by sonicating a tissue-mimicking phantom with a HIFU device and measuring the temperature with MR-Thermometry. We found good correspondence between our model and the measured data.

2 Method

The task of planning a treatment is to find appropriate tumor points which are sonicated by the HIFU device. The focal spot will stay static for a given time to achieve a precalculated temperature rise. During this phase, different tissue will pass through the focal spot due to respiratory motion. The points and the corresponding intensities have to be chosen such that the whole target is ablated. To avoid overtreatment, the energy has to be distributed mainly on the target and healthy tissue should be treated the least possible. Under these conditions, the treatment time is minimized, which consists of beam- and changing time. The beam time is the overall time where the HIFU device is focused on one point. The HIFU system used for the self-scanning approach is able to electrically steer the focal spot rapidly in depth along the acoustic axis. For the other directions, slower mechanical displacement is used, called changing time.

Temperature Model. The temperature inside the body is described by Pennes bioheat equation [10], for which a closed-form solution can be derived [14]. To calculate the temperature induced by a moving heat source, we discretized over time and write it as sum of static heat sources. For a temperature with moving heat source, we can write the temperature rise at point p and time t as

$$T(p,t) = \sum_i T_{\text{off}}(\gamma(p), i\Delta t, I_i), \tag{1}$$

where T_{off} is a closed-form solution for a static heat source similar to [14], γ is the respiratory motion function, I_i denotes the intensity at the time interval i, and each time interval has a duration of Δt seconds.

Thermal Dose. The most accepted model to determine how tissue is affected by temperature is described by the thermal dose model [12], which estimates the cumulative equivalent minutes at a temperature of 43°C (CEM_{43}).

Optimal Control. Our aim is to find an optimal treatment plan u that minimizes the treatment time and overtreatment while ensuring that the whole target is ablated. A treatment plan $u = (u^{\text{p}}(t), u^{\text{I}}(t))$ consists of points that are sonicated $u^{\text{p}}(t)$ (one per breathing cycle) and sonication intensities $u^{\text{I}}(t)$ (m per breathing cycle) for each time point $t \in [0, t_{\text{e}}]$, were $[0, t_{\text{e}}]$ is the treatment time interval. The treatment plan u induces a temperature rise T_u inside the domain, which is calculated by Eq. (1). As we want to prevent tissue from boiling, we claim that a given maximal temperature rise can not be exceeded. From the temperature rise T_u, the thermal dose D_u can be derived to obtain how the tissue is affected [12]. A treatment plan u is admissible, denoted by $u \in U_{\text{ad}}$, if the induced temperature rise T_u does not exceed a given maximal allowed temperature rise. Further, the target has to be ablated, which means that the thermal dose D_u inside the target has to reach to the lethal thermal dose. If T_u and D_u satisfy the mentioned constraints, we say that T_u and D_u are feasible. Moreover, the sonication points $u^{\text{p}}(t)$ have to be inside the domain Ω and the sonication intensities $u^{\text{I}}(t)$ can not exceed the maximal intensity $I_{\max}$.

$$U_{\text{ad}} = \{u = (u^{\text{p}}(t), u^{\text{I}}(t)) \,|\, u^{\text{p}}(t) \in \Omega,\, u^{\text{I}}(t) \in [0, I_{\max}], T_u \text{ and } D_u \text{ feasible}\}.$$

To get the optimal treatment plan, we find u^* which satisfies

$$u^* = \arg\min_{u \in U_{\text{ad}}} G(u) + \|w(D_u - D_{\text{opt}})\|, \tag{2}$$

where G is a functional that measures the treatment time, D_{opt} denotes the desired optimal thermal dose distribution and w is a weighting function that gives less weight to the target border. Note that the target can have any shape and a target zone around the tumor can be defined by adaption of D_{opt}. As it is difficult to not treat the healthy tissue at the border of the target, the weighting

ensures that this sort of overtreatment is less penalized. We define the treatment time measurement function G as

$$G(u) = \underbrace{\sum_i t_i(1 - \delta_0(u^{\mathrm{I}}(t_i)))}_{\star} + \underbrace{\eta \sum_i t_i \max(\nabla u^{\mathrm{I}}(t_i), 0)}_{\bullet},$$

where $\delta_0(x)$ is the Dirac delta at 0 and η is a weighting parameter to ensure that both sums are penalizing equally. The first sum ($\star$) penalizes nonzero intensities, i.e. times where the HIFU beam is on, where the multiplication with time t_i ensures that the longer the sonication, the more it costs. The second sum ($\bullet$) penalizes breaks of the sonication by preventing to turn the beam on again after it was turned off. This ensures that the beam is only turned off at the end of the treatment.

As the problem described in (2) is nonconvex and ill-posed, a good initial value for u is important for the success of the optimization process. To get such an initial value, we first solve the following optimal control problem.

$$u_{\mathrm{start}} = \arg\min_{u \in U_{\mathrm{ad}}} G(u) + \left\| w \left(\max_t T_u - T_{\mathrm{opt}} \right) \right\| + f(u), \;\; \text{s.t. } T_{\mathrm{opt}} \leq \max_t T_u,$$

where the function f is defined as $f(u) = \sum_i \|(P_{\mathrm{ac}}(u^{\mathrm{p}}(t_{i+1}) - u^{\mathrm{p}}(t_i)))\|$, and penalizes the changing time. Here, P_{ac} the orthogonal projection along the acoustic axis and T_{opt} is the optimal temperature to be reached. With the constraint we impose that inside the target a minimal temperature has to be attained during the treatment. Note that if one chooses an appropriate optimal temperature T_{opt}, one can predict with a high certainty that the target tissue will be ablated.

Now, we hold the sonication path defined by $u^{\mathrm{p}}_{\mathrm{start}}(t)$ fixed, introduce the sonication gaps resulting from changing the position of the HIFU device, and optimize the intensities according to the optimization framework in Eq. (2) to get the optimal treatment plan u^*. Note that after introducing the sonication gaps, u respects the changing time, which means that when two consecutive sonication points are not lying in the acoustic axis, the beam has to be turned off such that the focal spot can be changed by mechanical displacement. Hence, an optimal scanning path is found in the first step and in the second step, the number of variables can be reduced by solely optimizing the intensities.

3 Materials and Results

To show how well our model fits the actual temperature, HIFU experiments were performed on a tissue-mimicking phantom. We used an MRI-compatible 256-element phased-array transducer (Imasonic, Besançon, France), which is operating in the frequency range of 974–1049 kHz with natural focal length $R = 130$ mm and aperture $d = 140$ mm. A bath of degassed water coupled the ultrasound transducer to the phantom. Each sonication was imaged in the coronal and sagittal plane through the focal spot with a resolution of $1 \times 1 \times 3\,\mathrm{mm}^3$.

The imaging was performed on a 3 T clinical MRI-scanner (Prisma Fit, Siemens AG, Healthcare Sector, Erlangen, Germany). A gradient-recalled echo planar imaging (GRE-EPI) sequence was used to provide PRFS-sensitive images. The imaging parameters were: FOV $= 128 \times 128\,\mathrm{mm}^2$, TR $= 21.7\,\mathrm{ms}$, TE $= 10\,\mathrm{ms}$, flip angle $= 8°$, bandwidth $= 550\,\mathrm{Hz}$, EPI factor $= 7$, 11 cm loop coil. The thermal maps were calculated using the time-referenced single baseline 2D PRFS method, corrected for the background phase drift using three unheated ROIs for each time frame [9]. The sonications were performed at a displacement of $0\,\mathrm{mm}, \pm 5\,\mathrm{mm}$ and $\pm 10\,\mathrm{mm}$ in the radial direction during $3\,\mathrm{s}, 5\,\mathrm{s}$ and $10\,\mathrm{s}$.

We fitted the MRI measurements of the temperature with a least square approach. To test the temperature model given by Eq. (1), we discretized over time with $\Delta t = 0.4\,\mathrm{s}$ and wrote the static heat source as sum of heat sources to get T. For Fig. 1, we compared each MR-Thermometry measurement to the prediction of the temperature model T and the closed-form solution to Pennes equation T_{off}. The error was determined by calculating the difference between the model prediction and the measured temperature. We achieved correlation coefficients of 0.86 and 0.82 for T_{off} and T, respectively. The mean errors are $-0.12°\mathrm{C}$ and $-0.48°\mathrm{C}$, the variances $0.87°\mathrm{C}$ and $1.14°\mathrm{C}$, for T_{off} and T respectively. The fitted lines for the correlation plots have a slope of 1.03 and 1.35 for T_{off} and T, respectively. When comparing the MR-Thermometry measurements to our model, we observe that we are slightly underestimating the temperature. This can be seen by the slope of the fitted line to the correlation plot and as the mean error is negative. The error variance is bigger when calculated with T than with T_{off}. The reason is that T_{off} is an approximation to Pennes equation. If T_{off} was precise, the discretization T would converge to T_{off} for $\Delta t \to 0$. However, by the approximation, this property is not exactly fulfilled. In Fig. 2, this effect is visualized. At the focal spot during the heating time, the temperature T converges to T_{off} for $\Delta t \to 0$, which shows that in this case the model is correct. However, during the decay time as well as for points not equal to the focal spot, the discretization model T underestimates the temperature T_{off}.

Now that we have calibrated our physical HIFU system to our optimization framework, we apply the proposed self-scanning idea on a realistic scenario. As

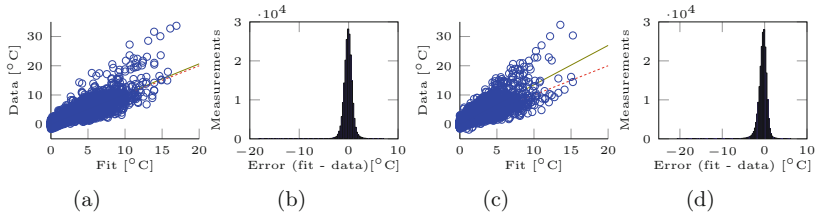

Fig. 1. (a) Correlation and (b) error between T_{off} and the MR-Thermometry data, (c) correlation and (d) error between T and the data. For T, we set $\Delta t = 0.4\,\mathrm{s}$. The solid lines in (a) and (c) are the fitted lines, the dotted are the identity lines.

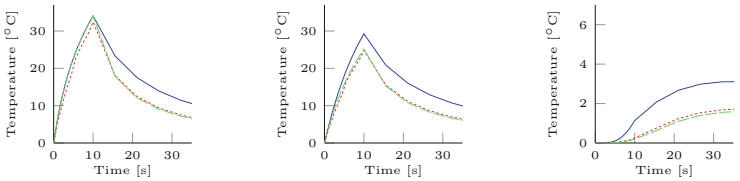

Fig. 2. Comparison of T_{off} and T, where the solid line represents T_{off}, the dashed lines represent T, with red $\Delta t = 0.5\,\text{s}$ and green $0.001\,\text{s}$, (a) temperature rise at the focal spot $(r, z) = (0\,\text{mm}, 0\,\text{mm})$, (b) at position $(r, z) = (1\,\text{mm}, 1\,\text{mm})$, (c) at position $(r, z) = (3\,\text{mm}, 3\,\text{mm})$.

an example, we set the domain $\Omega = 15\,\text{mm} \times 24\,\text{mm}$ to be a two dimensional plane, and the target to a circle with radius $r = 5\,\text{mm}$. The approximate duration of a breathing cycle is around 4 s and the motion in anterior-posterior during one breathing cycle is around 12 mm [13]. Hence, for simplicity, we set the respiratory motion to a sine curve with an amplitude of 6 mm and a period of 4 s. To define the temperature, we used the results of the temperature fit. The focal spot sizes of our HIFU system are $\sigma_r = 1\,\text{mm}$, $\sigma_z = 5\,\text{mm}$, and the diffusivity is $0.0013\,\text{cm}^2$. For the time discretization we use a step of $\Delta t = 0.4\,\text{s}$, and the number of intensity values $u^{\text{I}}(t)$ per breathing cycle was for the first stage $m = 1$, and for the second $m = 10$. Further, the lethal thermal dose was set to $60\,\text{CEM}_{43}$. The minimal temperature rise to reach inside the target during the first step is 20°C, the maximal allowed temperature rise is 50°C. The maximal intensity I_{max} is normalized such that an intensity of $1\,\text{W/mm}^2$ during 10 s induces a temperature rise of 34°C at the focal spot without motion, and we set $I_{\text{max}} = 1\,\text{W/mm}^2$. We

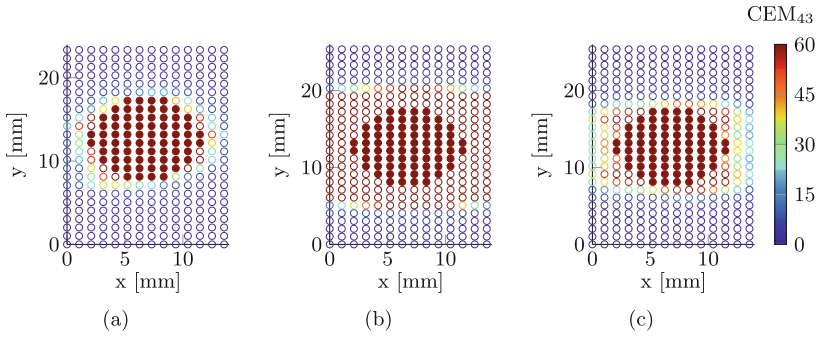

Fig. 3. Thermal dose, the filled dots are target tissue, the acoustic axis is along x-axis and the respiratory motion along y-axis, (a) thermal dose of u^* using the tracking approach, (b) thermal dose of u_{start}, and (c) u^* using the proposed self-scanning approach.

compared the our method to the classical tracking approach, where the focal spot is moved to compensate respiratory motion. We set the intensity decay due to steering to be a Gaussian in radial direction with variance $\sigma = 12\,\text{mm}$.

In Fig. 3, the thermal dose indication for each point in Ω is shown for both stages of the optimization for the self-scanning and the second stage for the tracking approach. In both cases, the whole target is ablated, i.e. the lethal thermal dose of $60\,\text{CEM}_{43}$ is reached inside the whole target. The treatment time found for the self-scanning approach is 268 s, where in this time period 2 changes of the HIFU position have to be made. We set the changing time to last for 4 s, which means that 8 s are used to change the position of the device. The tracking approach on the other hand needs 272 s to ablate the target.

4 Discussion

In the first step of the optimization when solely the temperature is optimized, both the target and also some surrounding tissue is ablated. The reason is that the number of intensities $u^{\text{I}}(t)$ per breathing cycle in the first step is $m = 1$, which means that the intensity can not be changed when the focal spot of the HIFU device is moving outside the target due to respiratory motion. In the second step, $m = 10$, and therefore, the intensity can be turned off when the focal spot is outside the target and overtreatment is successfully reduced. When comparing the results of the self-scanning approach to tracking of the target, we observe that the amount of overtreatment is slightly higher and the treatment times are almost the same. We showed that our optimization framework provides good results in two dimensions with a sine-shaped respiratory motion. Note that the motion can be easily adapted to any kind of motion by adjustment of the motion function γ. However, our method uses still some simplifications, like for example the breathing pattern is not allowed to change during treatment, and can thus not yet be used in clinics. We are currently working on generalizing our method to a more realistic scenario.

When looking at the correlation and the error distribution of the temperature fit, we observe that we are underestimating the temperature rise. However, as we want to guarantee that our treatment plans ablate the whole target, we are on the safe side. The drawback is that there might be more overtreatment of healthy tissue than foreseen and this may cause treatment elongation, as tissue is assumed to heat less than it actually does. However, HIFU treatment devices could be made simpler as only beam steering along the acoustical axis is required.

5 Conclusion

We showed that our optimization framework can be used to calculate feasible treatment plans for a self-scanning HIFU approach in moving tissue. Only few healthy tissue is treated and the treatment time performs on par to the tracking approach. However, the reduced complexity on the beam forming as well as the lower-cost HIFU device renders the idea of self-scanning attractive. In this paper,

we showed on artificial data that our proposed method for calculating optimal treatment plans for a self-scanning HIFU approach in moving tissue works and gives feasible solutions. Further, we showed by HIFU measurements that our temperature model can be fitted to real data. However, it remains to be shown in future studies that our temperature model fits also for moving tissue.

Acknowledgment. This research was supported by the Swiss National Foundation, grant number CR33I3_143980.

References

1. Arora, D., Minor, M.A., Skliar, M., Roemer, R.B.: Control of thermal therapies with moving power deposition field. Phys. Med. Biol. **51**(5), 1201 (2006)
2. Auboiroux, V., Dumont, E., Petrusca, L., Viallon, M., Salomir, R.: An MR-compliant phased-array HIFU transducer with augmented steering range, dedicated to abdominal thermotherapy. Phys. Med. Biol. **56**(12), 3563 (2011)
3. Cline, H.E., Schenck, J.F., Hynynen, K., Watkins, R.D., Souza, S.P., Jolesz, F.A.: MR-guided focused ultrasound surgery. J. Comput. Assist. Tomogr. **16**(6), 956–965 (1992)
4. ter Haar, G., Sinnett, D., Rivens, I.: High intensity focused ultrasound-a surgical technique for the treatment of discrete liver tumours. Phys. Med. Biol. **34**(11), 1743 (1989)
5. Hynynen, K.: MRI-guided focused ultrasound treatments. Ultrasonics **50**(2), 221–229 (2010)
6. Jud, C., Preiswerk, F., Cattin, P.C.: Respiratory motion compensation with topology independent surrogates. In: Workshop on Imaging and Computer Assistance in Radiation Therapy (2015)
7. Malinen, M., Huttunen, T., Kaipio, J.P., Hynynen, K.: Scanning path optimization for ultrasound surgery. Phys. Med. Biol. **50**(15), 3473 (2005)
8. Möri, N., Jud, C., Salomir, R., Cattin, P.: Leveraging respiratory organ motion for non-invasive tumor treatment devices: a feasibility study. Phys. Med. Biol. **61**(11), 4247 (2016)
9. Mougenot, C., Salomir, R., Palussière, J., Grenier, N., Moonen, C.T.: Automatic spatial and temporal temperature control for MR-guided focused ultrasound using fast 3D MR thermometry and multispiral trajectory of the focal point. Magn. Reson. Med. **52**(5), 1005–1015 (2004)
10. Pennes, H.H.: Analysis of tissue and arterial blood temperatures in the resting human forearm. J. Appl. Physiol. **1**(2), 93–122 (1948)
11. Petrusca, L., Cattin, P., De Luca, V., Preiswerk, F., Celicanin, Z., Auboiroux, V., Viallon, M., Arnold, P., Santini, F., Terraz, S., et al.: Hybrid ultrasound/magnetic resonance simultaneous acquisition and image fusion for motion monitoring in the upper abdomen. Invest. Radiol. **48**(5), 333–340 (2013)
12. Sapareto, S.A., Dewey, W.C.: Thermal dose determination in cancer therapy. Int. J. Radiat. Oncol.* Biol.* Phys. **10**(6), 787–800 (1984)
13. Von Siebenthal, M., Székely, G., Gamper, U., Boesiger, P., Lomax, A., Cattin, P.: 4D MR imaging of respiratory organ motion and its variability. Phys. Med. Biol. **52**(6), 1547 (2007)
14. Wan, H., Aarsvold, J., O'Donnell, M., Cain, C.: Thermal dose optimization for ultrasound tissue ablation. IEEE Trans. Ultrason. Ferroelectr. Freq. Control **46**(4), 913–928 (1999)

6.A Extended Theoretical Results

Due to the limited space, we could unfortunately not go into every detail of our proposed optimization method. Some of the parameter choices are explained in the following appendix. As a short repetition, the optimal control method is stated as

$$u^* = \arg\min_{u \in U_{\text{ad}}} G(u) + \|w(D_u - D_{\text{opt}})\|, \tag{6.1}$$

where the treatment time $G(u)$ is defined to be

$$G(u) = \sum_i t_i(1 - \delta_0(u^I(t_i))) + \eta \sum_i t_i \max(\nabla u^I(t_i), 0). \tag{6.2}$$

In this section, we will have a closer look at the choice of the weighting parameter w, the influence of the treatment horizon will be discussed, and the treatment time function G will be analyzed. The results shown in this appendix are obtained by minimizing the same problem as described in the publication and we consider solely the self-scanning approach without comparing to the tracking approach.

Weighting Parameter w. There are different possibilities on how to choose the weighting parameter w. Here, we present three different weights and their influence on the corresponding optimal treatment plan. The three weights are shown in Fig. 6.1(a)–(c). The first weight of Fig. 6.1(a) corresponds to the one used in this chapter's publication. The second weight of Fig. 6.1(b) is constant, corresponding to the case where no weight is used. Finally, the third weight of Fig. 6.1(c) uses a smooth transition region at the boundary of the tumor. For each of the weights, the optimization problem is solved and a feasible solution is found. The thermal dose profiles induced by the found optimal treatment plan are shown in Fig. 6.1(d)–(f). We observe that the treatment of healthy tissue is equally distributed using the first weight (see Fig. 6.1(d)), while the other two solutions induce more overtreatment at the bottom of the target (Fig. 6.1(e)–6.1(f)). The found treatment times and overtreatment values are shown in Table 6.1, where the publication result is marked with a star (*). The amount of overtreatment is measured with the Dice coefficient d between all the ablated tissue points and the target size. If there is no overtreatment, the ablated tissue points and the target coincide, resulting in a Dice coefficient of 1. To have an increasing measure for increasing overtreatment, we calculated $1 - d$. We observe that not only the treatment time, but also the amount of overtreatment is the lowest with the first weight.

Table 6.1: Treatment time and overtreatment corresponding to the different weights.

Weight	Treatment Time [no. of breathing cycles]	Overtreatment [1−Dice]
1*	67	0.097
2	71	0.132
3	77	0.321

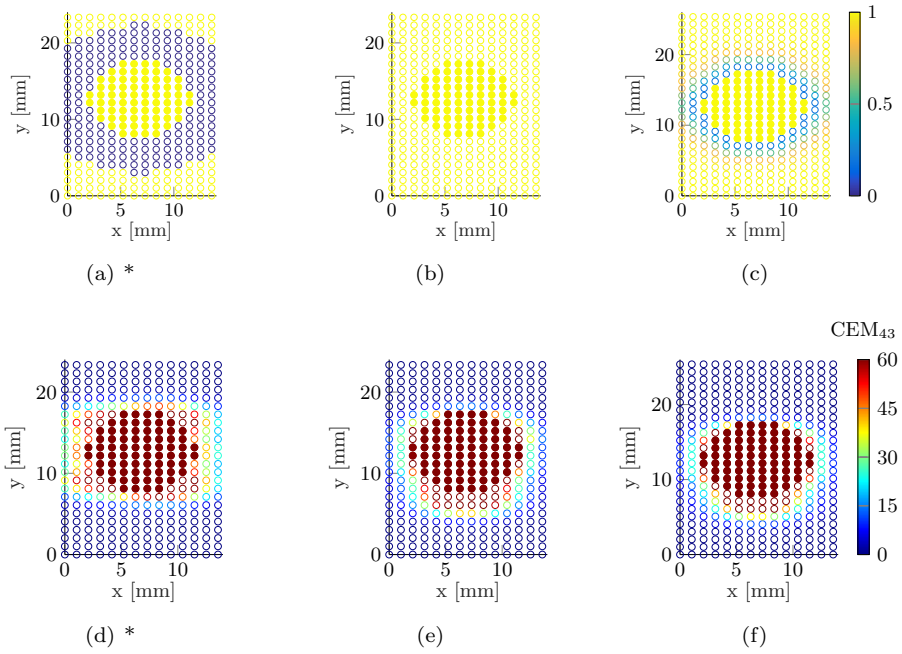

Figure 6.1: The influence of different weighting parameters w on the resulting thermal dose profiles. Filled circles correspond to target points, whereas non-filled points are healthy tissue. Results (a) and (d) are publication results. (a) – (c): three different weighting parameter choices, (d) – (f): induced thermal dose profiles by the optimal treatment plan according to the weight shown above.

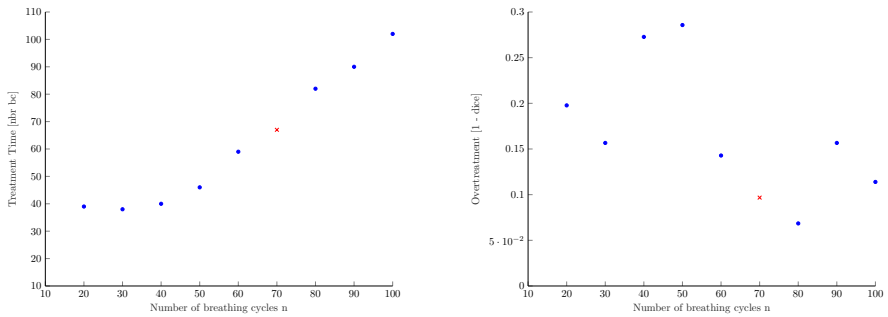

(a) (b)

Figure 6.2: The influence of the choice of n on the treatment time (a) and the amount of overtreatment (b). The red x marks the publication result. Note that the resulting treatment time can be larger than n due to the changing times. The changing times are described in more detail in this chapter's paper.

Treatment Horizon. As described in this chapter's publication, there is one treatment point $u^p(t)$ and m intensity values $u^I(t)$ per breathing cycle. However, it is not mentioned that the number of breathing cycles n has to be chosen manually. In fact, $u^p \in \mathbb{R}^{d\times n}$ and $u^I \in \mathbb{R}^{m\times n}$, where d is the dimension of the treatment points. In other words, a maximal treatment duration n has to be chosen before optimization. The choice of n has an influence on the treatment time and amount of overtreatment, as shown in Fig. 6.2. The treatment time increases with n, while the amount of overtreatment is decreasing. This indicates a trade-off between a short treatment time and a low amount of overtreatment. When minimizing the amount of overtreatment, we observe that $n = 80$ would yield the best result, while $n = 70$ gives the second best result. However, the treatment time is shorter using $n = 70$ compared to $n = 80$. Overall, $n = 70$ is a good compromise between a short treatment time and low overtreatment and was chosen for the publication. Nevertheless, other preferences, for example requiring a short treatment time despite higher amount of overtreatment, could lead to other choices of n.

Treatment Time. A straightforward method to measure the treatment time is to define it to be the number of breathing cycles during which the HIFU beam is on until the whole tumor is ablated. A way to do so is to penalize the sonication intensities which are greater than zero, resulting in the term

$$G_1(u) = \sum_i 1 - \delta_0(u^I(t_i)), \tag{6.3}$$

where δ_0 is the indicator function of 0. When comparing this equation to the first part of Eq. (6.2), we observe that the weighting by t_i is missing. We added the weighting

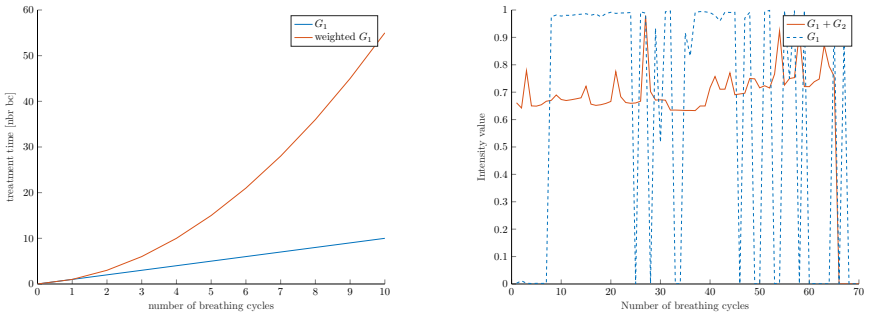

(a) (b)

Figure 6.3: (a): The treatment time of the weighted and non-weighted G_1, (b): optimizing with G_1 compared to the sum $G_1 + G_2$.

terms to have a nonlinear increase in the treatment time, which should result in shorter treatment times of the found sonication plan. The difference of the weighting is shown in Fig. 6.3(a). We can see that the term G_1 results in a linear increase of the treatment time, whereas the weighted G_1 gives a nonlinear increase.

One problem of the formulation given in Eq. (6.3) is that δ_0 is not continuous and is flat (i.e. has no gradient) for $u^I > 0$. A solution to this problem is to approximate δ_0 by the smooth function f_p

$$f_p := 1 - \exp\left(-px^2\right),$$

which converges to the indicator function for $p \to \infty$. During optimization, it is preferable to choose values of p that do not have vanishing gradients to avoid saturation during optimization.

Another problem of the formulation given in Eq. (6.3) is that the HIFU beam can be turned off before the end of the treatment without being penalized during the beam-off duration. This case should be avoided, as the following example shows. Assume that we have the following intensity values: $1, 0, 1$, where each intensity value corresponds to a breathing cycle. Then, the treatment duration is equal to 3, but G_1 would yield a treatment duration of only 2 as there are two non-zero intensity values. To avoid such cases, the zero intensities during the treatment, called *zero gaps*, should be penalized. To do so, we introduce the term

$$G_2(u) = \sum_i \max\left(\nabla u^I(t_i), 0\right). \tag{6.4}$$

As with G_1, the term G_2 is weighted by t_i.

Note that in the case of multiple successive *zero gaps*, like for example if the intensity is $1, 0, \ldots, 0, 1$, the term Eq. (6.4) does only penalize one of the zero entries instead of all. Despite this fact, the term G_2 seems to suffice to avoid *zero gaps*, as shown in Fig. 6.3(b). A possible explanation is that the *zero gaps* are removed successively until

none remains. For Fig. 6.3(b), optimal treatment plans using the weighted treatment time function G_1 and the weighted $G_1 + G_2$ were calculated. The intensity values of these solutions are shown over the whole treatment time for both cases. Using G_1, *zero gaps* are observed, in fact the treatment itself first starts at the 8-th breathing cycle. Moreover, towards the end of the treatment, the occurence of *zero gaps* increases. The amount of overtreatment is 0.301. However, when introducing the G_2 term, the appearance of *zero gaps* is avoided, resulting in a shorter treatment time and less overtreatment with 0.097.

7 A Feedback Algorithm for Self-Scanning

The publication of this chapter is based on the feedback algorithm and ex-vivo experiments on moving turkey muscle. The feedback algorithm calculates a treatment plan for the next time interval of duration Δt instead of calculating the whole treatment at once. As a result, the algorithm is able to adapt the planning to respiratory motion changes that occur during treatment. Moreover, the analytical temperature model used in Chapter 6 is extended such that it can model tissue inhomogeneities. The idea of the feedback algorithm is that not only the respiratory motion model is updated after each time interval, but also the temperature model is adapted to tissue inhomogeneities by incorporating the MR-thermometry measurements. In addition to the theoretical investigations of the proposed algorithm, ex-vivo experiments present the feasibility of the self-scanning approach. Turkey muscle is subjected to a respiratory-like motion pattern. We show that a uniform temperature rise can be induced in the presence of motion and tissue inhomogeneities.

Publication. The following publication was submitted to the journal *International Journal of Hyperthermia*.

Self-Scanning Treatment Planning for MRgHIFU: a Feedback Algorithm and Ex-Vivo Experiments

Nadia Möri [a], Laura Gui [b], Christoph Jud [a], Uri Nahum [a], Orane Lorton [b], Pauline Guillemin [b], Christoph D. Becker [b], Rares Salomir [b], Philippe C. Cattin [a]

[a]Center for medical Image Analysis & Navigation (CIAN), Department of Biomedical Engineering, University of Basel, Switzerland; [b]Faculty of Medicine, Radiology, University of Geneva, Switzerland

ARTICLE HISTORY
Compiled April 12, 2018

ABSTRACT
In noninvasive abdominal tumor treatment, research has focused on canceling organ motion either by gating or tracking the target. This paper's method is based on an alternative approach called self-scanning, which combines the advantages of the former methods: a static focus HIFU device and a high duty cycle. The self-scanning strategy leverages the organ motion by holding the focal spot of the HIFU device static for a given time, while it passively scans the target due to respiratory motion.

We present a feedback planning algorithm for the self-scanning method, which adapts the treatment plan continuously to nonperiodic respiratory motion. The used temperature model is constructed such that it can be online updated to tissue inhomogeneities by extracting them from temperature measurements.

We tested the proposed algorithm by simulation and compared it to the tracking method. We show that our method ensures complete target ablation under free-breathing while sparing healthy tissue in an inhomogeneous medium. The feedback planning method performs on par to the tracking approach regarding overtreatment, while the treatment time is slightly longer.

For a feasibility study, we performed MR-guided HIFU ex-vivo experiments on moving turkey muscle. The samples were continuously sonicated during a robot-driven movement inside the MR bore, where the sonication power was adapted to the motion to achieve a uniform temperature rise inside the samples. In addition, we physically verified our temperature model against PRFS multi-baseline thermometry and show that it can be adapted to tissue inhomogeneities and is able to accurately predict the thermal dose.

KEYWORDS
Self-Scanning, Treatment Planning, High Intensity Focused Ultrasound

1. Introduction

High intensity focused ultrasound (HIFU) is a well-known non-invasive thermal ablation modality for tumor treatment which is widely accepted for decades [1,2]. For image guidance during HIFU sonication, magnetic resonance imaging (MR) is often used [3–6]. In addition to the position and the motion of the tumor, MR provides temperature mapping as well [3]. With MR thermometry, the focal spot position and the heating procedure can be monitored. Further, the thermal dose is calculated to

determine the tissue damage [3,7]. MR-guided HIFU has been successfully applied for tumor ablation in immobile organs, such as uterus, prostate, breast and brain [3,8]. However, HIFU treatment of abdominal organs, such as kidney and liver, remains challenging due to respiratory motion and organ drift [9].

So far, research has focused on minimizing organ motion either by gating, breath holding or tracking of the target [10–13]. In the gating approach, an almost stationary part of the breathing cycle is exploited. Within a temporal window of 1-2 seconds, where the liver remains approximately still, the acoustic energy is periodically deposited [14]. The disadvantage of this method is the prolonged treatment time. Moreover, it neglects the motion during the gating-window. The tracking approach on the other hand is based on the idea of continuously readjusting the focal point position to the current tumor position in order to prevent both undesired tissue damage and energy spread [15–18]. The advantage of this method compared to the gated approach is the near 100% duty cycle, which results in a shorter treatment time [19]. However, in order to steer the focal spot of the HIFU device, a phased-array-transducer with hundreds of elements is required, each of which having its own amplifier. This complicates the electrical design of the device and is expensive. Moreover, the steering of the focal spot generates secondary lobes and the lateral steering causes an intensity decay at the focal spot [20].

A further challenge of the tracking approach is the prediction of the liver motion to actively steer the HIFU beam. There are two approaches to deal with that: indirect or direct motion tracking [10]. Indirect motion tracking takes advantage of the periodicity of the breathing motion. During a training phase, a motion model is created and later employed in a lookup table [18]. The advantage of this approach is the low latency. However, this method can not handle organ drift. In [16], they used a statistical exhalation drift model to compensate for organ drift. The idea of direct motion tracking is to detect the tumor in real-time and adjust the focal spot accordingly. Due to processing latency, the tumor position has to be anticipated to provide direct motion tracking [15,17]. In [13], they combined a population-based statistical motion model and information from 2D ultrasound sequences in order to predict the respiratory liver motion. In, [21], they used a non-linear Gaussian process regression method to predict organ motion based on a model-topology independent external respiratory signal.

As solid tumors are much larger than the focal spot of the HIFU device, ablating the whole tumor requires several treatment spots. The development of a sonication plan that reduces the treatment time and generates a uniform lesion has been addressed before in immobile tissue [22–25]. The basic idea in these approaches is to sonicate points in a regular grid. Different sequences of consecutive points are suggested, such as spiral pattern or raster scanning. To account for diffusion, the intensity and duration of focusing different points need to be adjusted. Using optimal control, not only the intensity and duration, but also the trajectory of the focal spot is optimized [26–28]. The main idea is to find optimal focal points with corresponding beam times such that a desired optimal thermal dose profile is achieved, while minimizing the treatment of healthy tissue and the treatment time.

For modeling the temperature induced inside the tumor, the thermal and acoustic properties of the tissue have to be known. The rate-of-heating method measures the ultrasonic absorption coefficient by observation of the temperature rise at the beginning of the heating period, which is assumed to be linear [29]. However, the method is limited to the short time at the beginning of heating before significant conduction takes place. The pulse-decay method accounts for heat conduction and beam

geometry [30]. In [31], they define the thermal load equation, which allows to fit the perfusion rate and energy absorption coefficient from temperature measurements. The diffusion coefficient is fitted by analysis of the spatial spread over time. However, the thermal load formula can not be applied for tissue inhomogeneities, as it assumes a constant absorption coefficient over space. In [32], they provide an analytical temperature model to determine the specific absorption rate (SAR), which can also be used for fitting the thermal properties of tissue. Although they evaluated their model in uniform tissue, it could also be applied for tissue inhomogeneities.

In this paper, we use the self-scanning method first introduced in [33], which takes advantage of the perpetual respiratory motion to passively scan the tumor. In other words, we are placing the static focal point of the HIFU into the tumor [33,34]. The motion caused by breathing shifts the tumor through this focal point. We anticipate at which time point tumor tissue is located under the focal spot and thus modulate the HIFU intensity based on this information. Once the tumor has been ablated along the self-scanned trajectory, the focal spot is relocated to a different but static position within the body. With this method, we combine the advantages of the gating and the tracking method: a HIFU device with a fixed focus and a high duty cycle. Moreover, since with the self-scanning approach no lateral steering of the focal spot is required, fewer secondary lobes are generated and position-dependent decay of the focal spot intensity during lateral steering is significantly reduced. Another benefit of the self-scanning approach is that the beam-forming problem through the ribs is simplified, as steering is not needed. However, this comes at the cost of an increased complexity at the planning stage.

In the following, we present a *feedback algorithm* for the self-scanning approach that is capable to continuously incorporate changing respiratory motion patterns and tissue inhomogeneities. The proposed algorithm relies on a model that predicts the respiratory organ motion. Moreover, using MR-thermometry measurements, the tissue inhomogeneities are extracted and integrated into the temperature model. Taking advantage of the online updated motion pattern and tissue properties, the algorithm updates the treatment plan progressively by optimizing an optimal control problem similar to the method introduced in [34]. The novelty of the proposed method compared to previous work in [33,34] is that it is based on a temperature model which includes tissue inhomogeneities, whereas they assumed homogeneous tissue. The temperature model is designed such that it can adapt itself online to the measured temperature data and is more and more fitted to a specific inhomogeneous tissue and is able to accurately predict the thermal dose. Moreover, the *feedback algorithm* can handle dynamic and nonperiodic respiratory motion. Overall, the proposed algorithm is a step in the direction of online self-scanning treatment planning. We showed by simulation that the *feedback algorithm* provides feasible treatment plans for the self-scanning approach, which can handle nonperiodic respiratory motion pattern as well as tissue inhomogeneities. We compared the treatment time and the amount of overtreatment to the tracking approach. The self-scanning approach induces only few overtreatment. The overtreatment performs on par to the one observed with the tracking approach, while the treatment time is slightly longer.

Furthermore, to show the feasibility of the self-scanning approach, we performed ex-vivo experiments on turkey muscle samples. The samples were moved by an MR-compatible robot arm to mimic respiratory motion, while the HIFU device continuously sonicated with a precalculated intensity. We showed that using modulated intensity values, a nearly uniform temperature rise could be induced inside the samples. Moreover, we showed that our temperature model is able to handle respiratory

motion and can accurately predict the thermal dose map in the presence of tissue inhomogeneities.

2. Methods

The task of planning a treatment is to find an optimal treatment plan u which ensures that the whole target is ablated while sparing healthy tissue. Moreover, the goal in this work is to adapt the treatment plan during sonication for incorporating nonperiodic respiratory motion and adapt to tissue inhomogeneities. In the self-scanning approach, the focal spot is static during a time interval of duration Δt, called *planning interval*. During this phase, different tissue will pass through the focal spot due to respiratory motion. The HIFU system used for the self-scanning approach is able to electrically steer the focal spot rapidly in depth along the acoustic axis. For the other directions, slower mechanical displacement is applied. In the proposed algorithm, we will start the treatment with an initial sonication point and replan after each Δt newly to adapt to the possibly changed respiratory motion. If the calculated sonication point requires a mechanical change of the HIFU device, the treatment is interrupted for repositioning of the device, called changing time. Moreover, using MR-thermometry measurements, the temperature model is continuously adapted to tissue inhomogeneities. To the best of our knowledge, the concept of updating the model itself during optimization is a new concept in HIFU treatment planning. The advantage of this method is that tissue inhomogeneities, which are patient specific and unknown before treatment and become first visible during the temperature measurements [22], can be included into the modeling and planning. Moreover, as the tissue parameters change during heating [35], this parameter development can be incorporated into the model.

In the following, we will explain the proposed algorithm in more detail. First, we describe the temperature model and how it can be adapted to tissue inhomogeneities. Then, the optimization problem to derive the optimal treatment plan is described.

2.1. *Temperature Model*

Pennes Bioheat Equation. The temperature inside the body can be described by Pennes bioheat equation [36]:

$$\frac{\partial T(p,t)}{\partial t} = D\nabla^2 T(p,t) - bT(p,t) + KQ(p,t), \tag{1}$$

where $T(p,t)$ and $Q(p,t)$ are the temperature rise and the heat source at a given point p and time t, respectively. Moreover, $D = \frac{\kappa}{\rho c}$, where κ is the thermal conductivity, ρ the density, and c is the specific heat of tissue. Furthermore, $b = \frac{wc_b}{\rho c}$, with w the perfusion and c_b the specific heat of blood, and $K = \frac{1}{\rho c}$. The first term represents the rate of change in heat content, the second conduction, the third is the perfusion heat transfer, and the fourth is the heat source.

Static Heat Source. Following [28], we assume that the temperature rise as well as the heat source of a static HIFU beam are Gaussian. This means that no conduction occurs during the heating period, which is reasonable for short heating periods. In this case, a closed form solution can be found to Pennes bioheat equation [28]. If point

$q = (q_r, q_z)$ in cylindrical coordinates is sonicated during a time period of $\Delta\tau$ with sonication intensity I, the induced temperature at point $p = (p_r, p_z)$ and time $t \geq \Delta\tau$ is

$$T_{\mathrm{s}}(p, t; q, \Delta\tau, I) = \frac{T_{\mathrm{peak}}\theta_r^2(\Delta\tau)\theta_z(\Delta\tau)e^{-bt}}{\theta_r^2(t)\theta_z(t)} \exp\left(-\frac{(p_r - q_r)^2}{2\theta_r^2(t)} - \frac{(p_z - q_z)^2}{2\theta_z^2(t)}\right), \quad (2)$$

where the functions θ_r and θ_z are defined as

$$\theta_i(t) = \sqrt{2Dt + \sigma_i}, \quad i \in \{r, z\}.$$

Here, σ_r, σ_z are the focal spot sizes of the HIFU device in radial r and axial z direction, respectively. Further, T_{peak} denotes the maximal induced temperature which is attained at the focal spot q after a sonication duration of $\Delta\tau$ and is given by

$$T_{\mathrm{peak}} = 2\alpha I K \sigma_r^2 \sigma_z \int_0^{\Delta\tau} \frac{\exp(-b\tau)}{(\sigma_r^2 + 4D\tau)\sqrt{\sigma_z^2 + 4D\tau}}\, d\tau, \quad (3)$$

where α is the intensity absorption coefficient of tissue. The derivation of the closed-form solution to the bioheat equation (1) is derived following [28] and is explained in more detail in the appendix.

Moving Heat Source. In our case the HIFU beam is not static but moving due to respiratory motion. To model the moving heat source Q_{m}, we discretize in time and approximate it as a sum of static heat sources $Q_{\mathrm{s}}^{q_i}$.

$$Q_{\mathrm{m}}^{\Delta\tau}(t) = Q_{\mathrm{s}}^{q_i}(t), \quad t \in \big[(i-1)\Delta\tau, i\Delta\tau\big),\ i \geq 1, \quad (4)$$

where $Q_{\mathrm{s}}^{q_i}$ denotes a static heat source of constant ultrasonic intensity placed at point q_i and of sonication duration $\Delta\tau$. Hence, we assume that during the i-th time interval of duration $\Delta\tau$, the heat source is static. When taking $\Delta\tau \to 0$, the heat source $Q_{\mathrm{m}}^{\Delta\tau}$ defined in (4) converges to the continuously moving heat source Q_{m} as schematically shown in Fig. 1. Considering the above discretization and as Pennes bioheat equation is linear in T, the temperature rise induced by $Q_{\mathrm{m}}^{\Delta\tau}$ can be written as

$$T(p, t) = \sum_i T_{\mathrm{s}}(p, t; q_i, \Delta\tau, I_i), \quad (5)$$

where $T_{\mathrm{s}}(p, t; q_i, \Delta\tau, I_i)$ denotes the solution to Pennes bioheat equation for the static heat source $Q_{\mathrm{s}}^{q_i}$ with ultrasonic intensity I_i given by Eq. (2) and (3).

2.2. *Tissue Inhomogeneities*

The temperature model described by Eq. (2) and (3) assumes that the tissue has homogeneous properties, i.e. it assumes that the parameters D, b, α and K are constant over the tissue domain and over the whole treatment time. But in reality, this is usually not the case. Not only that tissue properties vary spatially, but they also alter during heating as tissue changes its properties while undergoing necrosis [35]. In this section,

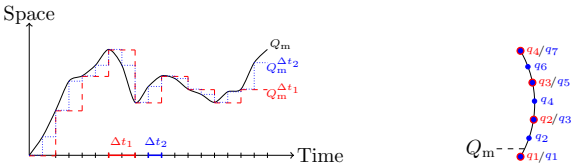

Figure 1. Discretization of the moving heat source Q_m. Left: Discretization of the heat source over time, the ordinate denotes the tissue space and the abscissa the time. The continuous heat source Q_m is shown in black solid line, the dashed red and dotted blue curves represent the discretization for $\Delta\tau_1$ ($Q_\mathrm{m}^{\Delta\tau_1}$) and $\Delta\tau_2$ ($Q_\mathrm{m}^{\Delta\tau_2}$), respectively. Right: Discretization of heat source shown in space. The black line represents a simplified respiratory trajectory in $\mathbb{R}^2$, the red and blue dots represent the discretized sonication points q_i. As before, blue represents a finer (i.e. smaller $\Delta\tau$) discretization than red.

we show how the temperature model can be adapted to tissue inhomogeneities by considering non-constant tissue properties.

In the temperature model described by Eq. (2) and (3), there are three parameters that might change over space and time: the diffusion parameter D, the perfusion b and the parameter $a := \alpha K$. In our ex-vivo experiments, there is no perfusion and hence we set $b = 0$. Moreover, as the diffusion coefficient D measures the rate of heat transfer, which is rather a global than a local process, we assume that D does not vary over space and time. Thus, the temperature can be written as a function of a_p, where the subscript p denotes the space dependency of parameter a.

$$T(a_p) = a_p f(p, t), \tag{6}$$

where the closed form of function f can be derived from Eq. (2). Given temperature measurements at point p in the image domain at measurement times $\{t_i\}_i$, the parameter a_p is fitted for each point, to which we refer as *point correction* in the further of this paper. Note that this is a linear regression problem. On the contrary, when fitting the parameter $a = \alpha K$ for the whole tissue domain, we refer to *overall correction* in the following.

2.3. *Thermal Dose*

The most accepted model to determine how tissue is affected by temperature is described by the thermal dose model [37].

$$C(p, t) = \int_0^t R^{43 - T(p,\tau)} d\tau, \tag{7}$$

where the constant R depends on the temperature T as follows

$$R = \begin{cases} 0, & T < 39°\mathrm{C}, \\ \frac{1}{4}, & 39°\mathrm{C} \leq T \leq 43°\mathrm{C}, \\ \frac{1}{2}, & 43°\mathrm{C} \leq T. \end{cases}$$

The thermal dose equation estimates the cumulative equivalent minutes at a temperature of 43°C (CEM_{43}). Studies showed that the threshold thermal dosage for tissue to undergo necrosis is between 50 and 240 CEM_{43}, depending on the tissue type [38].

2.4. *Optimal Control Problem*

The idea of the *feedback algorithm* is to update the treatment plan for every time interval of duration Δt, which we call *planning interval* in the following. A treatment plan u consists of a sonication point and m corresponding intensities. During each *planning interval*, the HIFU device will focus the current sonication point while the tissue underneath the focal spot moves through by respiratory motion. The intensity values will change every $\frac{\Delta t}{m}$ seconds to adapt to the motion pattern, which allows a more accurate temperature control. The aim of the optimization problem is to find an optimal treatment plan u for each *planning interval* that maximizes the ablated target tissue volume while minimizing treatment of healthy tissue. The treatment plan u induces a temperature rise T_u inside the tissue, which is calculated by the temperature model given by Eq. (5). As we want to prevent tissue from boiling, we request that a given maximal temperature rise T_m can not be exceeded. From the temperature rise T_u, the thermal dose C_u can be derived to obtain how the tissue is affected by Eq. (7). To find such a treatment plan u, we solve the following multi-objective optimization problem:

$$\begin{aligned} u^* = \arg\min_u \quad & \frac{w_1}{n_1}\|C_u - C_\mathrm{opt}\|_2 \\ & + \frac{w_2}{n_2}\sum_{p\in\Omega}\left(\mathcal{P}_+[C_\mathrm{opt}(p) - C_u(p)]\right)^2 \\ & + \frac{w_3}{n_3}\sum_{p\in\Gamma}\mathcal{P}_+[T_\mathrm{opt} - T_u^\mathrm{max}(p)], \\ \text{subject to } & T_u^\mathrm{max} \le T_\mathrm{m}, \end{aligned} \tag{8}$$

where $\|\cdot\|$ is the ℓ_2-norm, $\mathcal{P}_+[x] := \max(x, 0)$ is the projection onto the positive axis (i.e. $\mathbb{R}_+ = \{x \in \mathbb{R} : x \ge 0\}$) and the maximal temperature attained during treatment at a point p is denoted by $T_u^\mathrm{max}(p) := \max_t T(p,t)$. The current induced thermal dose profile is denoted by C_u, the desired dose profile is C_opt, and T_opt is the desired minimal temperature rise. Moreover, Ω denotes the tissue domain, and $\Gamma \subset \Omega$ is the target to be ablated. The parameters w_1, w_2, and w_3 are the weights of the different objectives, their selection is discussed in Section 4.1. The weights n_1, n_2, and n_3 are the normalization factors and are chosen to be the evaluation of the corresponding objective at the initial value u_0, as an example $n_1 = \|C_{u_0} - C_\mathrm{opt}\|_2$.

The optimization problem defined in Eq. (8) is defined as a sum of three objectives. The first objective corresponds to the difference of the current induced thermal dose profile C_u to the desired profile C_opt. The desired profile is defined to be the lethal thermal dosage inside the target, while at healthy tissue it is defined to be 0. The second objective penalizes each target point that is not yet ablated. In this way, the objective gets smaller the more target points are ablated and thus the optimizer is guided towards a solution that ablates the whole target. Further, the third objective ensures that the temperature inside the target is close to or higher than the desired minimal temperature rise T_opt. When choosing T_opt properly, the induced thermal dose will be close to the lethal thermal dose. The choice of T_opt is explained in Section 3.1.

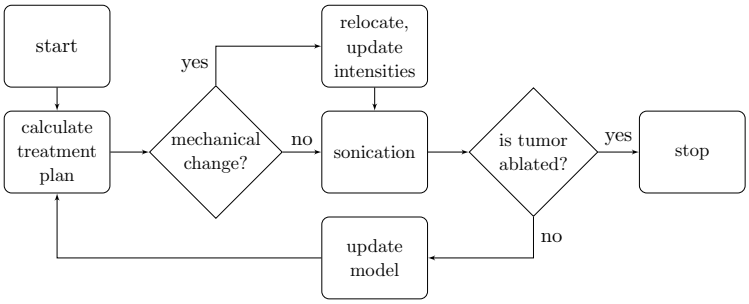

Figure 2. Flow chart of the proposed *feedback algorithm*.

2.5. *Feedback Algorithm*

Now that we defined the optimization problem to calculate a treatment plan during a *planning interval*, we can explain in more detail how the proposed *feedback algorithm* works. In the following, a theoretical description of the *feedback algorithm* is presented. First, a motion pattern is predicted for the next *planning interval* of duration Δt. In principle, any motion model can be used to predict the motion. In this work, we focus on how to plan a treatment, where we assume that a motion model is given. Then, the initial treatment plan u^* is calculated by optimizing Eq. (8). During the first *planning interval*, u^* is executed, while simultaneously the induced temperature rise is measured with MR-thermometry. In the next step, we take advantage of the new gained information to update the temperature model and integrate tissue inhomogeneities by performing a *point correction* as described by Eq. (6). Note that the temporal resolution of the motion prediction and the intensity change is not the same if $m > 1$. In these cases, the algorithm is able to compensate possible different velocities occurring in the motion prediction by adapting the intensity values.

The thermal dose map C_u is updated by applying Eq. (7) to the temperature measurements. Additionally, we predict the accumulated thermal dose for the future. The thermal dose accumulates over time until the temperature rise is below $+2°$C, where the dose accumulation stops. Hence, the long term effect of the treatment has to be included in the planning phase to avoid overtreatment and treatment elongation, which is done by considering the thermal dose not only retrospectively, but also prospectively. Thus, the thermal dose C_u in the optimization framework Eq. (8) also includes the future thermal dose accumulation.

Last, the motion pattern is predicted for the next *planning interval*. If the target is not yet ablated, i.e. the minimal thermal dose inside the target is below the lethal dosage, a new treatment plan is calculated for the next *planning interval*. Again, the problem given in Eq. (8) is solved. The induced thermal dose C_u and the maximal induced temperature rise $T_u^{\max}$ are calculated over the whole treatment time (and in case of C_u also prospectively). If the recalculated sonication point does not lie on the acoustic axis of the current HIFU position, the HIFU device has to be changed mechanically. During this time, the sonication is interrupted. As the respiratory motion might change again, the sonication intensities are recalculated and adapted to the changed motion. After the mechanical change is executed, the sonication is continued. The procedure is iterated until the whole target has been ablated. A flow chart of the

feedback algorithm can be seen in Fig. 2. Note that the target and the optimal thermal dose profile C_{opt} can be adapted to a safety margin around the tumor.

The proposed optimization problem defined in Eq. (8) is similar to the one proposed in our previous work [34], where we used an optimal control approach to find a treatment plan for a self-scanning approach. The whole treatment plan was optimized at once and was found in two steps: first, the temperature rise, and in the second step the thermal dose was optimized. The main difference from our previous method to the proposed *feedback algorithm* in this paper is that the treatment time is not optimized in the *feedback algorithm*. Here, the treatment time is automatically found during optimization, as we iteratively find new sonication points until the whole tumor is ablated. This means that we do not know a priori how long the treatment time will be. Basically, the treatment plan is updated as long as the target is not yet ablated, and the treatment stops as soon the whole target is ablated. Moreover, the number of parameters in the proposed *feedback algorithm* is dramatically reduced, which makes the optimization problem given in Eq. (8) easier to solve and we do not need two steps to find an optimal solution. Hence, the thermal dose can be optimized directly. We include the third objective in Eq. (8) to support the optimization algorithm to find an optimal solution. The proposed optimization problem can be viewed as a fusion of the two optimization problems proposed in our previous work [34].

3. Materials

3.1. *Simulations*

We applied the proposed *feedback algorithm* on a scenario with a circular ablation region and compared our dose maps to the classical tracking approach. We investigated the influence of motion prediction uncertainties as well as the influence of inaccurately fitted inhomogeneity parameters. Furthermore, the effect of different perfusion and absorption coefficients on the treatment time and the amount of overtreatment were analyzed. We simulated three different settings, which are described in the following.

We compared our *feedback algorithm* to the same problem as in our previous work in [34], which we call *comparing simulation*. We used a sine-shaped motion with an amplitude of 6 mm and a period of 4 s during the whole treatment and no tissue inhomogeneities. The tissue domain was $\Omega_1 = 15\,\text{mm} \times 24\,\text{mm}$, and the target was set to be a circle with radius $r = 5\,\text{mm}$. The heat source discretization is $\Delta\tau = 0.4\,\text{s}$, the *planning interval* is 4 s and the number of intensity values per *planning interval* is $m = 10$.

For a bigger 2D problem, we defined the tissue domain to be $\Omega_2 = 30\,\text{mm} \times 50\,\text{mm}$, with a circular target of radius $r = 10\,\text{mm}$. Furthermore, we tested the algorithm on a 3D problem with a tissue domain of $\Omega_3 = 20\,\text{mm} \times 30\,\text{mm} \times 10\,\text{mm}$, the target was defined to be sphere with a radius of $r = 7\,\text{mm}$. For both problems we used a heat source discretization of $\Delta\tau = 0.1\,\text{s}$ to model the moving heat source $Q_{\text{m}}^{\Delta\tau}$, and the number of intensity values per *planning interval* was $m = 20$, where the *planning interval* was 4 s. Note that the heat source discretization $\Delta\tau$ is not directly related to the *planning interval*. For these two problems, we considered nonperiodic motion with different noise levels, which is described below.

For all simulation experiments, we set the optimal temperature rise inside the target $T_{\text{opt}} = +18°\text{C}$, while outside the target it was set to zero. Note that if a minimal temperature rise of $+18°\text{C}$ is achieved at a tissue point, it is very likely that it will be

Table 1. Parameters for the sampling of the respiratory motion pattern, which is given as $x\sin(2\pi t/y)+zt$ per *planning interval*. The values σ and μ denote the standard deviation and the mean of the Gaussian distribution, respectively, cov is the covariance over time, and noise represents the standard deviation of a Gaussian with $\mu = 0$ used for noise sampling.

	x [mm]				y [s]				z [mm/s]			
Noise level	σ	μ	cov	noise	σ	μ	cov	noise	σ	μ	cov	noise
η_0	6	4	2	0	4	3	2.9	0	0	1	0.9	0
η_1	6	4	2	2	4	3	2.9	0.05	0	1	0.9	0.2
η_2	6	4	2	5	4	3	2.9	0.05	0	1	0.9	0.5

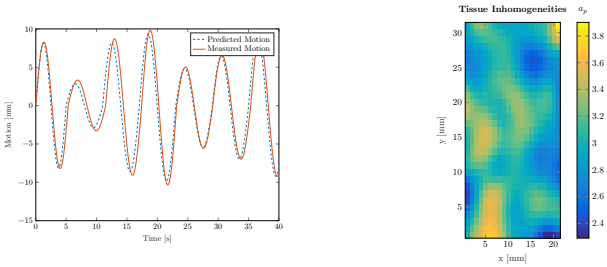

Figure 3. Examples for motion (left) and tissue inhomogeneities (right) samples for noise level η_2 used in the *noise simulations*.

ablated [39]. Moreover, the maximal allowed temperature rise to be $T_\mathrm{m} = +50°\mathrm{C}$, the lethal thermal dose was set to $120\,\mathrm{CEM}_{43}$ (which is the lethal dose for muscle [40]), and the thermal dose was calculated for 2 *planning intervals* into the future. The sonication point starting value of the optimization problem was set to be the median point of not yet treated target points, and the intensities are set to be the maximal allowed intensity, which is normalized such that an intensity of 1 W / mm^2 during 10 s induces a temperature rise of 34°C.

For the irregular motion pattern, we assumed that during each breathing cycle the motion is of the form $x\sin(2\pi t/y) + zt$, where x corresponds to the motion depth, y is the breathing cycle duration, z corresponds to organ drift, and t denotes the time. The parameters x, y and z are each sampled from the Gaussian normal distribution. Moreover, to simulate that the predicted may differ from the observed motion pattern, Gaussian noise is added to the parameters x, y and z to simulate the inaccuracy of the motion model. In Table 1, the parameters for sampling the values are shown and Fig. 3 shows an example of a motion sample.

The tissue inhomogeneity parameter a_p is sampled from the Rayleigh distribution and then shifted by a constant offset. To have continuous inhomogeneity maps, the resulting parameters are smoothed by a Gaussian. To simulate errors in fitting the inhomogeneities parameters, we added some noise on the inhomogeneities map and assumed that after a given number of temperature measurements, the error will converge to zero. The number of measurements needed until convergence was sampled for each point from the Rayleigh distribution and shifted by a constant offset. The noise on the inhomogeneities map was sampled from the Gaussian distribution, and both the convergence and noise maps are smoothed with a Gaussian. The observed tissue inhomogeneity a_p at a given point p will then linearly converge from the noisy to the exact inhomogeneity value, and will coincide to the exact value after the number of measurements indicated in the convergence map. The parameters for sampling

Table 2. Parameters for the sampling of the tissue inhomogeneity coefficient a_p. The value σ_R denotes the Rayleigh distribution parameter, which is shifted by the parameter shift. The values μ_G and σ_G define the mean and variance of a Gaussian, respectively. For noise level η_0, we chose a constant value of $a_p = 3$ over the whole domain, which is denoted by σ_R = - and shift = 3.

	Tissue inhomogeneity		Error		Convergence		Gauss filter
Noise level	σ_R	shift	μ_G	σ_G	σ_R	shift	σ_G [mm]
η_0	-	3	0	0	20	10	2
η_1	2	0.56	0.2	0.5	20	10	2
η_2	2	0.56	0.4	0.5	20	10	2

the values are shown in Table 2, and an example of a tissue inhomogeneity sample is shown in Fig. 3.

For the *noise simulations*, each of the three different problems Ω_1, Ω_2, and Ω_3 was optimized with the three different noise levels of the motion and inhomogeneities pattern η_0, η_2, and η_3. The noise level η_0 means a homogeneous tissue without noise on a_p and nonperiodic motion pattern without noise. For the noise levels η_1 and η_2, nonhomogeneous tissues are considered, and noise is added to the motion and inhomogeneity values. To consider the randomness of the sampled motion and inhomogeneity maps, each of the random patterns was sampled three times. This means that for a given domain Ω_i, and given noise level η_j, three simulation were calculated, each with different samples of inhomogeneity and motion patterns from the same distribution. Each of these simulations was performed for the self-scanning and the tracking approach.

For the *comparing simulations* to previous work in [34], we used a different parameter a_p than in the *noise simulation*. The reason is that in the *noise simulations* we used the parameters which were in the range of the values that we observed int the ex-vivo experiments, whereas in [34] the parameters of a tissue mimicking gel were used. We noticed that the values examined in the ex-vivo experiments were about three times higher compared to the ones measured with the tissue mimicking gel. To simplify, we express the value a_p relative to the *comparing simulation*, meaning that in these we used a relative $a_p = 1$, where as in the other simulations we used a relative $a_p = 3$.

To investigate the influence of varying a_p values on the treatment time and overtreatment, we performed simulations on a homogeneous tissue with a_p ranging from 1 to 4 for a nonperiodic motion pattern without noise, i.e. we assumed the motion to be known (noise level η_0). We performed this simulation for both the tracking and the self-scanning approach and call it *absorption simulation*.

In addition, we investigated the effect of different perfusion parameters on the amount of overtreatment and treatment time. We performed simulations on a homogeneous tissue with $a_p = 3$, for motion patterns of noise level η_0, meaning that we simulated nonperiodic motion patterns without noise. This simulation was performed for both the self-scanning and tracking approach, and is called *perfusion simulation*.

We compared our self-scanning approach to the tracking approach, where the motion is compensated by steering the focal spot of the HIFU device. The intensity decay at the focal spot due to steering is modeled to be a Gaussian in radial direction with a deviation of 12 mm, and optimal treatment plans are obtained with the proposed *feedback algorithm* adapted to tracking.

3.2. *Ex-Vivo Experiments*

For a proof of concept, we performed ex-vivo experiments to show that we are able to induce a near uniform temperature elevation inside moving tissue. We also evaluated

the performance of our temperature model and show that it can be adapted to tissue inhomogeneities as a two step treatment procedure. Moreover, we evaluated the performance of the temperature model not only by evaluating the temperature, but also the thermal dose.

Ex-vivo turkey breast tissue samples cylindrically shaped were moved by an MR-compatible robot (Innomotion), which induced a breathing-like periodic motion [41]. The displacement of the motion was 21 mm in the cranio-caudal direction, mimicking general anesthesia with controlled breathing. The motion pattern of the robot is shown in Figure 4. The motion pattern was extracted before sonication from MR-images. HIFU sonication was achieved with an MR-compatible 256-element randomized phased-array transducer (Imasonic, France, operating frequency 1031 kHz, natural focal length 130 mm, aperture 140 mm), coupled to the tissue samples through a bath of degassed water and driven by a 256-channel beam former (Image Guided Therapy, France). Temperature elevation was monitored online with a 3T MRI-scanner (Prisma Fit, Siemens, Germany) equipped with a receive only single element loop coil (11 cm diameter) in the coronal plane. 3D planning was achieved with high resolution T1-w sequences (0.8 mm isotropic voxel) freezing the motion of the robot. The MR thermometry slice was positioned coronal in the focal plane and was normal to the beam axis and parallel to the tissue motion axis. A multi-baseline time-referenced PRFS temperature-sensitive method was used off-line as described further. Main acquisition parameters were: FOV 128 mm square, voxel size $1.04 \times 1 \times 5\,\mathrm{mm}^3$, phase encode direction LR, TR/TE/flip angle = 90 ms, 10.2 ms/20°, EPI factor 13, bandwidth 1184 Hz/ pixel, spectral pulse fat saturation. Synchronization of the initial time point of each breathing with the respective cycle-specific pre-calculated acoustic power table was performed using an in-bore MR-compatible optical camera according to Auboiroux et al [14]. The camera was continuously monitoring at 30 fps a high contrast sight attached to the robotic arm. An optical flow algorithm implemented under OpenCV interface tracked the sight and generated a displacement curve. The onset of the robotic arm motion in the positive direction triggered the execution of a cycle-specific HIFU sonication according to a power table, which is described below.

In order to obtain MR thermometry maps, two kind of motion-related artifacts have to be taken into account: intra- and inter-scan features. Intra-scan artifacts were not detected when the position of the robot arm reached the proximal and distal stops, that is, still images. These images were further used with a multi-baseline method to generate artifact-free temperature maps. On the other side, during the robotic arm course between the stops, the MR images contained typical ghosting artifacts and were discarded, approximately 50% of images.

In order to sort the MR images in two categories, distal and proximal stops of the robot motion, the moving tissue was automatically segmented from the magnitude data with a thresholding method and the dynamic measurements where the tissue was still were identified and used to calculate two interleaved series of temperature maps by choosing the appropriate reference from a baseline atlas consisting of approximately 30 images per category. These maps at distal and proximal stops of the robot motion were roughly registered by applying a shift that made coincide the positions of the center of mass of the segmented tissue among dynamics. Subsequently, the temperature maps were corrected for background phase drift using three unheated ROIs for each time frame similar to [23], and their alignment was finally refined by a rigid registration (rotation and translation). As a last step temperature maps corresponding to the tissue moving intervals were computed by linear time interpolation from the temperature maps of the still dynamics.

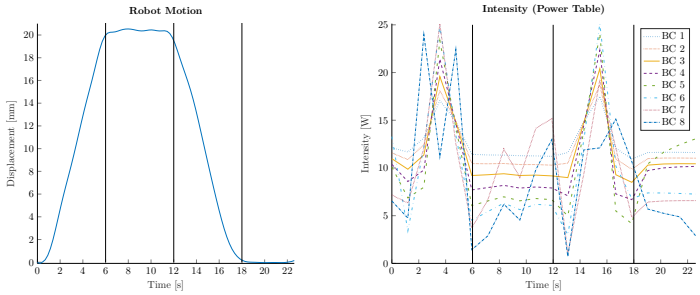

Figure 4. The robot motion (left) and the calculated intensity values, which are used as power tables (right). Here, BC stands for breathing cycle. For a better comparison between the two plots, we added vertical lines at 6, 12 and 18 seconds. The intensity values are higher at high velocity parts of the motion, and lower at low velocity.

Two different kind of ex-vivo experiments were performed in independent experiments: 1) single focal point sonication with HIFU power updated every 1.16 s according to pre-calculated power tables, and 2) two interleaved foci (switching period 0.58 s, electronic steering perpendicular to the motion direction at $+/-5$ mm lateral location). Sonication was done in 8 successive breathing cycles for a total period of approximately 180 s, which was pre-defined before the experiment.

For both independent experiments, two kinds of power tables were used: *power-compensated* and *non-compensated*. For the *non-compensated* ones, we used constant power during each breathing cycle. For the single focal spot *power-compensated* sonications, we optimized the sonication intensity using the following optimization problem:

$$u_{\mathrm{I}}^{*} = \arg\min_{u_{\mathrm{I}}^{*}} \sum_{p\in\Gamma} \left(T_u^{\max}(p) - T_{\mathrm{opt}}(p)\right)^2, \tag{9}$$

where u_{I} denotes the sonication intensities, and Γ is the trajectory of the focal point in the tissue's coordinate system due to robot-induced motion. The parameters defining the temperature T were extracted from MR-measurements, similar to [34]. The resulting intensity values u_{I}^{*} were then exported and used as power tables. We used $m = 20$ intensity values per cycle. For the two interleaved foci, we took the same power tables, but alternated between the two focal spots, which gave a total of $m = 40$ intensity values per cycle. In the *non-compensated* cases, the tissue was sonicated with the same total energy as compared to the *power-compensated* approach, but the intensity was held constant over time. The motion pattern of the robot arm and the calculated intensity values are shown in Figure 4.

In a separate experiment which we call *tissue inhomogeneities experiment*, we used the MR-temperature measurements to re-calculate the power tables to include the in-situ inhomogeneities observed in the thermal patterns. The recalculated power tables were used as in the *power-compensated* experiment on a cycle per cycle base.

Note that the above approach is a simplified version to the optimization problem given in Eq. (8), with $w_1 = w_2 = 0$. Moreover, the objective function corresponding to weight w_3 is altered such that the difference between the desired and induced temperature rise is optimized. This means that we do not consider the thermal dose ($w_1 = w_2 = 0$), and the target Γ is given to be the trajectory of the focal spot. As

we optimize the temperature, the problem is less challenging compared to thermal dose optimization. Due to the fact that the sonication point is fixed (which is given by the experimental setup), the problem is further simplified as the number of variables decreases. However, for a proof of concept, it suffices to show that a uniform temperature elevation can be established as this will induce a lethal thermal dose if the temperature is high enough.

3.3. *Evaluation Measures*

Overtreatment. To calculate the amount of overtreatment, the dice coefficient d between all the ablated tissue points and the target size was calculated. In a perfect case, where there is no overtreatment $d = 1$ as the ablated tissue points will exactly be the target points and thus both sets coincide. To have a measure which becomes greater with increasing overtreatment, we calculated $1 - d$.

Regression Slope. To evaluate how well the MR-thermometry measurements and the simulation values correspond to each other, we calculated the correlation and what we call the regression slope. A linear regression between the measurements and the simulation values gave the regression slope. A correlation value of 1 together with a regression slope of 1 would mean that the simulation fits the measurements very well. A regression slope of 0.5 means that the simulation values have to be multiplied by a factor of 2 to get the measurement results.

4. Results

4.1. *Simulations*

To know which weighting parameters w_1, w_2, and w_3 should be chosen, we performed a parameter search on Ω_1 with constant motion and no tissue inhomogeneities. We searched over the parameters $w_1, w_2, w_3 \in \{0, 0.2, \ldots, 1\}$ for the self-scanning and tracking approach independently. For each parameter set, we evaluated the performance regarding the amount of overtreatment and the treatment time. For the self-scanning approach, we found the best parameter set which minimizes the treatment time to be $w_1 = 0.8$, $w_2 = 0.4$ and $w_3 = 1$, where the parameters which minimized overtreatment were $w_1 = 0.8$, $w_2 = 0$ and $w_3 = 0.2$. For the tracking approach we observed different optimal parameters, which were $w_1 = 1$, $w_2 = 0.8$ and $w_3 = 0.2$ for minimal overtreatment, and $w_1 = 0.2$, $w_2 = 1$ and $w_3 = 0.2$ for minimal treatment time. We call the optimal parameter sets which optimize overtreatment *ot* and the ones that minimize treatment time *tr* in the following.

In the previous work done in [34], we achieved treatment times of 67 and 68 time intervals for the self-scanning and the tracking approach, respectively. With the proposed *feedback algorithm*, we achieved a treatment time duration of 35 time intervals, and a treatment time of 8 time intervals for the tracking approach in the *comparing simulation*.

When comparing the results of the tracking and self-scanning method computed with the *feedback algorithm*, we observe that the treatment time is much longer with the self-scanning approach. However, when looking at the results shown in Table 3 achieved with the *noise experiments*, we observe that the difference becomes smaller, especially with the *ot* parameters. The reason for this effect is the absorption coeffi-

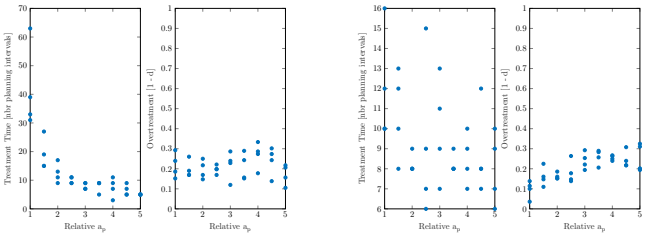

Figure 5. Results of the *absorption simulation*: The influence of different relative values of a_p as defined in Eq. (6), on the treatment time and the amount of overtreatment. The four values represent four different motion samples of noise level η_0.

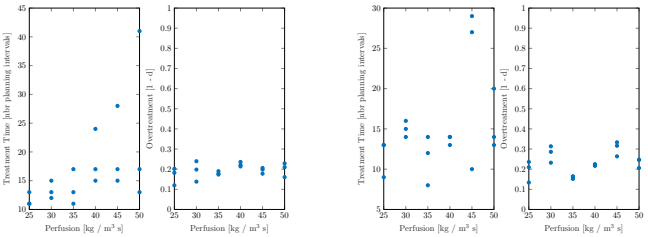

Figure 6. Results of the *perfusion simulation*: The influence of different values of the perfusion coefficient on the treatment time and the amount of overtreatment. The four values represent four different motion samples of noise level η_0.

cient. The relative tissue inhomogeneity factor $a_p = 1$ was chosen for the *comparing simulation*, and for the *noise simulations* the mean value was $a_p = 3$.

The *absorption simulation* was performed for self-scanning and tracking, the results can be seen in Figure 5. We observe that the treatment time decreases with increasing value of a_p in the self-scanning approach, while the overtreatment seems not to be affected. For the tracking on the other side, the treatment time is constant, whereas the amount of overtreatment is increasing.

The results of the *perfusion simulation* are shown in Fig. 6. We observe that the treatment time increases with increasing perfusion value for both, the tracking and the self-scanning approach. This seems reasonable, as the increased blood flow withdraws heat and thus the tissue temperature is decreased. The amount of overtreatment on the other side remains almost stable.

For the *noise simulations*, we optimized with the two different found parameter sets *ot* and *tr*. The results were evaluated by calculating the treatment time and the overtreatment and are shown in Table 3.

When comparing the results of the tracking approach to the self-scanning method, we observe that the amount of overtreatment is in the same range. However, when looking at the treatment times, the tracking approach achieves slightly shorter treatment times. Note that the near field heating is not yet included in these calculations.

Table 3. Results of the *noise simulations*. For each simulation, the treatment time (tr.Time) and the overtreatment (overtr.) are shown. The overtreatment is measured as 1 - dice coefficient between ablated tissue and tumor. The treatment time is measured in number of *planning intervals* used until target ablation. The domain Ω_1 and Ω_2 represent a smaller and a bigger 2D tumor, respectively, whereas Ω_3 is a 3D tumor. The noise level η_0 represents no noise, whereas η_1 some and η_2 moderate noise.

	Self-Scanning				**Tracking**			
Parameter set	*tr*		*ot*		*tr*		*ot*	
Simulation	tr.Time	overtr.	tr.Time	overtr.	tr.Time	overtr.	tr.Time	overtr.
Ω_1, η_0, sample 1	11	0.16	19	0.08	6	0.26	7	0.20
Ω_1, η_0, sample 2	9	0.24	19	0.27	7	0.29	18	0.18
Ω_1, η_0, sample 3	11	0.23	19	0.11	5	0.30	18	0.20
Ω_1, η_1, sample 1	11	0.34	21	0.33	6	0.18	16	0.27
Ω_1, η_1, sample 2	11	0.25	27	0.34	6	0.26	11	0.20
Ω_1, η_1, sample 3	9	0.20	19	0.19	6	0.22	11	0.20
Ω_1, η_2, sample 1	11	0.29	17	0.27	7	0.30	13	0.24
Ω_1, η_2, sample 2	13	0.16	21	0.10	7	0.27	13	0.26
Ω_1, η_2, sample 3	11	0.28	21	0.28	8	0.25	19	0.24
Ω_2, η_0, sample 1	35	0.11	79	0.13	31	0.20	50	0.13
Ω_2, η_0, sample 2	31	0.14	36	0.11	25	0.16	55	0.13
Ω_2, η_0, sample 3	45	0.13	95	0.10	21	0.16	57	0.13
Ω_2, η_1, sample 1	29	0.14	37	0.11	23	0.16	50	0.14
Ω_2, η_1, sample 2	47	0.16	75	0.15	30	0.23	53	0.13
Ω_2, η_1, sample 3	39	0.16	53	0.11	21	0.21	60	0.14
Ω_2, η_2, sample 1	37	0.14	51	0.11	29	0.20	63	0.20
Ω_2, η_2, sample 2	49	0.20	83	0.18	21	0.19	53	0.14
Ω_2, η_2, sample 3	31	0.17	55	0.18	38	0.26	46	0.13
Ω_3, η_0, sample 1	20	0.41	25	0.32	13	0.50	19	0.37
Ω_3, η_0, sample 2	27	0.47	33	0.44	10	0.38	18	0.36
Ω_3, η_0, sample 3	19	0.41	29	0.32	10	0.44	18	0.44
Ω_3, η_1, sample 1	31	0.51	31	0.42	9	0.39	22	0.43
Ω_3, η_1, sample 2	47	0.55	47	0.45	12	0.46	19	0.37
Ω_3, η_1, sample 3	23	0.46	21	0.31	11	0.47	16	0.33
Ω_3, η_2, sample 1	27	0.53	23	0.36	11	0.40	16	0.30
Ω_3, η_2, sample 2	20	0.44	27	0.34	13	0.50	17	0.34
Ω_3, η_2, sample 3	33	0.52	34	0.39	11	0.39	17	0.39

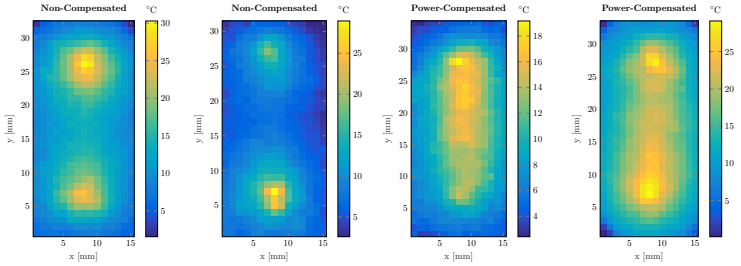

Figure 7. Maximal temperature projection over time of single focal spot experiment (ex-vivo). The left two images show the result with constant intensity values (*non-compensated*), and the right two images are the result with *power-compensated* intensity values.

As the tracking approach has no cooling times in our simulation, it is likely that the treatment time of the tracking approach will be elongated. The self-scanning approach on the other side already incorporates sonication interruptions due to the changing times, and thus the elongation due to near field heating is assumed to be less compared to tracking. Overall, the *noise simulations* shows that the proposed self-scanning approach can handle nonperiodic motion patterns in the presence of noise and tissue inhomogeneities.

4.2. *Ex-Vivo Experiments*

In Figs. 7 and 8, the maximal temperature elevation during 8 breathing cycles is shown in a slice perpendicular through the focal spot of the single focal point and the two interleaved foci experiment for both the *power-compensated* and the *non-compensated* experiment. The maximal temperature of the *power-compensated* experiments between the two extrema is more uniform as compared to the *non-compensated* cases. In particular, when calculating the normalized maximal difference between the temperatures along the focal spot trajectories, the differences are higher in the *non-compensated* cases as shown in Table 4. The difference in the temperature can approximately be halved if the intensity values are compensating for the motion (i.e. *power-compensated* intensity values are used). Moreover, as expected, the maximal temperature is higher in the *non-compensated* case, as more energy is deposited on the extrema points compared to the *power-compensated* approach. The single focal spot experiment was performed twice for both the *power-compensated* and *non-compensated* case. The difference in the maximal temperature rise map can be explained by local tissue inhomogeneities.

To evaluate our temperature model, we compared the temperature measurements during the heating period (i.e. during 8 breathing cycles) and the cooling period ($\approx 90-100\,\mathrm{s}$) to the temperature model prediction calculated by Eq. (5). The errors are calculated by taking the difference between each data measurement and corresponding simulation value for each pixel in the FOV and time point, the results are shown in Table 5. The correlation value of the uncorrected simulation is already high with values above 0.85. However, the regression slope is between $0.3 - 0.7$, indicating that the simulation values and the measurements differ mainly by a linear coefficient. This linear factor corresponds to the tissue inhomogeneity value a_p. When doing an *overall*

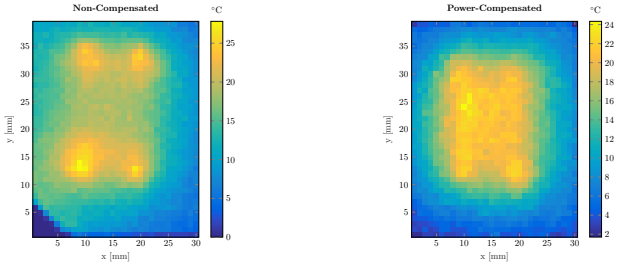

Figure 8. Maximal temperature projection over time of two interleaved foci experiments (ex-vivo). The left is with constant intensity values (*non-compensated*), and the right image is the result from *power-compensated* intensity values.

Table 4. The normalized difference of the maximal and minimal measured temperature along the focal spot trajectory. Here, the abbreviation FS stands for focal spot.

Type	**Normalized Difference** $\frac{T_{\max}-T_{\min}}{T_{\max}+T_{\min}}$
1FS, comp., ex. 1	0.20
1FS, comp., ex. 2	0.17
1FS, non-comp., ex. 1	0.35
1FS, non-comp., ex. 2	0.37
splitFS, comp.	0.06
splitFS, non-comp.	0.20
tissue inhomo. ex. non-comp.	0.36
tissue inhomo. ex. comp.	0.32
tissue inhomo. ex. comp. inhomo.	0.17

Table 5. The mean error (μ), variance (σ), correlation value (Corr.) and the regression slope (Slope) between the temperature measurements and the model simulation calculated over all pixels and measurement times. 1FS denotes the single spot experiment, whereas splitFS corresponds to the two interleaved foci experiment.

Type	**No Correction**				**Overall Correction**				**Point Correction**			
	μ	σ	Corr.	Slope	μ	σ	Corr.	Slope	μ	σ	Corr.	Slope
1FS, comp., ex. 1	2.7°C	2.5°C	0.92	0.55	0.3°C	3.2°C	0.92	1.00	0.2°C	0.8°C	0.97	0.98
1FS, comp., ex. 2	3.4°C	7.0°C	0.91	0.45	0.1°C	5.0°C	0.91	1.00	0.1°C	1.2°C	0.97	0.98
1FS, non-comp., ex. 1	1.4°C	2.8°C	0.85	0.65	0.1°C	4.2°C	0.85	1.00	0.2°C	1.7°C	0.92	0.93
1FS, non-comp., ex. 2	5.1°C	10.0°C	0.93	0.42	0.4°C	6.1°C	0.93	1.00	0.2°C	2.0°C	0.97	0.98
splitFS, comp.	4.6°C	12.9°C	0.86	0.38	0.1°C	11.0°C	0.86	1.00	0.3°C	3.3°C	0.95	0.96
splitFS, non-comp.	5.8°C	14.7°C	0.89	0.31	0.6°C	11.9°C	0.89	1.00	0.4°C	3.8°C	0.94	0.96

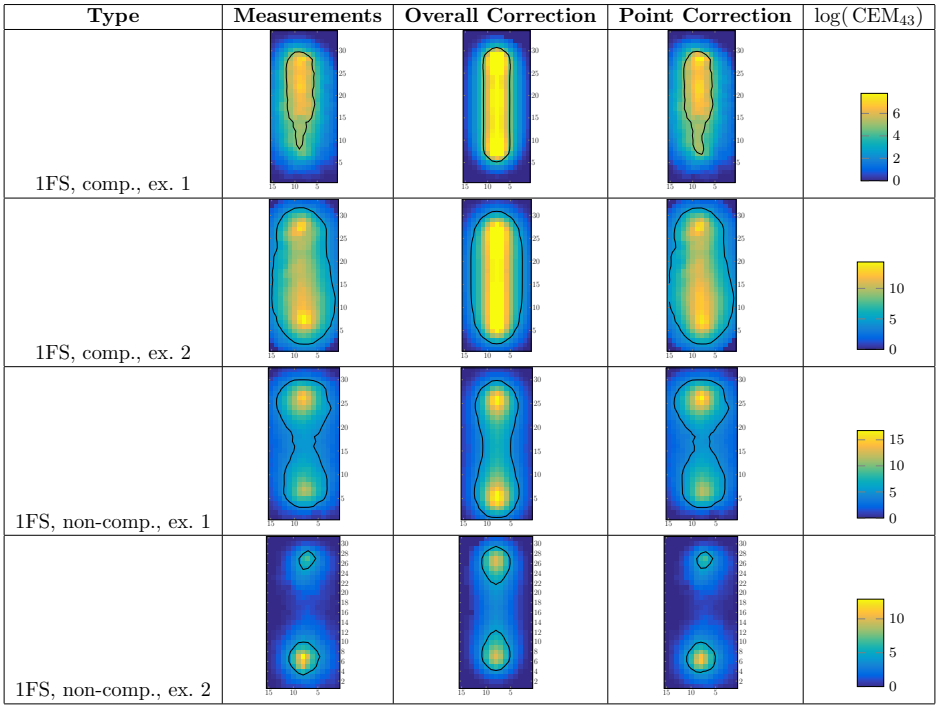

Figure 9. The thermal dose plots from the one focal spot ex-vivo experiment. The black line indicates the 120 CEM_{43} isobar, *overall correction* and *point correction* are simulation results.

correction, the correlation is not affected, but the mean error decreases, whereas the variance of the error is not improved, indicating that an *overall correction* is not enough. After the *point correction* (i.e. fitting a_p for each pixel independently), the correlation value and the regression slope are both increased to values above 0.9, which corresponds to the lower error and variance values.

In Figure 9 and 10, the thermal dose of the different models can be seen. In the first column the calculated thermal dose from the measurements is shown. For the second column, we performed an *overall correction*. In the last column, the *point corrected* simulation of the thermal dose is shown. With the *overall correction*, the predicted thermal dose is symmetric, whereas the measurement thermal dose is not. The experimental setup would suggest that the thermal dose profile is symmetric. However, the asymmetric pattern is a result of the tissue inhomogeneities. Using the *point correction*, the inhomogeneities can be modeled accurately, as can be seen visually and by the calculated dice coefficients in Fig. 11. For the dice coefficients, we segmented the tissue in two categories: the ablated and the non-ablated. Ablated means that the thermal dose is above a lethal dose, for which we chose values of the set $\{10, 20, 30, 45, 60, 120, 240\}$ and calculated for each of the given lethal doses the

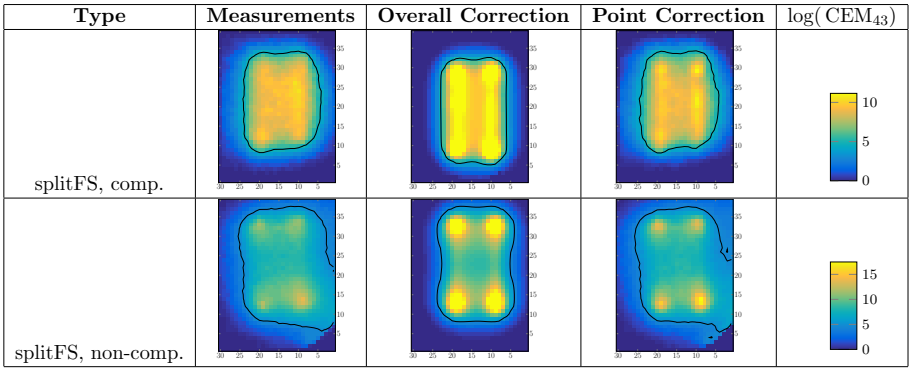

Figure 10. The thermal dose plots from the two interleaved focal spot ex-vivo experiment. The black line indicates the 120 CEM_{43} isobar, *overall correction* and *point correction* are simulation results.

dice coefficient between the simulated and the measured thermal dose segmentation. Fig. 11 shows the resulting 7 values. For the *point correction*, we achieved a mean dice coefficient of over 0.95.

Further, we verified if the framework is able to induce a uniform temperature in the presence of tissue inhomogeneities, in the *tissue inhomogeneities experiment*. We performed the *power-compensated* single focal point experiment on a non-homogeneous tissue part with temperature rises around 20°C in order to not change the tissue properties. Note that for the experiments shown in Figs. 7 and 8, the tissue location was chosen to be as homogeneous as possible. From the measured temperature, the tissue inhomogeneities were calculated using the *point correction* approach. The temperature model was updated accordingly and the intensity values were recalculated to compensate for the tissue inhomogeneities (*inhomogeneity-compensated*). In a second run, after letting the tissue cool down, the same part of the tissue was heated using the updated intensity values to obtain a more uniform temperature rise. For comparison, the *non-compensated* experiment was performed on the same tissue location. The results are shown in Fig. 12. The left and the middle images show the maximal temperature projection over time of the *non-compensated* and the *power-compensated* experiment, respectively. Both have higher temperatures at the extrema points and lower temperatures in between. It seems that the *power-compensation* was not sufficient to induce a uniform temperature, which is due to the inhomogeneous tissue properties. When updating the temperature model according to the tissue inhomogeneities (*inhomogeneity-correction*), a near uniform temperature rise is induced, as shown in the right image of Fig. 12. The intensity values used in the power tables used for the *inhomogeneity-correction* are shown in Fig. 13, together with the observed inhomogeneity values.

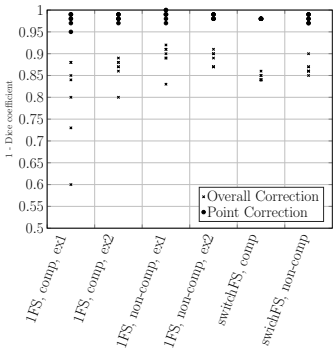

Figure 11. Dice coefficient for thermal dose segmentations. Seven different cutoff values for the thermal dose segmentation were taken and shown in the figure.

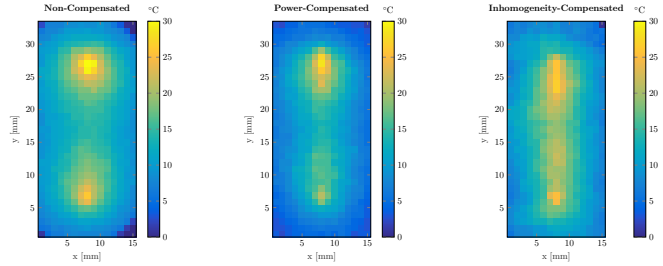

Figure 12. Maximal temperature projection over time of the *tissue inhomogeneities experiment*, all three different experiments show the same non-homogeneous tissue location. Left: *Non-compensated* experiment. Middle: *Power-compensated* experiment assuming homogeneous tissue. Right: *inhomogeneity-compensated* experiment using temperature model adapted to tissue inhomogeneities.

5. Discussion

5.1. *Simulations*

With the simulations, we showed that the proposed *feedback algorithm* can handle nonperiodic respiratory motion and tissue inhomogeneities, even in the presence of noise. As expected, an increasing level of noise results in more overtreatment and hence it is important to reduce the noise level. A possibility to reduce the noise level in the motion prediction would for example be the reduction of the *planning interval* duration. However, a limitation on the minimal duration of the *planning interval* is the computational time to update the treatment time, i.e. the time needed to find a solution to Eq. (8) and the time needed to update the temperature model. At the moment, the treatment plans can not yet be calculated in real time, the calculation time in the range of 20 s for 2D and 300 s for 3D optimization per breathing cycle, using GPU (GeForce GTX 970). Another possibility to reduce overtreatment in the presence of uncertainties could be to introduce a safety margin around the target and

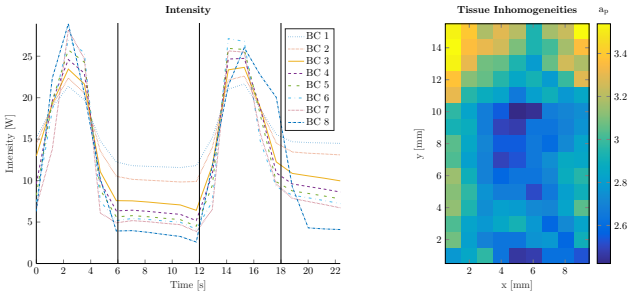

Figure 13. Left: Intensity values for the *inhomogeneity-compensated* experiment. Right: Tissue inhomogeneity values a_p observed in the *tissue inhomogeneity experiment*.

adapt it according to the expected variances in respiratory motion.

When comparing the treatment time of the *feedback algorithm* to the results in [34], we observe that the proposed algorithm achieves treatment times less than half as long. A reason for the superior results is that our algorithm is easier to solve and thus a better solution can be found in shorter computational time. Using our *feedback algorithm* it is easier to find a local minimum that is closer to the global optima, as the problem to solve is simplified by using less parameters to optimize. Moreover, the treatment time is not optimized explicitly, but is optimized in a greedy way. However, we believe that the treatment time can be further optimized, as it is unlikely that a global optima is found with the proposed method. To further reduce treatment time, a term that penalizes mechanical changes could be introduced in the optimization scheme. However, as we will discuss in Section 5.3, this will have an influence on near field heating.

When comparing the performance of the self-scanning to the tracking approach in the *noise simulation*, we observe that they perform on par. The same amount of overtreatment is induced and the treatment times of the self-scanning approach are only slightly longer in the presence of inhomogeneities and changing respiratory motion. More precisely, when comparing the performance of the tr parameters of both approaches, we observe that the mean values of the treatment times for Ω_1 and Ω_2 differ by a factor of about 1.5. The mean amount of overtreatment on the other side is about 1.3 times higher with the tracking approach. Moreover, as the self-scanning approach enables to use a HIFU device with a fixed focus and thus reduces the complexity of the beam forming problem, the self-scanning approach is a promising alternative to the tracking approach. When looking at the influence of the parameter a_p in the *absorption simulation*, one can observe that the tracking approach has faster treatment times for lower a_p, whereas the advantage of the self-scanning approach is that the amount of overtreatment does not increase with a_p. An explanation for the decreasing treatment time with increasing absorption coefficient, as shown in Figure 5, is that if a_p is small, the temperature rise is lower. Using the self-scanning approach, more time is needed for a thermal build-up along the trajectory of the focal spot. For the tracking method on the other side, the treatment time seems not to be affected, but overtreatment increases. Here, the thermal build-up is less affected due to tracking. However, if a_p increases, overtreatment is increasing as the temperature rise is higher at healthy tissue.

A question that arises when using the *feedback algorithm* is how to chose Δt, $\Delta\tau$ and m. Generally speaking, it is the better the lower the values Δt and $\Delta\tau$ are. In case of the heat source discretization $\Delta\tau$, the simulation results gets the more accurate the smaller $\Delta\tau$ is. This is due to the convergence property of $Q_{\mathrm{m}}^{\Delta\tau} \to Q_{\mathrm{m}}$, the error between the discretized heat source becomes smaller, the shorter $\Delta\tau$ gets. Some of the implications of the influence of $\Delta\tau$ are discussed in our previous work [34]. For the number of intensity values m during an *planning interval* of duration Δt holds basically the same: the more intensity values per *planning interval*, the more accurate the motion compensation and thus the planning works. However, both cases, i.e. lower $\Delta\tau$ and higher m values, induce longer computational times. For the heat source discretization, the lower $\Delta\tau$, the more summands in Eq. (5) and thus the more the temperature needs to be evaluated. When increasing m, the optimization problem in (8) has more parameters to optimize, which then results in longer calculation times. Therefore, a compromise between accuracy and computational time has to be found. The *planning interval* on the other side has to be chosen in a different way. When looking at the motion prediction, it is the best to have a short Δt, as this way the motion prediction will be more accurate. However, the *planning interval* is mainly limited to the processing latency: During the *planning interval*, the temperature measurements need to be evaluated, the tissue inhomogeneities need to be calculated and the treatment plan is updated. Therefore, Δt is limited to the computational time.

5.2. *Ex-Vivo Experiments*

The temperature model defined in Eq. (5) can handle motion and tissue inhomogeneities, as shown by ex-vivo experiments. We demonstrate that the model can accurately predict the thermal dose if a *point correction* is applied to include the tissue inhomogeneities. Moreover, we could show that a near uniform temperature rise can be induced despite the presence of tissue-inhomogeneities, whereas heating with the assumption of homogeneous tissue properties resulted in two hotspots at the extrema points of the focal point trajectory. As observed in [35], tissue changes its properties during heating. In this work, we did not account for temporal changes in the tissue inhomogeneity factor a_p. However, this could be done by updating the value a_p continuously during treatment, where not the whole temperature data of the treatment is accounted for, but only the recent measurements are considered.

The ex-vivo experiments showed the feasibility of the self-scanning approach. We were able to induce a near homogeneous temperature rise along the focal spot trajectory. However, there are some issues that need to be solved towards in-vivo experiments and real-time experiments. First of all, the computational time of the proposed algorithm needs to be accelerated. Moreover, the pre-scanning of the motion and the optical camera to detect the motion stage needs to be replaced by a motion model. As a further step, the temperature model should include non-zero perfusion. To model the vessels in liver tissue, the perfusion parameter b should assumed to be space-dependent, i.e. it should be assumed that $b = b_p$ is different for each point. Hence, in a next step, the temperature model has to be expanded to perfusion inhomogeneities. Nevertheless, the compensation of inhomogeneities as described in Section 2.2 is valid for any point-dependent factor, like absorption, diffusion, perfusion: Whatever the reason that temperature does not rise up enough at a location, the *feedback algorithm* will re-enforce the heat deposition at that location based on a posteriori data.

5.3. *Near Field Heating*

The used temperature model is limited as it is derived by the assumption that the temperature rise as well as the heat source are Gaussian distributed. This means for example that near field heating is not included in the model, which leads to problems for long treatment times. A possible solution is that the treatment can be paused until the temperature in the healthy near field region has decreased sufficiently [42, 43]. There are several possibilities to do so. One could be to have fixed heating and cooling times [42]. However, this might lead to enlarged treatment times. Another possibility is to apply an approach similar to [44], where they optimized the heating and cooling times and could shorten the treatment time significantly. They state that this optimization could be performed independently of the trajectory optimization. For our temperature model and optimization framework this would mean that we could first find a treatment plan and then optimize the cooling periods and would not have to change the proposed optimization framework. The cooling time could be further minimized by having subsequent sonication points that are far away from each other to minimize near field heating [27]. Using this, the optimization framework and the temperature model should be adapted such that sonication points far away from each other are favored in the presence of near field heating. Moreover, note that it is likely that the amount of near field heating induced in the self-scanning approach is less compared to the tracking approach. There are two reasons for this assumption: First, using the self-scanning approach, mechanical changes are used to shift the focal spot position lateral to the acoustic axis. During this time the sonication is interrupted and the tissue in the near field region can cool down. Moreover, the tissue moves underneath the focal spot, which can be viewed as having several sonication points during movement. Hence the induced near field temperature rise will be smaller. However, this depends on the motion pattern and the effect is stronger the larger the motion amplitude is. Compared to spiral and circular patterns, the proposed *feedback algorithm* has a linear pattern and thus less near field heating is induced [45].

6. Conclusion

We showed that the proposed *feedback algorithm* can be used to calculate feasible treatment plans for a self-scanning HIFU approach in moving tissue with changing respiratory motion and in the presence of tissue inhomogeneities. Compared to previous work in [34], we achieved shorter treatment times. The proposed *feedback algorithm* is a step towards online treatment planning. The treatment time is slightly longer, and the amount of overtreatment performs on par to the tracking approach. The influence of near field heating and perfusion on the treatment time of the self-scanning approach has to be further evaluated in future work. However, the advantages of the self-scanning approach is that steering of the focal spot is not needed. This results in a reduced complexity of the beam-forming through the ribs, fewer secondary lobes and no intensity decay due to steering. Hence, these benefits resulting from the fixed focus HIFU device render the idea of self-scanning attractive.

In ex-vivo experiments, we showed the feasibility of the self-scanning method. We achieved near uniform temperature rises along the focal point trajectory in moving tissue. Moreover, we could show that our temperature model accurately predicts the induced thermal dose and is able to adapt to tissue inhomogeneities.

Funding

This work was supported by the Swiss National Foundation under Grant CR33I3_143980. Access to the MR scanner was provided by the Center for Biomedical Imaging of the University of Geneva.

Disclosure statement

The authors report no conflicts of interest. The authors alone are responsible for the content and writing of the article.

References

[1] Cline HE, Schenck JF, Hynynen K, Watkins RD, Souza SP, Jolesz FA. MR-guided focused ultrasound surgery. Journal of computer assisted tomography. 1992;16(6):956–965.
[2] ter Haar G, Sinnett D, Rivens I. High intensity focused ultrasound-a surgical technique for the treatment of discrete liver tumours. Physics in medicine and biology. 1989;34(11):1743.
[3] Hynynen K. MRI-guided focused ultrasound treatments. Ultrasonics. 2010;50(2):221–229.
[4] Petrusca L, Viallon M, Terraz S, de Luca V, Celicanin Z, Auboiroux V, et al. Simultaneous Ultrasound Imaging and MRI Acquisition. In: Interventional Magnetic Resonance Imaging. Springer; 2012. p. 457–470.
[5] Petrusca L, Cattin P, De Luca V, Preiswerk F, Celicanin Z, Auboiroux V, et al. Hybrid ultrasound/magnetic resonance simultaneous acquisition and image fusion for motion monitoring in the upper abdomen. Investigative radiology. 2013;48(5):333–340.
[6] Moonen C, Quesson B, Salomir R, Vimeux FC, De Zwart J, Van Vaals J, et al. Thermal therapies in interventional MR imaging. Focused ultrasound. Neuroimaging clinics of North America. 2001;11(4):737–47.
[7] Wijlemans J, Bartels L, Deckers R, Ries M, Mali WTM, Moonen C, et al. Magnetic resonance-guided high-intensity focused ultrasound (MR-HIFU) ablation of liver tumours. Cancer Imaging. 2012;12(2):387.
[8] Ellis S, Rieke V, Kohi M, Westphalen AC. Clinical applications for magnetic resonance guided high intensity focused ultrasound (MRgHIFU): present and future. Journal of medical imaging and radiation oncology. 2013;57(4):391–399.
[9] Von Siebenthal M, Székely G, Gamper U, Boesiger P, Lomax A, Cattin P. 4D MR imaging of respiratory organ motion and its variability. Physics in medicine and biology. 2007;52(6):1547.
[10] De Senneville BD, Ries M, Bartels LW, Moonen CT. MRI-guided high-intensity focused ultrasound sonication of liver and kidney. In: Interventional Magnetic Resonance Imaging. Springer; 2012. p. 349–366.
[11] Muller A, Petrusca L, Auboiroux V, Valette P, Salomir R, Cotton F. Management of respiratory motion in extracorporeal high-intensity focused ultrasound treatment in upper abdominal organs: current status and perspectives. Cardiovascular and interventional radiology. 2013;36(6):1464–1476.
[12] Aubry JF, Pauly KB, Moonen C, Haar G, Ries M, Salomir R, et al. The road to clinical use of high-intensity focused ultrasound for liver cancer: technical and clinical consensus. Journal of therapeutic ultrasound. 2013;1(1):13.
[13] Preiswerk F, De Luca V, Arnold P, Celicanin Z, Petrusca L, Tanner C, et al. Model-guided respiratory organ motion prediction of the liver from 2D ultrasound. Medical image analysis. 2014;18(5):740–751.
[14] Auboiroux V, Petrusca L, Viallon M, Muller A, Terraz S, Breguet R, et al. Respiratory-

gated MRgHIFU in upper abdomen using an MR-compatible in-bore digital camera. BioMed research international. 2014;2014.
[15] Ries M, De Senneville BD, Roujol S, Berber Y, Quesson B, Moonen C. Real-time 3D target tracking in MRI guided focused ultrasound ablations in moving tissues. Magnetic Resonance in Medicine. 2010;64(6):1704–1712.
[16] Arnold P, Preiswerk F, Fasel B, Salomir R, Scheffler K, Cattin PC. 3D organ motion prediction for MR-guided high intensity focused ultrasound. In: Medical Image Computing and Computer-Assisted Intervention–MICCAI 2011. Springer; 2011. p. 623–630.
[17] Celicanin Z, Auboiroux V, Bieri O, Petrusca L, Santini F, Viallon M, et al. Real-time method for motion-compensated MR thermometry and MRgHIFU treatment in abdominal organs. Magnetic Resonance in Medicine. 2014;72(4):1087–1095.
[18] Holbrook AB, Ghanouni P, Santos JM, Dumoulin C, Medan Y, Pauly KB. Respiration based steering for high intensity focused ultrasound liver ablation. Magnetic Resonance in Medicine. 2014;71(2):797–806.
[19] Celicanin Z, Manasseh G, Petrusca L, Scheffler K, Auboiroux V, Crowe LA, et al. Hybrid ultrasound-MR guided HIFU treatment method with 3D motion compensation. Magnetic resonance in medicine. 2017;.
[20] Auboiroux V, Dumont E, Petrusca L, Viallon M, Salomir R. An MR-compliant phased-array HIFU transducer with augmented steering range, dedicated to abdominal thermotherapy. Physics in medicine and biology. 2011;56(12):3563.
[21] Jud C, Preiswerk F, Cattin PC. Respiratory motion compensation with topology independent surrogates. In: Workshop on imaging and computer assistance in radiation therapy; 2015. .
[22] Salomir R, Palussière J, Vimeux FC, de Zwart JA, Quesson B, Gauchet M, et al. Local hyperthermia with MR-guided focused ultrasound: Spiral trajectory of the focal point optimized for temperature uniformity in the target region. Journal of magnetic resonance imaging. 2000;12(4):571–583.
[23] Mougenot C, Salomir R, Palussière J, Grenier N, Moonen CT. Automatic spatial and temporal temperature control for MR-guided focused ultrasound using fast 3D MR thermometry and multispiral trajectory of the focal point. Magnetic resonance in medicine. 2004;52(5):1005–1015.
[24] Hui L, Guofeng S, Yazhu C. Treatment planning of scanning time and path for phased high-intensity focused ultrasound surgery. In: Biomedical Engineering and Informatics, 2009. BMEI'09. 2nd International Conference on. IEEE; 2009. p. 1–4.
[25] Zhou Y. Generation of uniform lesions in high intensity focused ultrasound ablation. Ultrasonics. 2013;53(2):495–505.
[26] Arora D, Minor MA, Skliar M, Roemer RB. Control of thermal therapies with moving power deposition field. Physics in medicine and biology. 2006;51(5):1201.
[27] Malinen M, Huttunen T, Kaipio JP, Hynynen K. Scanning path optimization for ultrasound surgery. Physics in medicine and biology. 2005;50(15):3473.
[28] Wan H, Aarsvold J, O'Donnell M, Cain C. Thermal dose optimization for ultrasound tissue ablation. IEEE transactions on ultrasonics, ferroelectrics, and frequency control. 1999;46(4):913–928.
[29] Arkin H, Holmes K, Chen M, Bottje W. Thermal pulse decay method for simultaneous measurement of local thermal conductivity and blood perfusion: a theoretical analysis. Journal of biomechanical engineering. 1986;108(3):208–214.
[30] Parker KJ. The thermal pulse decay technique for measuring ultrasonic absorption coefficients. The Journal of the Acoustical Society of America. 1983;74(5):1356–1361.
[31] Dragonu I, de Oliveira PL, Laurent C, Mougenot C, Grenier N, Moonen CT, et al. Non-invasive determination of tissue thermal parameters from high intensity focused ultrasound treatment monitored by volumetric MRI thermometry. NMR in Biomedicine. 2009;22(8):843–851.
[32] Dillon C, Vyas U, Payne A, Christensen D, Roemer R. An analytical solution for improved HIFU SAR estimation. Physics in medicine and biology. 2012;57(14):4527.

[33] Möri N, Jud C, Salomir R, Cattin P. Leveraging respiratory organ motion for non-invasive tumor treatment devices: a feasibility study. Physics in medicine and biology. 2016;61(11):4247.
[34] Möri N, Gui L, Jud C, Lorton O, Salomir R, Cattin PC. An Optimal Control Approach for High Intensity Focused Ultrasound Self-Scanning Treatment Planning. In: International Conference on Medical Image Computing and Computer-Assisted Intervention. Springer; 2017. p. 532–539.
[35] Damianou CA, Sanghvi NT, Fry FJ, Maass-Moreno R. Dependence of ultrasonic attenuation and absorption in dog soft tissues on temperature and thermal dose. The Journal of the Acoustical Society of America. 1997;102(1):628–634.
[36] Pennes HH. Analysis of tissue and arterial blood temperatures in the resting human forearm. Journal of applied physiology. 1948;1(2):93–122.
[37] Sapareto SA, Dewey WC. Thermal dose determination in cancer therapy. International Journal of Radiation Oncology* Biology* Physics. 1984;10(6):787–800.
[38] Damianou C, Hynynen K. The effect of various physical parameters on the size and shape of necrosed tissue volume during ultrasound surgery. The Journal of the Acoustical Society of America. 1994;95(3):1641–1649.
[39] Kickhefel A, Rosenberg C, Weiss CR, Rempp H, Roland J, Schick F, et al. Clinical evaluation of MR temperature monitoring of laser-induced thermotherapy in human liver using the proton-resonance-frequency method and predictive models of cell death. Journal of Magnetic Resonance Imaging. 2011;33(3):704–709.
[40] Damianou CA, Hynynen K, Fan X. Evaluation of accuracy of a theoretical model for predicting the necrosed tissue volume during focused ultrasound surgery. IEEE transactions on ultrasonics, ferroelectrics, and frequency control. 1995;42(2):182–187.
[41] Lorton O, Möri N, Guillemin P, Terraz S, Cattin P, Salomir R, et al. An experimental demonstration of HIFU self-scanning treatment in moving tissue. In: EU-FUS. Leipzig; 2017. .
[42] Damianou C, Hynynen K. Focal spacing and near-field heating during pulsed high temperature ultrasound therapy. Ultrasound in medicine & biology. 1993;19(9):777–787.
[43] Salomir R, Petrusca L, Auboiroux V, Muller A, Vargas MI, Morel DR, et al. Magnetic resonance–guided shielding of prefocal acoustic obstacles in focused ultrasound therapy: application to intercostal ablation in liver. Investigative radiology. 2013;48(6):366–380.
[44] Payne A, Vyas U, Blankespoor A, Christensen D, Roemer R. Minimisation of HIFU pulse heating and interpulse cooling times. International journal of hyperthermia. 2010;26(2):198–208.
[45] Petrusca L, Auboiroux V, Goget T, Viallon M, Muller A, Gross P, et al. A nonparametric temperature controller with nonlinear negative reaction for multi-point rapid MR-guided HIFU ablation. IEEE transactions on medical imaging. 2014;33(6):1324–1337.

Appendix

In [28], a closed-form solution to Pennes bioheat equation for a static heat source Q_s^0 placed at the origin ($q = 0$) during the power-off time, i.e. no heat source ($Q = 0$), is derived as

$$T_s(p,t;0,\Delta\tau,I) = \frac{\exp(-bt)}{4D\pi t}\iint_{-\infty}^{\infty} T_0(\alpha,\beta)\exp\left(-\frac{(p_r-\alpha)^2+(p_z-\beta)^2}{4Dt}\right)d\alpha d\beta, \quad (10)$$

for $t > \Delta\tau$. Here, $T_0(p_r, p_z)$ is the initial temperature at time $t = \Delta\tau$ and point (p_r, p_z). Now, in [28] they assumed that the temperature rise pattern during the beam-on time

is Gaussian with time-dependent amplitude and deviation:

$$T_{\mathrm{on}}(p,t;q,\Delta\tau,I)=\frac{A(t)}{2\pi\theta_r^2(t)\theta_z(t)}\exp\left(-\left(\frac{p_r^2}{2\theta_r^2(t)}+\frac{p_z^2}{2\theta_z^2(t)}\right)\right), \tag{11}$$

while at the same time assuming that the heat source is Gaussian too. This then leads to the conclusion that the time dependent deviation must be of the form

$$\theta_i(t)=\sqrt{2Dt+\sigma_i},\quad i\in\{r,z\}.$$

The derivation of these formulas are explained in more detail in [28]. To receive the formula of an explicit formula for the temperature induced by a static heat source during the power-off time, we insert Eq. (11) as initial temperature into Eq. (10) and get after integration

$$T_{\mathrm{s}}(p,t;0,\Delta\tau,I)=\frac{A(t_0)\exp(-bt)}{2\pi\theta_r^2(t)\theta_z(t)}\exp\left(-\frac{1}{2}\left(\frac{p_r^2}{\theta_r^2(t)}+\frac{p_z^2}{\theta_z^2(t)}\right)\right), \tag{12}$$

for $t\geq\Delta\tau$. Observe that when defining

$$T_{\mathrm{peak}}:=T_{\mathrm{s}}(0,\Delta\tau;0,\Delta\tau,I)=\frac{A(t_0)}{2\pi\theta_r^2(\Delta\tau)\theta_z(\Delta\tau)}, \tag{13}$$

we derive to the formula Eq. (2). The formula for the maximal temperature at the focal spot T_{peak} can be directly derived from Pennes bioheat equation. For this, we assume that the static heat source can be written as [32]

$$Q_{\mathrm{s}}^0(p,t)=2\alpha I\exp\left(-\left(\frac{p_r^2}{\sigma_r^2}+\frac{p_z^2}{\sigma_z^2}\right)\right).$$

From [28], we have the implicit solution formula for the beam-on time given as

$$T_{\mathrm{on}}(p,t;0,\Delta\tau,I)=\frac{K}{4D\pi}\int_0^t\frac{e^{-b\tau}}{t}\iint_{-\infty}^{\infty}Q_s\big((\alpha,\beta),\tau\big)\exp\left(-\tfrac{(p_r-\alpha)^2+(p_z-\beta)^2}{4D\tau}\right)d\alpha d\beta d\tau.$$

Inserting Q_{s} into the formula above, setting $p=0$ and solving the integrals, we get

$$T_{\mathrm{on}}(0,t,0,\Delta\tau,I)=2\alpha IK\sigma_r^2\sigma_z\int_0^{\Delta\tau}\frac{\exp(-b\tau)}{\sqrt{(\sigma_z^2+4D\tau)}(\sigma_r^2+4D\tau)}d\tau,$$

which is Eq. (3).

8 Discussion and Conclusion

Achievements. It was our goal to develop a method for a self-scanning approach to calculate optimal treatment plans that ablate the whole liver tumor, while minimizing treatment time and the treatment of healthy tissue. Moreover, the method should be able to handle nonperiodic respiratory motion.

In a first version (Chapter 5), we showed the feasibility of the self-scanning approach on a simplified model, assuming a linear dose. We showed that the achieved treatment time obtained with the self-scanning approach was shorter compared to the tracking approach, but more treatment of healthy tissue was found. However, the used dose model was not yet accurate enough to persist in a realistic scenario.

We changed to a more realistic model incorporating the Pennes bioheat equation and the non-linear thermal dose (Chapter 6). The results are expected to be a better estimation of reality. We found that the self-scanning and the tracking approach gave the same treatment times, and also the amount of overtreatment was in the same range, although the self-scanning approach resulted in slightly more overtreatment. However, we still assumed repetitive respiratory motion, which is rather unlikely to occur in the treatment of a patient.

In a third version (Chapter 7), we expanded our approach to include nonperiodic respiratory motion. The method is based on an adaptive temperature model, that is able to model tissue inhomogeneities which only become visible during MR-thermometry measurements. The advantage of such an approach is that the method can adapt itself to inhomogeneities and thus correct for modeling errors. This concept of updating the temperature model was tested in ex-vivo experiments. We could show that first of all, the temperature model and the method to adapt the sonication power to the respiratory motion is feasible. The observed temperature rise induced by the HIFU device was shown to be as predicted by simulations. Moreover, we could confirm that we are able to induce a uniform temperature rise along the focal spot trajectory in moving tissue. In a further step, we showed that not only the motion, but also tissue inhomogeneities can be corrected by our method. By sonicating a inhomogeneous part of the tissue, we observed that correcting the sonication power to the motion pattern is not sufficient. In fact, also tissue inhomogeneities need to be corrected. By adapting our temperature model to the observed inhomogeneities and recalculating the power values, we achieved a uniform temperature rise along the focal spot in moving tissue and in the presence of tissue inhomogeneities. With the ex-vivo experiments, we could confirm the theoretical findings of this thesis and do a first step towards in-vivo and clinical experiments.

Limitations. Although a method could be proposed that is able to handle nonperiodic respiratory motion and tissue inhomogeneities, there are still many open issues. As an example, the question on how to deal with near field heating and the influence of perfusion needs to be answered. Moreover, the computational cost is an issue that needs to be solved.

The impact of near field heating on the treatment time was already discussed in Chapter 7. To summarize, near field heating is currently not included into our temperature model. To further shorten the treatment time, it is suggested to include near field heating into the planning algorithm. There are different possibilities to do so. For example, a "near field term" could be added to the temperature model. When introducing such a term, the proposed feedback algorithm from Chapter 7 can be used with the updated temperature model. The resulting treatment plans would then avoid heating of healthy tissue in the near field region. This would be a further step towards more realistic treatment plans. In particular, a more realistic treatment time can be estimated when including the near field heating. We expect that the algorithm will then choose sonication points that are more apart to avoid near field heating. This will probably not much change the treatment time of the self-scanning approach, as it incorporates already changing times, which minimizes near field heating. For the tracking approach on the other side, no cooling times are considered so far. Therefore, we expect that the treatment times for the tracking approach will increase if near field heating is modeled. However, the exact impact of including the near field heating into the simulation needs to be further evaluated.

We investigated the influence of perfusion in a simulation in Chapter 7, where we altered the perfusion coefficient on the whole tissue domain and evaluated its influence on the treatment time and the amount of overtreatment. This surely gives a first impression on how the algorithm works in presence of blood perfusion. We showed that the treatment time increases with increasing perfusion rate, while the amount of overtreatment does not seem to be affected. However, the perfusion is not a homogeneous value over the whole tissue domain, but it rather changes its value depending on where blood vessels are located and how large they are. We assume that the perfusion can be expressed as a spatial parameter - similar to the absorption coefficient resulting in the investigated tissue inhomogeneity parameter. Hence, we suggest to write the perfusion as a position dependent parameter that changes its value depending on the location of the blood vessels. To determine the values of the perfusion coefficient, it is possible that a similar approach can be used as with the tissue inhomogeneities. However, here the relation will not be linear, but it is an exponential relationship. Hence, a solution has to be found to fit the tissue inhomogeneities and perfusion parameter simultaneously.

Another issue of the proposed method is its calculation time. At the moment, it is not yet possible to calculate the treatment times in real time. As the method needs to be further expanded by including near field heating into the temperature model and a more complex fitting method to include non-homogeneous perfusion values, the computational cost will most likely further increase. There are several possible solutions to this problem. First of all, although the code of the algorithm consist of some parts that are already implemented in CUDA to run on a graphics card (GPU),

most of it still runs on Matlab. We believe that if more work and time is spent by porting the code to a faster language and by changing the existing CUDA code to a more efficient one, the computational time can be certainly improved. However, the question will be if this is already enough. Another possibility is to find a compromise between accuracy of the temperature simulation, the number of iterations used in the optimization and computational time. For example, the simulation of the temperature, which needs to be done several times during optimization, runs much faster if it is evaluated on a coarse spatial and temporal grid. However, when reducing the spacing, the simulation gets less accurate. The same holds for the optimization problem: If less iterations are performed, the computational time will be shorter, but the resulting treatment plan will not be an optimal solution. Hence, a good compromise has to be found. There might be some heuristics that help in finding optimal treatment plans in shorter time: if for example the starting point of the optimization problem is chosen close enough to a local minimum, less iterations are needed until convergence.

Outlook. In future work, the adaption to tissue inhomogeneities could be further improved by incorporating the time-dependency of the tissue parameters. To do so, fitting the tissue inhomogeneity values should not be performed over the whole treatment period, but only on the most recent measurements. The length of the temporal window needs to be set in an appropriate way, such that there is enough data for a proper fit, but at the same time it should be short enough to capture temporal changes.

From a more mathematical point of view, it would be very interesting and relevant to explore the robustness of the method. We already investigated the influence of noise on the motion prediction and tissue inhomogeneity values in Chapter 7, and could show that the algorithm is robust. However, the relationship between the different noise and discretization parameters would be interesting to know. For example, we used a fixed time interval Δt, for which the current treatment plan was assumed to be optimal. After the time interval, the treatment plan was recalculated by considering the changed organ motion and tissue inhomogeneities. It would be very interesting to know how the treatment time, overtreatment, the parameter Δt and the motion noise are related. This could give an idea on how fast the treatment plan should be updated in the presence of noise.

It is still a long way towards clinical implementation of the self-scanning approach. One of the most crucial parts besides the near field and perfusion modeling is that the treatment plans can at the moment not be calculated in real-time. Moreover, the treatment planning workflow has to be established to run fully automatically. For example the processing of MR-thermometry measurements to update the temperature model is not yet fully automated. In addition, in-vivo experiments and clinical studies are required and it is important to implement safety constraints to ensure that the treatment is immediately interrupted if the treatment plan fails.

Conclusion. The advantages of the self-scanning approach is that steering of the focal spot is not required. Three dimensional steering of the focal spot produces secondary lobes and the intensity of the acoustic beam is decreased when focusing away from

the natural spot. These two disadvantages are avoided in the self-scanning approach due to the fixed focus device. Moreover, the beam-forming problem through the ribs is more complicated when steering the focal spot, as for each position of the focal spot the problem needs to be resolved. For the self-scanning approach on the other side, the beam is static and thus the beam-forming problem has to be solved only once. Overall, the self-scanning approach to treat tumors within moving tumors is a promising alternative to the tracking approach.

When comparing the achievements to the goals of this PhD project, we observe that we found a method that is able to ablate the whole tumor, while minimizing treatment time and the amount of overtreatment. Moreover, the method is able to handle nonperiodic respiratory motion and we could proof the performance of our approach in ex-vivo experiments. Nevertheless, we could not yet find a method that is able to run in real time, although the computational time has already significantly improved from the second to the third publication. Instead, we could adapt our method to tissue inhomogeneities and proof the feasibility of our method in ex-vivo experiments.

There are still some open problems that arise with the self-scanning method, which include the near field heating and inhomogeneous perfusion values. Moreover, the treatment planning workflow has to be automated towards clinical implementation.

Nevertheless, we believe that the results presented in this thesis showed the feasibility of the self-scanning approach and provides a treatment planning method which showed its capability in ex-vivo experiments and that is able to model and correct for tissue inhomogeneities.

Bibliography

[1] Ravi P Agarwal and Donal O'Regan. *An introduction to ordinary differential equations*. Springer Science & Business Media, 2008.

[2] Sean F Altekruse, Katherine A McGlynn, and Marsha E Reichman. Hepatocellular carcinoma incidence, mortality, and survival trends in the united states from 1975 to 2005. *Journal of clinical oncology*, 27(9):1485–1491, 2009.

[3] Dhiraj Arora, Mark A Minor, Mikhail Skliar, and Robert B Roemer. Control of thermal therapies with moving power deposition field. *Physics in medicine and biology*, 51(5):1201, 2006.

[4] Vincent Auboiroux, Erik Dumont, Lorena Petrusca, Magalie Viallon, and Rares Salomir. An MR-compliant phased-array HIFU transducer with augmented steering range, dedicated to abdominal thermotherapy. *Physics in medicine and biology*, 56(12):3563, 2011.

[5] Jean-Francois Aubry, Kim B Pauly, Chrit Moonen, Gail Ter Haar, Mario Ries, Rares Salomir, Sham Sokka, Kevin M Sekins, Yerucham Shapira, Fangwei Ye, Heather Huff-Simonin, Matt Eames, Arik Hananel, Neal Kassell, Alessandro Napoli, Joo Ha Hwang, Feng Wu, Lian Zhang, Andreas Melzer, Young-sun Kim, and Wladyslaw M Gedroyc. The road to clinical use of high-intensity focused ultrasound for liver cancer: technical and clinical consensus. *Journal of therapeutic ultrasound*, 1(1):13, 2013.

[6] MR Bailey, VA Khokhlova, OA Sapozhnikov, SG Kargl, and LA Crum. Physical mechanisms of the therapeutic effect of ultrasound (a review). *Acoustical Physics*, 49(4):369–388, 2003.

[7] Julius Balogh, Emad H Asham David Victor III, Sherilyn Gordon Burroughs, Maha Boktour, Ashish Saharia, Xian Li, R Mark Ghobrial, and Howard P Monsour Jr. Hepatocellular carcinoma: a review. *Journal of hepatocellular carcinoma*, 3:41, 2016.

[8] Nicolás Benech, Carlos Negreira, and Stefan Catheline. Monitoring local temperature changes in soft tissues by time-reversal elastography. In *Ultrasonics Symposium (IUS), 2009 IEEE International*, pages 2414–2417. IEEE, 2009.

[9] Stephen Boyd and Lieven Vandenberghe. *Convex optimization*. Cambridge university press, 2004.

[10] Jordi Bruix and Morris Sherman. Management of hepatocellular carcinoma: an update. *Hepatology*, 53(3):1020–1022, 2011.

[11] Richard H Byrd, Mary E Hribar, and Jorge Nocedal. An interior point algorithm for large-scale nonlinear programming. *SIAM Journal on Optimization*, 9(4):877–900, 1999.

[12] Gianpaolo Carrafiello, Domenico Laganà, Monica Mangini, Federico Fontana, Gianlorenzo Dionigi, Luigi Boni, Francesca Rovera, Salvatore Cuffari, and Carlo Fugazzola. Microwave tumors ablation: principles, clinical applications and review of preliminary experiences. *International Journal of Surgery*, 6:S65–S69, 2008.

[13] Vincent Chan and Anahi Perlas. Basics of ultrasound imaging. In *Atlas of ultrasound-guided procedures in interventional pain management*, pages 13–19. Springer, 2011.

[14] Jean-Yves Chapelon, Dominique Cathignol, Charles Cain, Emad Ebbini, Jan-Ulco Kluiwstra, Oleg A Sapozhnikov, Gérard Fleury, Rémi Berriet, Laurent Chupin, and Jean-Luc Guey. New piezoelectric transducers for therapeutic ultrasound. *Ultrasound in medicine & biology*, 26(1):153–159, 2000.

[15] Harvey E Cline, John F Schenck, Kullervo Hynynen, Ronald D Watkins, Steven P Souza, and Ferenc A Jolesz. MR-guided focused ultrasound surgery. *Journal of computer assisted tomography*, 16(6):956–965, 1992.

[16] Joshua Coon, Nick Todd, and Robert Roemer. HIFU treatment time reduction through heating approach optimisation. *International Journal of Hyperthermia*, 28(8):799–820, 2012.

[17] Alexander Copelan, Jason Hartman, Monzer Chehab, and Aradhana M Venkatesan. High-intensity focused ultrasound: current status for image-guided therapy. In *Seminars in interventional radiology*, volume 32, pages 398–415. Thieme Medical Publishers, 2015.

[18] Ben Cox. Acoustics for ultrasound imaging. *Lecture Notes, University College London*, 2013.

[19] C Damianou and K Hynynen. Focal spacing and near-field heating during pulsed high temperature ultrasound therapy. *Ultrasound in medicine & biology*, 19(9):777–787, 1993.

[20] C Damianou and K Hynynen. The effect of various physical parameters on the size and shape of necrosed tissue volume during ultrasound surgery. *The Journal of the Acoustical Society of America*, 95(3):1641–1649, 1994.

[21] Baudouin Denis De Senneville, Charles Mougenot, and Chrit TW Moonen. Real-time adaptive methods for treatment of mobile organs by MRI-controlled high-intensity focused ultrasound. *Magnetic Resonance in Medicine*, 57(2):319–330, 2007.

[22] Baudouin Denis de Senneville, Mario Ries, Lambertus W Bartels, and Chrit TW Moonen. MRI-guided high-intensity focused ultrasound sonication of liver and kidney. In *Interventional Magnetic Resonance Imaging*, pages 349–366. Springer, 2011.

[23] Bart Decadt and Ajith K Siriwardena. Radiofrequency ablation of liver tumours: systematic review. *The lancet oncology*, 5(9):550–560, 2004.

[24] Emad S Ebbini and Gail Ter Haar. Ultrasound-guided therapeutic focused ultrasound: current status and future directions. *International Journal of Hyperthermia*, 31(2):77–89, 2015.

[25] Julia K Enholm, Max O Kohler, Bruno Quesson, Charles Mougenot, Chrit TW Moonen, and Shunmugavelu D Sokka. Improved volumetric MR-HIFU ablation by robust binary feedback control. *IEEE Transactions on Biomedical Engineering*, 57(1):103–113, 2010.

[26] Xiaobing Fan and Kullervo Hynynen. Ultrasound surgery using multiple sonications—treatment time considerations. *Ultrasound in medicine & biology*, 22(4):471–482, 1996.

[27] Wladyslaw MW Gedroyc and Ann Anstee. MR-guided focused ultrasound. *Expert review of medical devices*, 4(4):539–547, 2007.

[28] Oleg Grodzevich and Oleksandr Romanko. Normalization and other topics in multi-objective optimization. 2006.

[29] Michael Hinze, René Pinnau, Michael Ulbrich, and Stefan Ulbrich. *Optimization with PDE constraints*, volume 23. Springer Science & Business Media, 2008.

[30] Martijn Hoogenboom, Dylan Eikelenboom, Martijn H den Brok, Arend Heerschap, Jurgen J Fütterer, and Gosse J Adema. Mechanical high-intensity focused ultrasound destruction of soft tissue: working mechanisms and physiologic effects. *Ultrasound in medicine & biology*, 41(6):1500–1517, 2015.

[31] http://www.examrefresh.com/transducer arrays/. Transducer arrays, 2018.

[32] Renate Huch, Klaus D Jürgens, and D Fessel. *Mensch, Körper, Krankheit*. Jungjohann, 1994.

[33] Christoph Jud, Frank Preiswerk, and Philippe C Cattin. Respiratory motion compensation with topology independent surrogates. pages 9–16, 2016.

[34] James E Kennedy. High-intensity focused ultrasound in the treatment of solid tumours. *Nature reviews cancer*, 5(4):321–327, 2005.

[35] Max O Köhler, Charles Mougenot, Bruno Quesson, Julia Enholm, Brigitte Le Bail, Christophe Laurent, Chrit TW Moonen, and Gösta J Ehnholm. Volumetric HIFU ablation under 3D guidance of rapid MRI thermometry. *Medical physics*, 36(8):3521–3535, 2009.

[36] Thomas A Leslie and James E Kennedy. High-intensity focused ultrasound principles, current uses, and potential for the future. *Ultrasound quarterly*, 22(4):263–272, 2006.

[37] Tahar Loulou and Elaine P Scott. Thermal dose optimization in hyperthermia treatments by using the conjugate gradient method. *Numerical Heat Transfer: Part A: Applications*, 42(7):661–683, 2002.

[38] Matti Malinen, Tomi Huttunen, and Jari P Kaipio. Optimization and control methods for ultrasound surgery. 2005.

[39] Hassan Mansour. Beyond l1-norm minimization for sparse signal recovery. In *Statistical Signal Processing Workshop (SSP), 2012 IEEE*, pages 337–340. IEEE, 2012.

[40] R Timothy Marler and Jasbir S Arora. The weighted sum method for multi-objective optimization: new insights. *Structural and multidisciplinary optimization*, 41(6):853–862, 2010.

[41] Jamie R McClelland, David J Hawkes, Tobias Schaeffter, and Andrew P King. Respiratory motion models: a review. *Medical image analysis*, 17(1):19–42, 2013.

[42] Charles Mougenot, Rares Salomir, Jean Palussiere, Nicolas Grenier, and Chrit TW Moonen. Automatic spatial and temporal temperature control for MR-guided focused ultrasound using fast 3D MR thermometry and multispiral trajectory of the focal point. *Magnetic resonance in medicine*, 52(5):1005–1015, 2004.

[43] A Muller, Lorena Petrusca, Vincent Auboiroux, PJ Valette, R Salomir, and F Cotton. Management of respiratory motion in extracorporeal high-intensity focused ultrasound treatment in upper abdominal organs: current status and perspectives. *Cardiovascular and interventional radiology*, 36(6):1464–1476, 2013.

[44] Allison Payne, Urvi Vyas, Adam Blankespoor, Douglas Christensen, and Robert Roemer. Minimisation of HIFU pulse heating and interpulse cooling times. *International journal of hyperthermia*, 26(2):198–208, 2010.

[45] Harry H Pennes. Analysis of tissue and arterial blood temperatures in the resting human forearm. *Journal of applied physiology*, 1(2):93–122, 1948.

[46] Lorena Petrusca, Vincent Auboiroux, Thomas Goget, Magalie Viallon, Arnaud Muller, Patrick Gross, Christoph D Becker, and Rares Salomir. A nonparametric temperature controller with nonlinear negative reaction for multi-point rapid MR-guided HIFU ablation. *IEEE transactions on medical imaging*, 33(6):1324–1337, 2014.

[47] Christian Rosenberg, Antje Kickhefel, Birger Mensel, Tilman Pickartz, Ralf Puls, Joerg Roland, and Norbert Hosten. PRFS-based MR thermometry versus an alternative T1 magnitude method–comparative performance predicting thermally induced necrosis in hepatic tumor ablation. *PloS one*, 8(10):e78559, 2013.

[48] Sébastien Roujol, Chrit Moonen, and Baudouin Denis de Senneville. Motion correction techniques for MR-guided HIFU ablation of abdominal organs. In *Frontiers of Medical Imaging*, pages 355–376. World Scientific, 2015.

[49] Rares Salomir, Jean Palussière, Frédéric C Vimeux, Jacco A de Zwart, Bruno Quesson, Maurice Gauchet, Pierre Lelong, Jean Pergrale, Nicolas Grenier, and Chrit TW Moonen. Local hyperthermia with MR-guided focused ultrasound: Spiral trajectory of the focal point optimized for temperature uniformity in the target region. *Journal of magnetic resonance imaging*, 12(4):571–583, 2000.

[50] Rares Salomir, Lorena Petrusca, Vincent Auboiroux, Arnaud Muller, Maria-Isabel Vargas, Denis R Morel, Thomas Goget, Romain Breguet, Sylvain Terraz, Jerry Hopple, Montet Xavier, Christoph D. Becker, and Magalie Viallon. Magnetic resonance–guided shielding of prefocal acoustic obstacles in focused ultrasound therapy: application to intercostal ablation in liver. *Investigative radiology*, 48(6):366–380, 2013.

[51] Stephen A Sapareto and William C Dewey. Thermal dose determination in cancer therapy. *International Journal of Radiation Oncology* Biology* Physics*, 10(6):787–800, 1984.

[52] Michael Schwenke, Jan Strehlow, Sabrina Haase, Juergen Jenne, Christine Tanner, Thomas Langø, Arjo J Loeve, Ioannis Karakitsios, Xu Xiao, Yoav Levy, Giora Sat, Mario Bezzi, Stefan Braunewll, Matthias Guenther, Andreas Melzer, and Tobias Preusser. An integrated model-based software for FUS in moving abdominal organs. *International Journal of Hyperthermia*, 31(3):240–250, 2015.

[53] J Segen. Segen's medical dictionary. *Huntingdon Valley, Farlex*, 2012.

[54] Martin von Siebenthal. *Analysis and modelling of respiratory liver motion using 4DMRI*, volume 48, [3-86628-194-3]. ETH Zurich, 2008.

[55] Virginia P Studdert, Clive C Gay, and Douglas C Blood. *Saunders Comprehensive Veterinary Dictionary E-Book*. Elsevier Health Sciences, 2011.

[56] Gail R Ter Haar. High intensity focused ultrasound for the treatment of tumors. *Echocardiography*, 18(4):317–322, 2001.

[57] Fredi Tröltzsch. Optimale Steuerung partieller Differentialgleichungen. *Vieweg, Wiesbaden*, 2005.

[58] Ewout Van Den Berg and Michael P Friedlander. Probing the pareto frontier for basis pursuit solutions. *SIAM Journal on Scientific Computing*, 31(2):890–912, 2008.

[59] Thomas J Vogl, Nagy NN Naguib, Nour-Eldin A Nour-Eldin, Pramod Rao, Alborz Hedayati Emami, Stefan Zangos, Mohamed Nabil, and Ahmed Abdelkader. Review on transarterial chemoembolization in hepatocellular carcinoma: palliative, combined, neoadjuvant, bridging, and symptomatic indications. *European journal of radiology*, 72(3):505–516, 2009.

[60] Martin von Siebenthal, Gabor Szekely, Urs Gamper, Peter Boesiger, Antony Lomax, and Ph Cattin. 4D MR imaging of respiratory organ motion and its variability. *Physics in medicine and biology*, 52(6):1547, 2007.

[61] Richard A Waltz, José Luis Morales, Jorge Nocedal, and Dominique Orban. An interior algorithm for nonlinear optimization that combines line search and trust region steps. *Mathematical programming*, 107(3):391–408, 2006.

[62] Hong Wan, John Aarsvold, Matthew O'Donnell, and Charles Cain. Thermal dose optimization for ultrasound tissue ablation. *IEEE transactions on ultrasonics, ferroelectrics, and frequency control*, 46(4):913–928, 1999.

[63] Feng Wu. High intensity focused ultrasound (HIFU) ablation. In *Tumor Ablation*, pages 61–75. Springer, 2013.

[64] Ya-xiang Yuan. A review of trust region algorithms for optimization. In *ICIAM*, volume 99, pages 271–282, 2000.

[65] Marvin C Ziskin. Fundamental physics of ultrasound and its propagation in tissue. *Radiographics*, 13(3):705–709, 1993.

Nadia Möri

Curriculum Vitae

Contact Details

E-Mail **nadia.moeri@bluemail.ch**.

Education

since 2015 **PhD in Biomedical Engineering**, *University of Basel*, Topic: Generation of Treatment Plans for Magnetic Resonance guided High Intensity Ultrasound in Liver.
Supervisor: Prof. Dr. Philippe Cattin, Department of Biomedical Engineering

2013–2015 **Master of Science in Mathematics**, *University of Bern*, Master Thesis: Monotone singularly perturbed semilinear boundary value problems.
Supervisor: Prof. Dr. Thomas Wihler

2009–2013 **Bachelor of Science in Mathematics**, *University of Bern*, Minors: Biology and Computer Science, Bachelor Thesis: Fraktale Dimension von Gruppen und Ringen in $\mathbb{R}$.
Supervisor: Prof. Dr. Zoltan Balogh

2006–2009 **Matura**, *Seeland Gymnasium Biel*, Main focus: Physics and applied mathematics.

Publications

Nadia Möri, Christoph Jud, Rares Salomir, and Philippe C Cattin. Leveraging respiratory organ motion for non-invasive tumor treatment devices: a feasibility study. *Physics in medicine and biology*, 61(11):4247, 2016.

Nadia Möri, Laura Gui, Christoph Jud, Orane Lorton, Rares Salomir, and Philippe C Cattin. An optimal control approach for high intensity focused ultrasound self-scanning treatment planning. In *International Conference on Medical Image Computing and Computer-Assisted Intervention*, pages 532–539. Springer, 2017.

Christoph Jud, Nadia Möri, Benedikt Bitterli, and Philippe C Cattin. Bilateral regularization in reproducing kernel hilbert spaces for discontinuity preserving image registration. In *International Workshop on Machine Learning in Medical Imaging*, pages 10–17. Springer, 2016.

Christoph Jud, Nadia Mori, and Philippe C Cattin. Sparse kernel machines for discontinuous registration and nonstationary regularization. In *Proceedings of the IEEE Conference on Computer Vision and Pattern Recognition Workshops*, pages 9–16, 2016.

Christoph Jud, Robin Sandkühler, Nadia Möri, and Philippe C Cattin. Directional averages for motion segmentation in discontinuity preserving image registration. In *International Conference on Medical Image Computing and Computer-Assisted Intervention*, pages 249–256. Springer, 2017.